Numerical Parametric Study of Fast Biomass Pyrolysis in a Gas Solid Vortex Reactor

Stijn Vangaever

Supervisors: Prof. dr. ir. Geraldine Heynderickx, Dr. Maria del Mar Torregrosa Galindo
Counsellor: Kaustav Niyogi

Master's dissertation submitted in order to obtain the academic degree of
Master of Science in Chemical Engineering

Department of Chemical Engineering and Technical Chemistry
Chair: Prof. dr. ir. Guy Marin
Faculty of Engineering and Architecture
Academic year 2015-2016

UNIVERSITEIT GENT

UNIVERSITEIT GENT

FACULTY OF **ENGINEERING AND ARCHITECTURE**

Department of Chemical Engineering and Technical Chemistry
Laboratory for Chemical Technology
Director: Prof. Dr. Ir. Guy B. Marin

Laboratory for Chemical Technology

Declaration concerning the accessibility of the master thesis

Undersigned,

Stijn Vangaever

Graduated from Ghent University, academic year 2015-2016 and is author of the master thesis with title:

Numerical Parametric Study of Fast Biomass Pyrolysis in a Gas Solid Vortex Reactor

The author gives permission to make this master dissertation available for consultation and to copy parts of this master dissertation for personal use.
In the case of any other use, the copyright terms have to be respected, in particular with regard to the obligation to state expressly the source when quoting results from this master dissertation.

01-06-2016

Stijn Vangaever

Acknowledgements

With this master dissertation coming to an end also five years of education in chemical engineering at Ghent University comes to a close. Five years of hard work, exciting courses and countless experiences. This project would not have been possible without the help and support of numerous people, who I would like to thank accordingly.

At first I want to thank prof. dr. ir. Guy Marin for providing the opportunity to work on this thesis in optimal circumstances. Secondly I would like to thank my supervisor prof. dr. ir. Geraldine Heynderickx. I could always pass by and have interesting discussions providing me of new input or a new angle.

My gratitude also goes to Kaustav Niyogi, my coach who was always available and always ready to help. His experience on CFD modelling and the gas-solid vortex reactor proved to be a great asset throughout the year. I also want to thank Marita Torregrosa for reviewing chapters of my thesis, proposing the necessary adjustments and adding interesting comments.

My fellow students, who I worked with daily also deserve my acknowledgements. They were always available to talk to about our subjects when necessary or to talk about something completely different when we had the need to. Special thanks goes out to the “penthouse”. Moreno, Lennert and Andres, we had some great times working on our thesis.

At last my acknowledgements go out to my family and my girlfriend, Sofie, who has always supported me.

Stijn Vangaever

"When I meet God, I am going to ask him two questions: Why relativity? And why turbulence? I really believe he will have an answer for the first."

W. Heisenberg

Numerical Parametric Study of Fast Biomass Pyrolysis in a Gas Solid Vortex Reactor

Stijn Vangaever

Master's dissertation submitted in order to obtain the academic degree of
Master of Science in Chemical Engineering

Academic year 2015-2016

Promotors: Prof. dr. ir. Geraldine Heynderickx, dr. Maria del Mar Torregrosa Galindo
Coach: Kaustav Niyogi

GHENT UNIVERSITY

Faculty of Engineering and Architecture

Department of Chemical Engineering and Technical Chemistry
Laboratory for Chemical Technology
Chairman: prof. dr. ir. Guy B. Marin

Abstract

The goal of this master dissertation is to gain more insight in the bed dynamics of a gas-solid vortex reactor. This dissertation can be divided in three major parts. A literature study has been performed comparing gravitational fluidized bed reactors, which have been the most extensively explored technology for fast biomass pyrolysis processes, to gas-solid vortex reactors, which show favorable properties for fast biomass pyrolysis reactions. The second part of the dissertation consists of a parametric study of a gas-solid vortex reactor geometry using computational fluid dynamics. The influence of changing the slot thickness and the injection slot angle on operating conditions including radial velocities, tangential velocities and heat transfer coefficients in the gas-solid vortex reactor is investigated. The third part of the dissertation focusses on the computational fluid dynamic modelling of fast biomass pyrolysis in a gas-solid vortex reactor. The interaction between the various phases is studied with the emphasis on the volume fraction, temperature profile and outlet composition of the different phases.

Keywords: Gas solid vortex reactor, fast biomass pyrolysis, geometric study, heat transfer

Numerical Parametric Study of Fast Biomass Pyrolysis in a Gas Solid Vortex Reactor

Stijn Vangaever

Promotors: prof. dr. ir. G. Heynderickx, dr. Maria del Mar Torregrosa
Coach: Kaustav Niyogi

***Abstract*: Conversion of biomass via fast pyrolysis and other thermal, biological and mechanical conversion processes is positioned to become an important part of the energy landscape of the future. Pyrolysis of lignocellulosic biomass in a gas-solid vortex reactor (GSVR) is modeled to assess the potential of this centrifugal fluidization reactor technology and to explore its process intensification abilities. The effect of changing geometric parameters of a gas-solid vortex reactor on the hydrodynamics inside the reactor chamber were investigated. Cold flow computational fluid dynamic (CFD) simulations were performed on various reactor geometries to investigate both the influence of injection slot angle and the injection slot thickness on the local heat transfer coefficient and the radial and azimuthal velocities at various positions in the reactor. In a second step fast biomass pyrolysis simulations were performed to gain insight in the bed dynamics of the gas and solid phases. A stable bed at temperatures suitable for fast biomass pyrolysis was obtained with a product distribution around 73 wt% tar, 17 wt% char and 10 wt% pyrolysis gas.**

***Keywords*: gas-solid vortex reactor, fast biomass pyrolysis, geometric study, heat transfer**

I. Introduction

Biomass can be converted into more valuable forms of energy via numerous processes. Pyrolysis is a thermal conversion process with fast pyrolysis being carried out at temperatures between 450 and 500 °C and short reaction times up to 2.0 s in order to maximize the liquid tar yield [1].

The gas-solid vortex has the ability to meet the necessary criteria for fast biomass pyrolysis. The high gas-solid slip velocities, that result in high convective heat transfer coefficients, and short gas phase residence time in the reactor ensure a high heat transfer rate and precise temperature control which are, together with the necessity for rapid cooling of the pyrolysis vapors, the three main characteristics to optimize fast pyrolysis processes as outlined by Bridgwater and Peacocke [2]. The GSVR is sometimes also referred to as Rotating Fluidized Bed in Static Geometry (RFB-SG). The RFB-SG geometry has characteristics of both fluidized bed and packed bed reactors. These unique attributes allow it to significantly improve processes that suffer from convective heat or mass-transfer limitations.

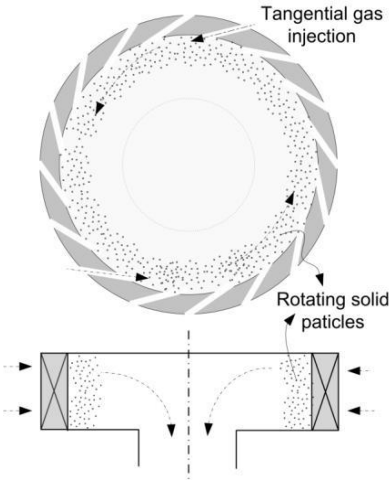

Fig. 1: Visual representation of a gas-solid vortex reactor.

Standard rotating fluidized beds (RFB), with a rotating reactor chamber, are similar to the GSVR and should be acknowledged both as a competitor technology and as a source of information. These reactors share many of the same operating principles with a GSVR, but with added mechanical complexity that comes with large rotating parts, such as complex sealing, mechanical vibrations and wear and tear [3]. Both reactor types replace the gravitational field by a larger centrifugal field. The centrifugal field in a RFB is generated by mechanically rotating the reactor vessel. In a RFB-SG the centrifugal field is introduced by the tangential injection of the fluid phase through the inlet slots. An advantage of RFB over RFB-SG is that for rotating fluidized bed reactors the gas flow rate and the rotational velocity of the bed can be set independently.

Computational fluid dynamics simulations were performed to gain more insight in the gas velocity profiles inside the GSVR and to investigate the geometric dependency of the azimuthal and radial velocity components which determine the process hydrodynamics such as residence time, gas-solid slip velocities and heat transfer coefficients. The simulations presented in this work model the behavior of a GSVR that is similar in geometry to an existing experimental unit [4]. The distributor jacket diameter is 0.68 m, the reactor diameter equals 0.54 m and the exhaust diameter is 0.2 m. The reactor height is 0.1 m and 36 injection slots are present with an injection slot opening of 2.0 mm and an injection slot angle of 10°.

II. Effect of slot thickness

Initially gas-only numerical simulations were performed to investigate the influence the geometric parameters on the bed hydrodynamics. The injection slot thickness is varied while keeping the injection slot angle 20°. The CFD software package ANSYS Fluent 15.0 was used to perform the calculations. The reactor was modeled with a 2-D projection using a 360° cross section. Eulerian-Eulerian simulations were performed using the realizable k-ε model with initially only air entering the reactor jacket at 1102 Nm^3/h. The azimuthal velocity increases significantly with decreasing slot thickness as can be intuitively expected since the total injection area is reduced while the gas feeding rate is kept constant. Not only the azimuthal velocity of the gaseous phase is of importance. The ratio between the azimuthal, v_θ, and radial velocity, v_r, is called the swirl ratio and is indicative for the ratio of angular momentum to radial momentum in a vortex [5].

$$Swirl\ ratio = \left|\frac{v_\theta}{v_r}\right| \tag{1}$$

The absolute value of the swirl ratio along the radius increases with decreasing slot thickness. However this trend is less pronounced comparing the 2.0 mm inlet to the 1.5 mm inlet, as shown in Fig. 2.

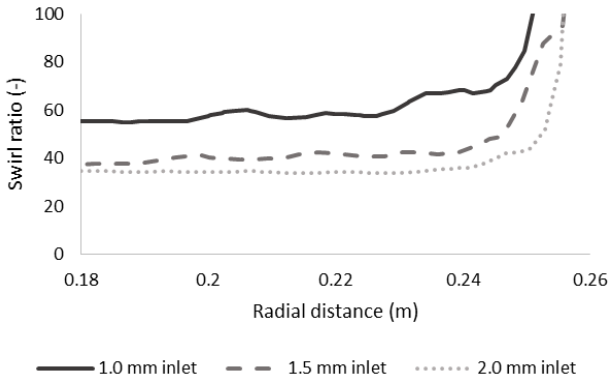

Fig. 2 Local swirl ratio in function of radial distance at steady-state after 2.0 s for a constant 20° angle and a varying injection slot thickness.

In a next step two-phase simulations will be performed with both polymer particles and air in the reactor. The Eulerian granular solids formulation was employed to model the particle behavior, using the per phase realizable k-ε model for turbulence. The Gidaspow model was used to model the fluid-solid drag interactions since the Gidaspow model is recommended for dense fluidized beds [6]. Turbulence interaction was accounted for using the Simonin et al. model [7]. In order to generate a stable polymer bed, only gas is fed for 2.0 s until steady-state is reached. In a second step the polymer particles with a density of 950 kg/m^3 and a diameter of 1.0 mm, which corresponds to the experimental setup are fed in the reactor for 2.5 s [4]. After the polymer feeding step, only air is send through the GSVR until 8.0 s of simulation time has passed and steady-state is again reached.

The fluidized bed dynamics inside the GSVR are determined by the ratio between the drag and centrifugal forces working on the polymer particles. A higher centrifugal force suppresses the bed height and the drag force tends to expand the bed. The drag force is given by the Ergun equation:

$$F_{D,r} = 150\frac{\mu_g(1-\varepsilon)^2}{\varepsilon^3 d_p^2}v_{g,r} + 1.75\frac{(1-\varepsilon)\rho_g}{\varepsilon^3 d_p}v_{g,r}^2 \tag{2}$$

The centrifugal force per unit volume is proportional to the racial coordinate assuming the angular velocity ω remains constant throughout the bed:

$$F_{C,r} = \rho_s(1-\varepsilon)r\omega^2 \tag{3}$$

However for the GSVR, the angular velocity ω is dependent on the radius and can be calculated by rescaling the tangential velocity, v_{θ,r_m}, at a specific radius:

$$\omega = \frac{v_{\theta,r_m}}{r_m} \tag{4}$$

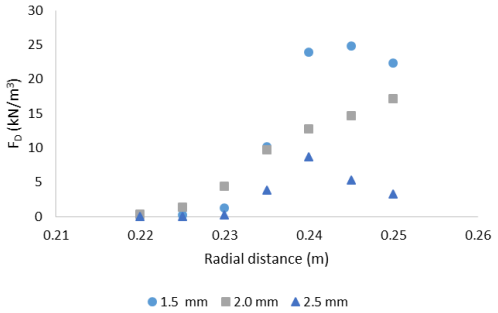

Fig. 3 Drag forces working on the polymer bed in function of radial distance for a constant injection slot angle of 20°.

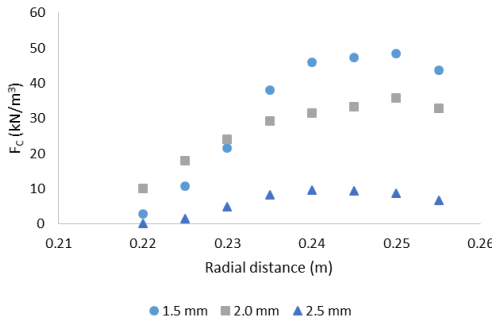

Fig. 4 Centrifugal forces working on the polymer bed in function of radial distance for a constant injection slot angle of 20°.

Drag and centrifugal forces operating on the polymer bed appear to increase with decreasing slot thickness as shown in Figs. 3 and 4. In the case of granular flows ANSYS Fluent uses a Nusselt number correlation by Gunn [8] which is applicable in a porosity range of 0.35 – 1.0 and for Reynolds numbers up to 10^5:

$$Nu_p = \frac{h_p.d_p}{\lambda_g} = \left(7 - 10\varepsilon_g + 5{\varepsilon_g}^2\right)\left(1 + 0.7.Re_p^{0.2}.Pr^{0.5}\right) + \left(1.33 - 2.4\varepsilon_g + 1.2{\varepsilon_g}^2\right).Re_p^{0.7}.Pr^{0.5} \tag{5}$$

In this equation, h_p is the particle-scale convective heat transfer coefficient, d_p the particle diameter, λ_g the thermal conductivity of the gas, ε_g is the gas volume fraction, Pr the Prandtl number of the gas phase and Re_p the particle Reynolds number based on the gas-solid slip velocity:

$$Re_p = \frac{\rho_p.d_p.|v_g - v_s|}{\mu_g} \tag{6}$$

Where μ_g is the dynamic gas phase viscosity and ρ_p is the polymer density. The cold-flow Fluent simulations were performed without solving the energy equation. It has to be pointed out that the heat transfer coefficient is calculated during the post processing of the simulations, based on the gas-solid slip velocity, the gas volume fraction and the Prandtl number. The Prandtl number is a dimensionless number defined as the ratio of momentum diffusivity to thermal diffusivity and is usually assumed to be 0.707 for air at room temperature.

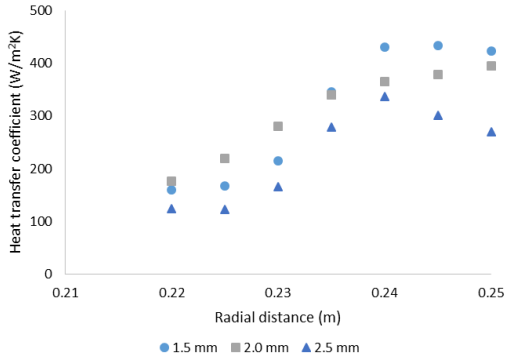

Fig. 5 Local heat transfer coefficient in function of radial distance for varying injection slot thickness and a constant 20° injection angle.

III. Effect of Injection Slot Angle

In a next step, the injection slot angle is varied from the 10° angle to larger angles including 15° and 20° injection slot angles for a constant injection slot thickness of 2.0 mm. The total centrifugal and drag force operating on the polymer bed is given in Table 1. There is no significant difference between the forces operating on the polymer bed for injection slot angles higher than 15°.

Table 1: Centrifugal and drag forces operating on the polymer bed for various injection slot angles

injection angle	Drag force (N)	Centrifugal force (N)
10°	63.43	97.87
15°	31.38	64.52
20°	29.65	63.62

The centrifugal force is bigger than the drag force operating in the bed, generating a stable bed where the polymer particles do not elude with the gas phase. The total gravitational force on the bed is in the order of 19.62 N, calculated by multiplying the mass with the gravitational acceleration, g. The centrifugal forces working on the polymer bed are a multiple of the gravitational forces, with accelerations ranging from 8 to 10 g for the various injection slot angles. This leads to the determination that neglecting the gravitational acceleration is acceptable.

Calculated heat transfer coefficients are higher in the polymer bed of the geometry with the 10° injection angle as shown in Fig. 6.

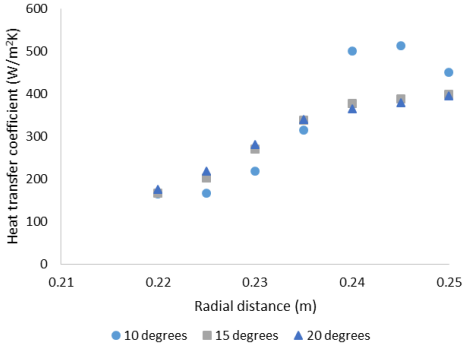

Fig. 6 Local heat transfer coefficient in function of radial distance for varying injection slot angles

IV. Biomass Fast Pyrolysis

After analyzing the geometric parameters, fast biomass pyrolysis was modeled in a gas-solid vortex reactor with an injection slot thickness of 2.0 mm and an injection slot angle of 10°. The simulations were done by first modeling a stable sand bed inside the GSVR. In a second step lignocellulosic biomass was fed to the GSVR. The biomass-sand interactions and possible phase segregation phenomena were investigated before enabling the fast biomass pyrolysis kinetics. The final goal was to generate a stable reactor bed at temperatures suitable for fast biomass pyrolysis 450 – 500 °C, in order to calculate biomass conversions and to compare the results with the classical fluidized riser reactors used for fast biomass pyrolysis.

The gas phase was defined as the primary phase using the ideal gas law for the density and the mass-weighted mixing law for viscosity and thermal conductivity. The secondary phases biomass, char and sand were all defined as granular phases with a particle diameter of 500 µm.

Fluid-solid drag interactions were accounted for using the Gidaspow model and solid-solid drag forces were modeled using the Syamlal-O'Brein symmetric drag model [9]. The Gunn correlation was used to calculate the heat exchange coefficient for fluid-solid interactions. So far the phase interactions correspond to the polymer-air GSVR simulations of the previous section. Since more than one particulate phase was modeled in the fast biomass pyrolysis simulations, solid-solid heat transfer has to be accounted for. This heat transfer was assumed to consist mainly out of radiation as suggested by Ashcraft et al. [10], which can be implemented manually by a user-defined function for every particulate phase.

$$Q_i = \left[\frac{W}{m^3}\right] = \left(\frac{6}{d_p}\right) \cdot \frac{\epsilon \cdot \sigma}{\varepsilon_s} \sum_{solids} \varepsilon_k \left(T_k^4 - T_i^4\right) \qquad (7)$$

Here, Q_i is the volumetric heat source term, d_p is the particle diameter (m), ϵ is the emissivity of the material, the Stefan-Boltzmann constant σ equals $5.676 \times 10^{-8}\, W/m^2 \cdot K^4$, ε_s is the total solids volume fraction, and T is the absolute temperature in Kelvin.

A. Sand and biomass feeding

Initially only nitrogen was sent through the GSVR reactor jacket at a volumetric flow rate of 1102 Nm^3/h at 923 K. After 2.0 s when steady-state was reached, the sand phase was sent through the reactor jacket for 1.0 s in order to reach a sand bed of 2.0 kg.

After obtaining a stable sand bed the biomass feeding is enabled. A user-defined function ensured that biomass consisting of 36 wt% cellulose, 47 wt% hemicellulose and 17 wt% lignin, was fed homogeneously at 300 K in the reactor chamber at a radial distance between 0.25 and 0.255 m.

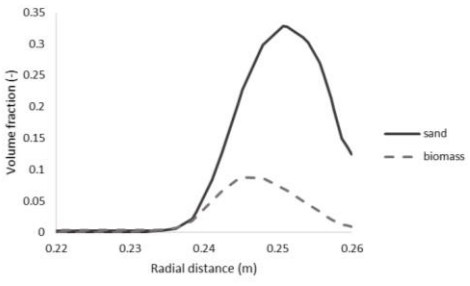

Fig. 7 Volume fractions of sand and biomass in function of radial distance after 2.5 s of biomass feeding

Segregation of both phases was expected to occur but in this case both bed masses differ in order of magnitude, 96.70 g of biomass compared to 2.0 kg of sand and no segregation is observed. It is believed that increasing the amount biomass would result in segregation.

B. Reaction mechanism

The fast biomass pyrolysis reaction network was based on the previous work performed by Xue et al. [11]. The used reaction mechanism can be described as a multiple-component multiple-step reaction mechanism. This devolatilization scheme assumes that biomass is composed of three components: cellulose (CL), hemicellulose (HC) and lignin (LG). The biomass mass fractions of cellulose, hemicellulose and lignin will influence the obtained product yield of fast pyrolysis. Secondary tar cracking is also taken into account in this mechanism.

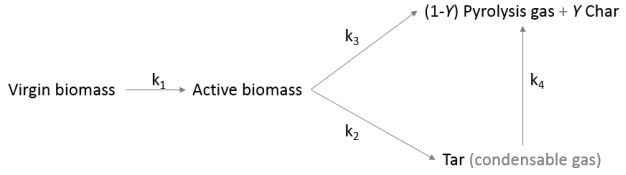

Fig. 8 Reaction network for the multiple component multiple-step devolatilization scheme.

Immediately after implementing the fast biomass pyrolysis reaction mechanism when a stable biomass bed was formed after 2.5 s of feeding, a temperature drop in the reactor was observed. An energy balance was necessary to determine the heat required to heat up the wet biomass phase to temperatures suitable for fast biomass pyrolysis. Since the nitrogen feed is the only heat source the inlet velocity of nitrogen was increased to 2.73 m/s, this was done stepwise. Another possibility was to increase the nitrogen inlet temperature but this idea was dismissed since an increased flow rate is easier to control in an experimental setup.

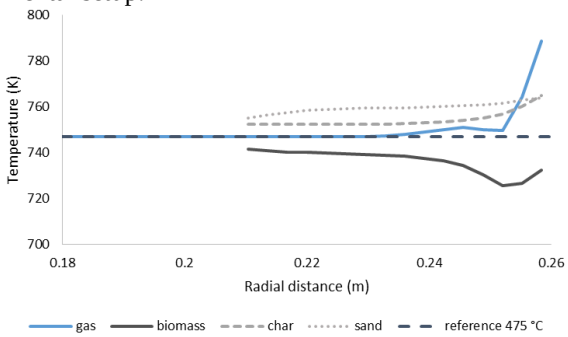

Fig. 9 Temperature profiles inside the reactor chamber once the reactor bed is heated up to temperatures around 750 K.

Ashcraft et al. [10] used a biomass the same biomass composition which corresponds to the composition of bagasse previously used for fast biomass pyrolysis simulations in a fluidized-bed riser-reactor by Xue et al. [11]. Changing the biomass feed to the same composition gives after reaching steady state product distributions given in Table 2.

Table 2: Reaction products in weight percentage of the fed biomass for the performed simulations in comparison with scientific literature.

	Simulation	Ashcraft et al. [10]	Xue et al. [11]
pyro gas	9.91 ± 0.01 wt%	9.5 wt%	21.5 wt%
tar	73.17 ± 0.05 wt%	73.8 wt%	63.4 wt%
char	16.90 ± 0.06 wt%	16.1 wt%	14.4 wt%

C. Reduce char diameter

When continuing the simulations for an extended time period, the char phase remains trapped in the reactor chamber. This accumulation of char over time does not correspond with the claim that char would leave the vortex reactor through the central outlet entrained in the gas phase. The char particle diameter is reduced to 100 µm. Remark that in real life a distribution of char particle diameters will be encountered. Fig. 10 shows the char phase leaving the reactor through the outlet entrained in the gas phase.

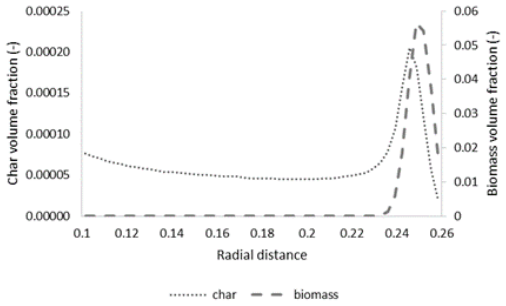

Fig. 10 Char and biomass volume fractions in function of radial distance for a 100 µm char particle diameter 3.5 after enabling the reaction mechanism.

V. Conclusion

Two-phase simulations were performed with a polymer bed inside the GSVR while feeding the same volumetric gas flow rate as in the gas-only simulations. Because of the momentum transfer from the gas phase to the polymer, the velocity profiles of the two-phase simulations are significantly different from the gas-only simulations.

When comparing heat transfer coefficients inside the polymer bed it was observed that reducing the injection slot thickness and selecting a more tangential injection angle results in higher heat transfer coefficients, especially in the regions where the polymer bed is most dense. The drag and centrifugal forces also increase when reducing the injection slot thickness and increasing the tangential injection angle. However the ratio of the centrifugal force over the drag force appears to be almost independent of the GSVR geometry.

A reactive CFD simulation of fast biomass pyrolysis in a gas-solid vortex reactor was modeled. The high tar yield of 73.2 wt% confirms the claim that the gas-solid vortex reactor offers process intensification possibilities as compared to classical riser reactors where only 63.4 wt% of the fed bagasse is converted to the desired tar product.

Char was reported to stay in the reactor chamber, which is undesired. In reality the char leaves the reactor through the outlet entrained in the gas phase. To account for this experimentally expected behavior, the model was adjusted by reducing the char particle diameter from 500 µm to 100 µm.

REFERENCES

1. Mohan, D., C.U. Pittman, and P.H. Steele, *Pyrolysis of wood/biomass for bio-oil: A critical review.* Energy & Fuels, 2006. **20**(3): p. 848-889.
2. Bridgwater, A.V. and G.V.C. Peacocke, *Fast pyrolysis processes for biomass.* Renewable & Sustainable Energy Reviews, 2000. **4**(1): p. 1-73.
3. De Wilde, J., *Gas–solid fluidized beds in vortex chambers.* Chemical Engineering and Processing: Process Intensification, 2014. **85**: p. 256-290.
4. Ekatpure, R.P., et al., *Experimental investigation of a gas–solid rotating bed reactor with static geometry.* Chemical Engineering and Processing: Process Intensification, 2011. **50**(1): p. 77-84.
5. Bloor, M.I.G. and D.B. Ingham, *The flow in industrial cyclones.* Journal of Fluid Mechanics, 1987. **178**: p. 507-519.
6. Syamlal, M., W. Rogers, and T.J. O'Brien, *MFIX documentation: Theory guide.* National Energy Technology Laboratory, Department of Energy, Technical Note DOE/METC-95/1013 and NTIS/DE95000031, 1993.
7. Simonin, C. and P. Viollet, *Predictions of an oxygen droplet pulverization in a compressible subsonic coflowing hydrogen flow.* Numerical Methods for Multiphase Flows, FED91, 1990: p. 65-82.
8. Gunn, D., *Transfer of heat or mass to particles in fixed and fluidised beds.* International Journal of Heat and Mass Transfer, 1978. **21**(4): p. 467-476.
9. Syamlal, M., *The particle-particle drag term in a multiparticle model of fluidization*, in *Other Information: Portions of this document are illegible in microfiche products. Original copy available until stock is exhausted*. 1987. p. Medium: X; Size: Pages: 25.
10. Ashcraft, R.W., G.J. Heynderickx, and G.B. Marin, *Modeling fast biomass pyrolysis in a gas-solid vortex reactor.* Chemical Engineering Journal, 2012. **207**: p. 195-208.
11. Xue, Q., T.J. Heindel, and R. Fox, *A CFD model for biomass fast pyrolysis in fluidized-bed reactors.* Chemical Engineering Science, 2011. **66**(11): p. 2440-2452.

Table of Contents

Nomenclature

List of Symbols

d_p	particle diameter [m]
D_E	exhaust diameter [m]
D_J	distributer jacket diameter [m]
D_R	reactor chamber diameter [m]
E_a	activation energy [kJ]
F_c	radial centrifugal force [N]
F_D	radial drag force [N]
I_N	number of inlet slots [m]
I_O	inlet slot thickness [mm]
K	fluid-solid momentum exchange coefficient []
L_R	reactor length [m]
m_{bed}	mass of bed [kg]
M_W	molecular weight [g/mol]
Nu_p	particle Nusselt number [-]
p	pressure [kPa]
Pr	Prandtl number [-]
Q_i	volumetric heat source term [W/m^3]
r	radial position [m]
R	gas constant [J/mol K]
R_E	exhaust radius [m]
R_J	Distributer jacket radius [m]

R_R	reactor chamber radius [m]
Re_p	particle Reynolds number [-]
T	temperature [K]
v_g	gas velocity [m/s]
v_r	radial velocity [m/s]
v_s	solid velocity [m/s]
v_θ	tangential velocity [m/s]
v_{slip}	gas-solid slip velocity [m/s]

List of Greek Symbols

ϵ	emissivity [-]
ε	void fraction [-]
ε_g	gas volume fraction [-]
ε_s	solids volume fraction [-]
λ_g	thermal conductivity of the gas phase [W/mK]
μ_g	gas dynamic viscosity [Pa s]
ρ_g	gas density [kg/m^3]
ρ_s	solids density [kg/m^3]
σ	Stefan-Boltzmann constant [W/m^{2}K^4]
ϑ	injection angle [°]

Abbreviations

BIOTC	biomass thermochemical conversion
CFD	computational fluid dynamics
CL	cellulose
GSVR	gas solid vortex reactor
HC	hemicellulose
LG	lignin
RFB	rotating fluidized bed
RFB-SG	rotating fluidized bed in a static geometry

Chapter 1: Literature study

Table of Contents

List of Figures

List of Tables

1.1. Introduction

For years there has been an incentive to investigate alternative sources of energy because of the limited fossil fuel resources and the social pressure to reduce greenhouse gas emissions. More recently, advances in the chemical industry allow us to convert biomass to more easy transportable high energy density product. Because of this evolution, conversion of biomass via fast pyrolysis and other thermal, biological and mechanical conversion processes is positioned to be an important part of the energy landscape of the future.

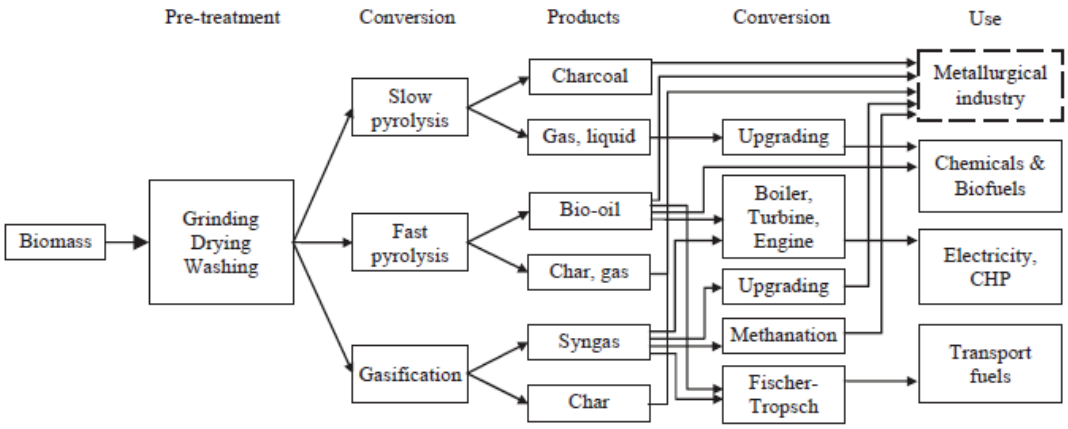

Figure 1- 1: Schematic illustration of the three main biomass thermochemical conversion pathways [1].

However a lot of obstacles still have to be overcome to utilize the biomass pyrolysis products effectively and economically [2]. In this literature study the focus will be on the fast biomass pyrolysis process. First a historical overview of the thermochemical conversion processes will be given. Classical, gravitational fluidized bed reactors, which have been the most extensively investigated technology for fast biomass pyrolysis, will be compared to the gas-solid vortex reactor (GSVR), which is a promising alternative because of its short gas phase residence time and high heat transfer rates. The focus will be publications on computational fluid dynamic modeling of the fast biomass pyrolysis mechanism in various reactor geometries.

1.2. Fast biomass pyrolysis

1.2.1. Historical background

The term bio-fuel is referred to as liquid or gaseous fuels for the transport sector that are predominantly produced from biomass. Bio-fuels are generally considered as offering many priorities, including sustainability, reduction of greenhouse gas emissions, regional development, social structure, agriculture and security of supply [3]. Worldwide energy consumption has increased 17 fold in the last century and emissions of CO_2, SO_2 and NO_x from fossil-fuel combustion are primary causes of atmospheric pollution [4]. Known petroleum reserves are estimated to be depleted in less than 50 years at the present rate of consumption [5]. Up until now 97% of all transportation energy in the United States is currently derived from non-renewable petroleum [6]. Foreign oil accounts for more than half of all oil used in the United States and the European union. The fact that oil is non-renewable and the fact that both Europe and the United States depend heavily on foreign suppliers are excellent incentives for developing renewable sources. The growth in the rate of energy consumption in developing economies in Asia, particularly India and China, raises this incentive for most countries. Environmental concerns are also an important driving factor for the search for alternative energy sources. Plant growth needed to generate biomass absorbs atmospheric carbon dioxide in order to produce glucose by photosynthesis [7]. By combustion of this biomass the stored carbon will again be released in the atmosphere but in a carbon dioxide neutral cycle. These features help to provide a growing trend towards employing modern technologies and efficient bio-energy conversion using a range of biofuels, which are becoming cost-wise competitive with fossil fuels [8, 9].

Biomass can be converted into more condensed forms of energy via processes including thermal, biological and mechanical processes [10, 11]. Thermal conversion processes include direct combustion to provide heat for steam production and hence electricity generation [12]. Gasification provides a fuel gas that can be combusted, generating heat, or can be used in an engine or turbine for energy generation. The third alternative thermal process is pyrolysis [13]. Pyrolysis itself is a very complex phenomenon, it involves heat transfer to the particle, chemical reactions within the particle and the escape of volatiles through the particle pores [14]. When organic, carbonaceous, matter is heated in the absence of air, it decomposes to non-condensable pyrolysis gas, a gaseous tar phase which is later condensed to liquid and solid char. The goal is to manipulate this pyrolysis product yield by changing operating conditions as temperature, heating rate and vapor-residence time.

The origin of pyrolysis dates back to before the industrial revolution, when tar for caulking and embalming agents was made by pyrolysis of biomass. Pyrolysis processes have been improved and are now widely used for charcoal production. In the 1980s, researchers found that the pyrolysis liquid yield could be increased using fast pyrolysis where a biomass feedstock is used and the produced vapors are condensed at a rapid rate. This produced bio-oil could be an alternative source of energy compared to fossil fuels.

Pyrolysis can roughly be categorized into slow and fast pyrolysis. The terms slow and fast pyrolysis are somewhat arbitrary, there is no precise definition of the temperatures, times and heating rates. In conventional slow pyrolysis the biomass is slowly heated to around 500 °C, with vapor residence times from 5 to 30 min. In fast pyrolysis, the heating rate is much higher, with vapor residence times reduced to several seconds, and temperatures up to 700 °C [6]. Temperatures of around 500 °C will result in a higher liquid tar fraction yield up to 60-70 wt%. Fast pyrolysis carried out at high temperatures of around 700 °C, will maximize the pyrolysis gas yield. Historically slow pyrolysis was used to produce charcoal for the metallurgical industry [15]. Slow pyrolysis is less energy efficient since only one third of the initial chemical energy of the biomass is conserved in the liquid tar phase compared to 60 % of the chemical energy for fast pyrolysis [16]. Only in the last thirty years, fast pyrolysis at moderate temperatures of around 500 °C and short reaction times up to 2.0 s has become a technology of considerable interest because it maximizes the liquid tar yield, which is a more condensed transportable form of energy compared to unconverted biomass [17]. The produced bio-oils are dark brown, free-flowing organic liquids that are comprised of highly oxygenated compounds [12].

Throughout the scientific literature various methods of biomass pyrolysis have been defined based on the temperature, heating rate and residence time. As a conclusion, an overview is given in Table 1-1 of the various modes of pyrolysis as defined by Bridgwater et al. [17].

Table 1-1: Typical product weight yields obtained by different modes of pyrolysis.

Mode	Conditions	Tar	Char	Gas
Fast	∼500 °C short hot vapor residence time ∼1 s	75 %	12 %	13 %
Intermediate	∼500 °C hot vapor residence time 10-30 s	50 %	25 %	25 %
Carbonization (slow)	∼400 °C long vapor residence time days	30 %	35 %	35 %
Gasification	∼750 – 900 °C short vapor residence time	5 %	10 %	85 %
Torrefaction (slow)	∼300 °C solid residence time 10-60 min	0 %	80 %	20 %

1.2.2. Biomass composition

Biomass can be defined as non-fossil organic material having an intrinsic chemical energy content derived from living or recently living organisms, such as wood and herbaceous material. [18] The chemical composition of biomass differs significantly from that of coal, oil and other non-renewable resources. The large presence of oxygen in the chemical composition, means that the pyrolytic chemistry differs sharply from other fossil feeds [6]. Biomass is essentially a composite material constructed from oxygen-containing organic polymers. Biomass consists overall of three main components: cellulose, hemi-cellulose and lignin [19]. Minor low-molar-mass extraneous materials, mostly organic extractives and inorganic minerals, are also present in biomass, usually between 4-10 %. [20]

Cellulose

As early as in 1838, it was established that the fibrous component of all higher plant cells had a unique chemical structure, which was named cellulose [21]. In about 1930 the macromolecular nature of cellulose was described as a polymer of glucose units. The chemical composition and conformation of cellulose chains combined with their hydrogen bonding system are responsible for the tendency to form crystalline aggregates [21, 22].

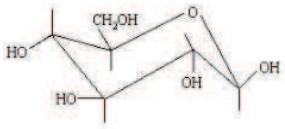

Figure 1-2: Glucopyranose unit of cellulose [23].

Hemi-cellulose

A second major wood chemical constituent is hemicellulose. Hemicellulose is a mixture of various polymerized monosaccharaides such as glucose and galactose. The difference between cellulose and hemicellulose is that cellulose contains only glucose as a monomer unit in its structure, hemicellulose however contains various saccharides [6]. Hemicelluloses exhibit lower molecular weights than cellulose. Hemicellulose decomposes at temperatures of 200 - 260 °C, giving rise to more volatiles, less tar and less chars than cellulose, which decomposes at temperatures above 430 °C [24].

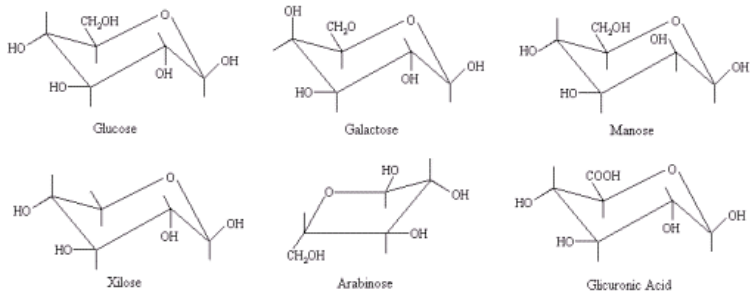

Figure 1-3: Various saccharides found in hemi-cellulose polymers [23].

Lignin

Lignin, a constituent in almost all dry-land plant cell walls, is second only to cellulose in natural occurrence. This natural polymer has drawn a lot of attention due to its complexity, non-uniformity and conjunctive bonding to other substances. Due to its chemical properties, lignin has been difficult to isolate without modification and difficult to convert into useful consumer products. Lignin as a polymer is built up by the combination of three basic monomer building blocks that might differ in the substitutions: p-cumaryl alcohol, coniferyl alcohol and sinapyl alcohol substitutions [25]. Lignin is the main binder for the agglomeration of fibrous cellulosic components while it also provides a shield against the microbial or fungal destruction of the cellulosic fibers [6].

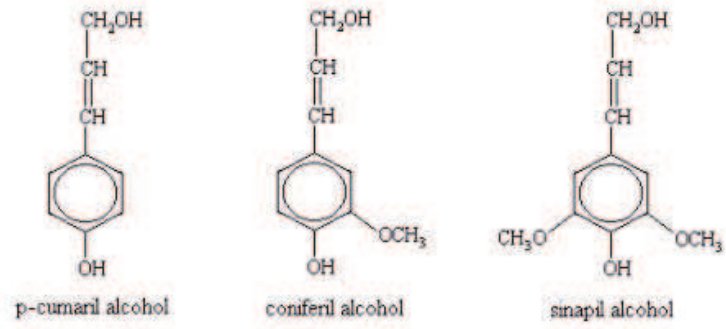

Figure 1- 4: Three phenyl propane monomers found in lignin [23].

1.3. Computational Fluid Dynamics of fast biomass pyrolysis

Gravitational riser reactors will be discussed before going into more detail on the specific vortex reactor setup. Since no experimental results have been obtained for fast biomass pyrolysis in a vortex reactor, it is important to focus on the work performed on classical fluidized bed reactors because they are a competitive technology that can give insight in the fluidized bed dynamics for fast biomass pyrolysis processes in general. The focus will first be on the experimental setup of a gravitational fluidized bed reactor, this will give a better idea the operating conditions and challenging scale-up aspects of the reactor. Next the developed CFD models for this reactor type will be discussed.

1.3.1. Gravitational fluidized bed reactors

Experimental setup

The fluidized bed technology is a well-studied technology known from the petrochemical industry. [26] Fluidized bed reactors have a lot of potential for the production of condensable tar by fast biomass pyrolysis since they allow a good heat and mass transfer between the gas phase and the individual particles [27], and high heating rates can be achieved [28]. An additional interesting feature of this reactor type is that char does not accumulate in the bed, but is elutriated with the gas flow, after which it may be filtered out, making the reactor suitable for continuous operation [28].

Considerable progress has been achieved for fast pyrolysis for biofuel production [9]. Several pilot plants have been built and tested experimentally. However some technical challenges still need to be solved to enable large-scale industrialization of this process [29]. A good example of a lab scale setup is the 100 g biomass per hour bubbling fluidized bed reactor, that was designed and built at the Center for Sustainable and Environmental Technologies of Iowa State University [30].

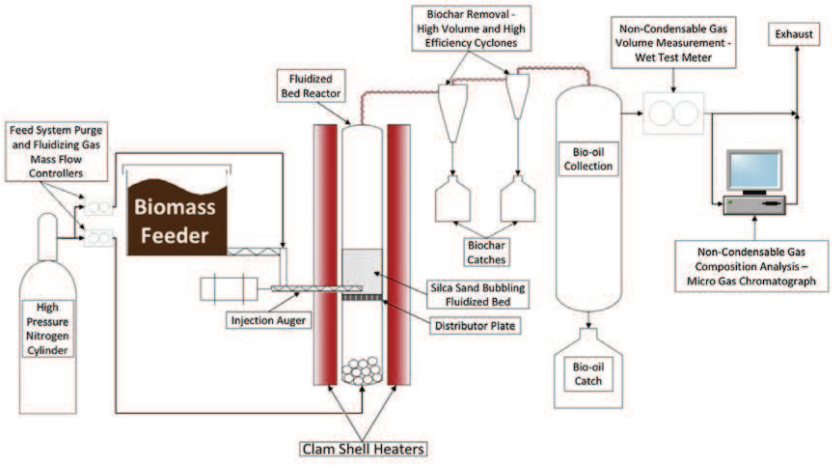

Figure 1-5: Flow diagram of the fluidized-bed pyrolysis reactor system.

As shown in Figure 1-5, biomass enters the reactor near the bottom of the sand bed through a nitrogen entrainment system. The bubbling fluidized bed reactor consists of a stainless steel pipe of 0.34 m in height and with an internal diameter of 38.1 mm. Ceramic clamshell heaters are used to maintain the reactor temperatures at 500 °C for fast pyrolysis. In a separation train, the solid char particles are first separated using two cyclones. A bio-oil collection system condenses the gaseous tar. After the fluidized bed reactor, the produced tar has to be condensed as soon as possible in order to prevent further degradation at high temperatures. An optimal design of the separation section is thus crucial for a high bio-oil yield [30].

CFD model description

With today's computational power, the Eulerian method is one of the most affordable multiphase CFD modeling approaches for performing simulations of an industrial-scale gas-solid flow system and has widely been used for various gas-solid simulations. In the next sections a detailed description will be given of the methodology used to simulate biomass fast pyrolysis. The focus will be on the classical fluidized bed riser reactors. Although various papers describe the CFD studies on fast biomass pyrolysis. The following description is based on the work of Xue et al. [31]. First the kinetic reaction network will be discussed before discussing the numerical framework.

Chemical kinetic model of single biomass particle pyrolysis

The chemical process of biomass fast pyrolysis is extremely complex and may involve hundreds of species and reactions. Details of the process are largely unknown so global devolatilization schemes have been used to simulate the fast biomass pyrolysis reaction scheme. Xiong et al. compared the three most used devolatilization schemes to experimental data [32]. In global reaction schemes, lumped reactants and products are connected via several simplified reactions [33]. In most schemes biomass will decompose into non-condensable pyrolysis gases, a gaseous tar fraction which is later condensed and a solid char fraction. In the next three devolatilization schemes the solid char, liquid tar and non-condensable gas are assumed to be individual chemical components.

The most basic devolatilization scheme used is the single-component single-step mechanism, where biomass is decomposed through three parallel reactions into three products: organic liquid, gas and char. All reactions are modeled using first-order irreversible reactions rates. This reaction scheme is used in various publications. Boateng et al. [34] used this scheme to model the space-time evolution of fast biomass pyrolysis. Yu et al. [35] applied this devolatilization scheme in order to study the biomass pyrolysis in a downer reactor equipped with a gas-solid separator.

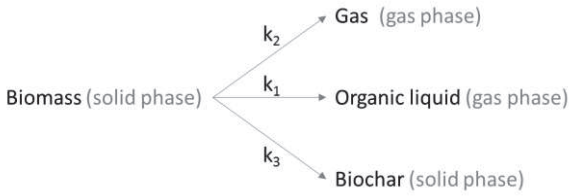

Figure 1-6: Reaction steps for the single-component single-step devolatilization scheme.

A more elaborate devolatilization scheme considers the secondary organic liquid cracking [36]. In this second reaction scheme organic liquid will decompose into gas and char in parallel reactions in addition to the primary competitive biomass decomposition. This secondary devolatilization scheme as shown in Figure 1-7 is also known as the single-component multiple-step mechanism.

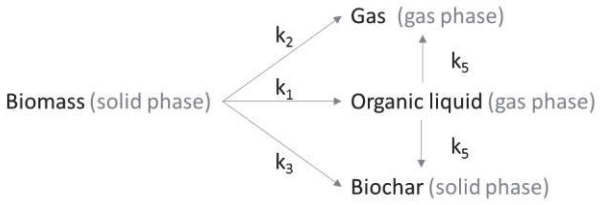

Figure 1-7: Reaction steps for the single-component multiple-step devolatilization scheme.

The third reaction mechanism is the Broido-Shafizadeh scheme. It can be described as a multiple-component multiple-step reaction mechanism. This scheme assumes that biomass is composed of the three components: cellulose, hemicellulose and lignin; and the pyrolysis rate is said to be related to its composition:

$$\text{Biomass} = \alpha\ \text{Cellulose} + \beta\ \text{Hemicellulose} + \gamma\ \text{Lignin}$$

The total pyrolysis rate of the biomass is considered to be the sum of the rates of the three main components. This reaction scheme is the most used devolatilization scheme in order to simulate the thermal decomposition of various sources of biomass [30, 31, 37-47].

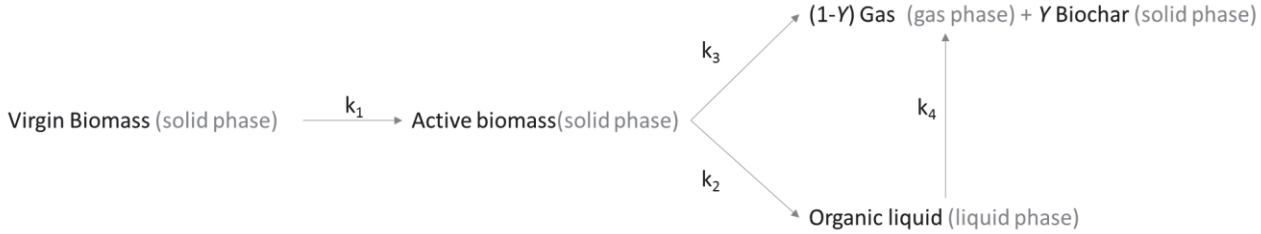

Figure 1-8: Reaction steps for the multiple component multiple-step devolatilization scheme.

All reactions are modeled with the first-order Arrhenius kinetics depending on a pre-exponential factor A, an activation energy E and temperature T:

$$k = A \exp(-\frac{E}{RT}) \tag{1.1}$$

Other reaction schemes have also been proposed through the years. Mellin et al. [48] used a multiple-component single-step devolatilization schemeand later used a more elaborate scheme with a broader product distribution [49, 50]. However these more elaborate devolatilization schemes focus on a more detailed pyrolysis gas composition, but the most important product of fast biomass pyrolysis for fuel production is the tar phase. More detailed reaction schemes are used in simulating gasification processes since in gasification processes the produced gas phase is the primary product.

The pyrolysis devolatilization data for the Broido-Shafizadeh scheme is given in Table 1-2 [51-53]. The subscript "v" and "a" indicate the virgin and activated forms of biomass. Fractional char formations for cellulose, hemicellulose and lignin are 0.35, 0.60 and 0.75 kg char per kg biomass respectively.

Table 1-2 shows the various elementary reaction steps in the Broido-Shafizadeh scheme with the corresponding data obtained from literature. This multiple-component multiple-step reaction mechanism is the selected fast biomass pyrolysis model for the rest of the study, since it gives the best agreement with experimental setups. The biomass components cellulose, hemicellulose and lignin are abbreviated as CL, HC and LG respectively.

Table 1-2: Pyrolysis devolatilization data for the multiple-component multiple-step reaction mechanism [53-55].

	Reaction	ΔH_r (kJ/kg)	A_f (1/s)	E_A (kJ/mol)	k_r @ 773 K (1/s)
1a	$CL_v \rightarrow CL_a$	0	2.80×10^{19}	242.4	1170
1b	$HC_v \rightarrow HC_a$	0	2.10×10^{16}	186.7	5080
1c	$LG_v \rightarrow LG_a$	0	9.60×10^{8}	107.6	51.4
2a	$CL_a \rightarrow$ tar	255	3.28×10^{14}	196.5	17.3
2b	$HC_a \rightarrow$ tar	255	8.75×10^{15}	202.4	184
2c	$LG_a \rightarrow$ tar	255	1.50×10^{9}	143.8	0.287
3a	$CL_a \rightarrow$ 0.35 char + 2.6 Pgas	-20	1.30×10^{10}	150.5	0.878
3b	$HC_a \rightarrow$ 0.60 char + 1.6 Pgas	-20	2.60×10^{11}	145.7	37.1
3c	$LG_a \rightarrow$ 0.75 char + Pgas	-20	7.70×10^{6}	111.4	0.228
4	tar → 4 Pgas	-42	4.25×10^{6}	108.0	0.214

Implementation of a kinetic model in source terms

The kinetic model and reaction constants are developed based on a small particle assumption, in a way that internal transport phenomena are ignored. In a multi-fluid CFD approach, instead of modeling individual particles, the particles are treated as a continuous phase. Reaction equations for all of the phases are given in Table 1-3:

Table 1-3: Reaction rates for all phases and species.

Component	Reaction rate*
CL_v	$R_{CL_v} = -k_{1a}\rho_S\varepsilon_S X_{CL_v}$
HC_v	$R_{HC_v} = -k_{2a}\rho_S\varepsilon_S X_{HC_v}$
LG_v	$R_{LG_v} = -k_{3a}\rho_S\varepsilon_S X_{LG_v}$
CL_a	$R_{CL_a} = k_{1a}\rho_S\varepsilon_S X_{CL_v} - \rho_S\varepsilon_S X_{CL_v}(k_{2a}+k_{3a})$
HC_a	$R_{HC_a} = k_{2a}\rho_S\varepsilon_S X_{HC_v} - \rho_S\varepsilon_S X_{HC_v}(k_{2b}+k_{3b})$
LG_a	$R_{LG_a} = k_{3a}\rho_S\varepsilon_S X_{LG_v} - \rho_S\varepsilon_S X_{LG_v}(k_{2c}+k_{3c})$
tar	$R_{tar} = k_{2c}\rho_S\varepsilon_S X_{CL_a} + k_{2b}\rho_S\varepsilon_S X_{HC_a} + k_{2c}\rho_S\varepsilon_S X_{LG_a} - k_4\rho_g\varepsilon_g X_{tar}$
gas	$R_{gas} = k_{3a}\rho_S\varepsilon_S X_{CL_a}(1-\Upsilon_{CL}) + k_{3b}\rho_S\varepsilon_S X_{HC_a}(1-\Upsilon_{HC}) + k_{3c}\rho_S\varepsilon_S X_{LG_a}(1-\Upsilon_{LG}) + k_4\rho_g\varepsilon_g X_{tar} + \left[\rho_S\varepsilon_S X_{CL_a}(k_{2a}+k_{3a}) + \rho_S\varepsilon_S X_{HC_a}(k_{2b}+k_{3b}) + \rho_S\varepsilon_S X_{LG_a}(k_{2c}+k_{3c})\right].\frac{\rho_g}{\rho_b} + \left[\rho_S\varepsilon_S X_{CL_a}k_{3a}\Upsilon_{CL} + \rho_S\varepsilon_S X_{HC_a}k_{3b}\Upsilon_{HC} + \rho_S\varepsilon_S X_{LG_a}k_{3c}\Upsilon_{LG}\right].\frac{\rho_g}{\rho_c}$
$char_s$	$R_{char_s} = k_{3c}\rho_S\varepsilon_S X_{CL_a}\Upsilon_{CL} + k_{3b}\rho_S\varepsilon_S X_{HC_a}\Upsilon_{HC} + k_{3c}\rho_S\varepsilon_S X_{LG_a}\Upsilon_{LG}$
$char_g$	$R_{char_g} = -\left[\rho_S\varepsilon_S X_{CL_a}(k_{2a}+k_{3a}) + \rho_S\varepsilon_S X_{HC_a}(k_{2b}+k_{3b}) + \rho_S\varepsilon_S X_{LG_a}(k_{2c}+k_{3c})\right].\frac{\rho_g}{\rho_b} - \left[\rho_S\varepsilon_S X_{CL_a}k_{3a}\Upsilon_{CL} + \rho_S\varepsilon_S X_{HC_a}k_{3b}\Upsilon_{HC} + \rho_S\varepsilon_S X_{LG_a}k_{3c}\Upsilon_{LG}\right].\frac{\rho_g}{\rho_c}$

** In these expressions, only the non-zero changes in mass due to the pyrolysis chemistry are shown.*

Conservation laws for the gas phase

In the multi-fluid CFD model, gas and solid phases are treated as interpenetrating continua in an Eulerian framework. The gas is considered as the primary phase, whereas the solid phases are considered as secondary phases. Each solid phase is distinguished by its physical and thermal properties. The primary and dispersed phase are linked by tracking the phase volume fractions in a finite-volume frame. These volume fractions are assumed to be dependent on space and time. By definition, the volume fractions of all the phases must sum up to unity:

$$\varepsilon_g + \sum_{m=1}^{M} \varepsilon_{s_m} = 1 \tag{1.2}$$

The gas phase is formulated through a set of conservation equations for mass, momentum and energy. The continuity equation for the gas phase is:

$$\frac{\delta \varepsilon_g \rho_g}{\delta t} + \nabla . \left(\varepsilon_g \rho_g \vec{u}_g\right) = R_g \tag{1.3}$$

With ρ_g the density of the gas, $\vec{u}_g$ the gas velocity and R_g the interphase mass transfer terms from the dispersed solid phase due to surface chemistry. The momentum equation for the gas phase is:

$$\frac{\delta \varepsilon_g \rho_g \vec{u}_g}{\delta t} + \nabla . \left(\varepsilon_g \rho_g \vec{u}_g \vec{u}_g\right) = \nabla . \vec{S}_g + \sum_{m=1}^{M} \vec{I}_{gm} + \varepsilon_g \rho_g \vec{g} \tag{1.4}$$

Where $\vec{S}_g$ is the second-order stress tensor for the gas. $\vec{I}_{gm}$ is an interaction force representing the momentum transfer between the gas ant the mth solid phase. $\vec{g}$ represents the gravity vector. The momentum exchange included in $\vec{I}_{gm}$ due to mass transfer from solid phase m to the gas phase is described as:

$$\sum_{n=1}^{N} R_{smn}(\xi_{gm}\vec{u}_{sm} + (1-\xi_{gm})\vec{u}_g) \text{ with } \xi_{gm} = \begin{cases} 0 \; if \; \sum_{n=1}^{N} R_{smn} < 0 \\ 1 \; if \; \sum_{n=1}^{N} R_{smn} \geq 0 \end{cases} \tag{1.5}$$

The energy equation for the gas phase is given by:

$$\varepsilon_g \rho_g C_{pg} \left(\frac{\partial T_g}{\partial t} + \vec{u}_g . \nabla T_g\right) = \nabla . \vec{q}_g - \sum_{m=1}^{M} H_{gm} - \Delta H_{rg} + H_{wall}(T_{wall} - T_g) \tag{1.6}$$

Where $\vec{q}_g$ is the gas-phase conductive heat flux. H_{gm} describes the fluid-solid interphase heat transfer between the gas and the mth solid. ΔH_{rg} is the heat of reaction in the gas phase. The last term takes the heat loss through the wall into account.

Conservation equations for the solid phases

The solid phases are also formulated through a set of conservation equations for mass, momentum and energy. The continuity equation for a solid phase m is analogously to the gas phase given by:

$$\frac{\partial \varepsilon_{sm}\rho_{sm}}{\partial t} + \nabla.(\varepsilon_{sm}\rho_{sm}\vec{u}_{sm}) = R_{sm} \tag{1.7}$$

Where ρ_{sm} stands for the density, $\vec{u}_{sm}$ is the velocity of the solid phase m and R_{sm} the mass transfer term. The momentum equation for the solid phase m is described as:

$$\frac{\partial \varepsilon_{sm}\rho_{sm}\vec{u}_{sm}}{\partial t} + \nabla.(\varepsilon_{sm}\rho_{sm}\vec{u}_{sm}\vec{u}_{sm}) = \nabla.\vec{S}_{sm} + \vec{I}_{gm} - \sum_{l=1,l\neq m}^{M} \vec{I}_{ml} + \varepsilon_{sm}\rho_{sm}\vec{g} \tag{1.8}$$

The energy equation of the mth solid phase as a function of the solid-phase temperature T_{sm} is given by the expression:

$$\varepsilon_{sm}\rho_{sm}C_{psm}\left(\frac{\partial T_{sm}}{\partial t} + \vec{u}_{sm}.\nabla T_{sm}\right) = \nabla.\vec{q}_{sm} + \sum_{m=1}^{M} H_{gm} - \Delta H_{rsm} \tag{1.9}$$

A Newtonian closure is used for the stress tensors. Momentum transfer between the fluid and particulate phases is accounted for using the Gidaspow model in Fluent [56]. Solid/solid momentum exchange is addressed with the Fluent-recommended Syamllal-O'Brien symmetric drag model [57]. Heat exchange between the gas and the particulate phases is accounted for using the Gunn model, which is recommended by Fluent for gas-solid interactions [58]. Heat transfer between solid phases is modeled using a simple user-defined radiative heat transfer expression. The gas phase is assumed to not participate in radiative heat transfer.

$$Q_i = \left(\frac{6}{d_p}\right).\frac{\epsilon.\sigma}{\varepsilon_s}.\sum\nolimits_{solids}\varepsilon_m(T_m^4 - T_i^4) \tag{1.10}$$

The volumetric heat source, Q_i, for a specific phase is given in function of the particle diameter, d_p, the emissivity of the material, ϵ, which is assumed to be 0.75 for all particulate phases, the total solids volume fraction, ε_s, and the volume fraction, ε_m, of the solid phase, m. The Stephan-Boltzmann radiation constant has a value of 5.676 $\times 10^{-8}$ W/m^{2}K^4.

Xiong et al. [59] modeled the effects of interphase transport coefficients on fast biomass pyrolysis in fluidized riser reactors. Since numerical modeling of sub-grid structures can affect the evolution of interphase transport coefficients and influence the predictive capability of coarse-grid computational fluid dynamics models in simulating fluidized-bed reactors, different formulations of drag and heat transfer coefficients were employed and compared to experimental results. The base equations used for drag force coefficient correlations were the Gidaspow, Syamlal-O'brien and EMMS model. For the heat transfer correlations the Ranz-Marshall, Gunn and Li-Mason models were compared. The research concluded that the EMMS drag model gives the most accurate results compared to the experimental data since the EMMS model considers a more detailed sub-grid structure. These effects were investigated inside a gravitational fluidized bed reactor[*]. The energy minimization multi-scale (EMMS) model shows encouraging results for simulations where particle clustering occurs [60]. The choice of the heat transfer model only slightly influences the product distribution because of the relatively short response time for the adjustment of the interphase temperature difference compared to the long response time for the adjustment of the interphase slip velocity which is determined by the drag coefficients [59]. Because of the relatively short response time for the adjustment of the interphase temperature difference, heat transfer between two phases takes place immediately. As a result, nearly the same temperature profiles were predicted for the different heat transfer models.

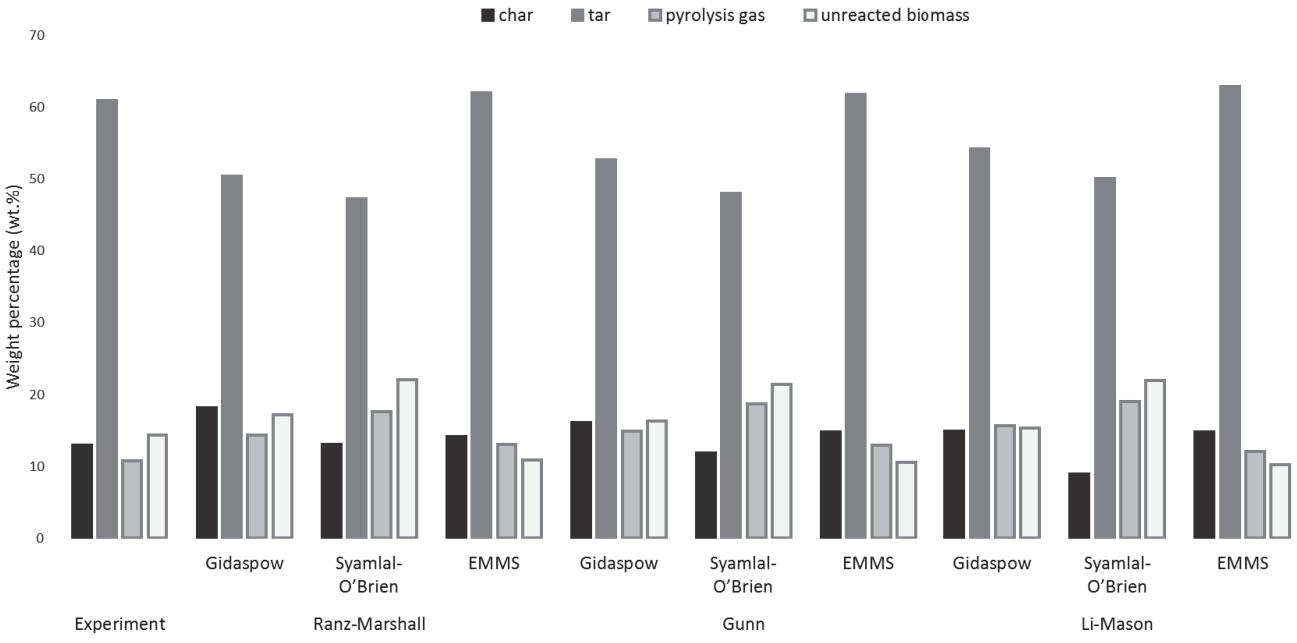

Figure 1-9: Product distribution for CFD modelling of fast biomass pyrolysis for various heat transfer and mass transfer models compared to the experimental yield.

[*] In the numerical simulations performed in a gas-solid vortex reactor higher shear forces are present, preventing particle clustering. In that case the Gidaspow model is assumed to be appropriate.

Computational Fluid Dynamics simulations of Fast Biomass Pyrolysis in Fluidized bed reactors

Throughout the years various publications have been made on Computational Fluid Dynamics simulations for fluidized bed reactors. This chapter will give an overview of the most important publications in the field of computational fluid dynamics simulations of fast biomass pyrolysis in fluidized bed reactors.

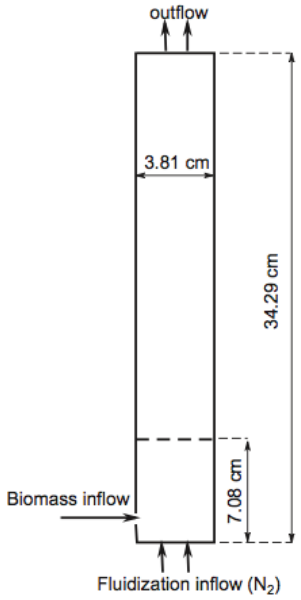

Figure 1-10: Representation of a classical fluidized bed reactor setup.

Papadikis et al. published various papers on the fast biomass pyrolysis process by adopting the Lagrangian approach for particle tracking while the flow of the inert gas was treated with the standard Eulerian method for gases using a single-component two-step reaction mechanism. This way radial temperature and density distributions were obtained for discrete particles [46]. Momentum transport in bubbling fluidized beds was investigated by calculating forces exerted on the particle as well as calculating its velocity components for both 2-D and 3-D simulations. The drag force induced by the carrier fluid surrounding the particle is the major parameter that defines the particle motion. Regions with higher sand concentrations induce greater amounts of drag force and the virtual mass effect becomes less important and noticeable. The hydrodynamics behavior of the bed changed significantly from the 2-D to the 3-D case. Simulations showed that bubble formation close to the feeding point of the reactor reduced the drag force at the injection point compared with the 2-D case [42], suggesting that 3-D simulations are required to accurately capture phenomena at the biomass feeding inlet.

In later publications Papadikis et al. [43] focused more on heat, momentum and mass transport in bubbling fluidized beds. Different particle shrinkage models were compared and it was concluded that biomass shrinkage inside a bubbling bed doesn't affect the momentum transport significantly. The effect of shrinkage on product yield and pyrolysis time can be neglected for small particle sizes (350-500 µm) [44]. But the biomass particles have to be small due to feeding problems anyway. 350 µm and 550 µm diameter biomass particles, respectively smaller and larger than the 440 µm sand particles in the reactor, were compared. The use of different particle sizes results in different heat transfer mechanisms, altering the heat transfer coefficient, which will influence the temperature profiles at the surfaces and the centers of the biomass particles. However if the residence time is kept below two seconds, product yields will be similar. In this publication the volume occupied by the solid structure of the particle is assumed to decrease linearly with the biomass mass and to increase with the char mass, as devolatilization takes place. This shrinkage effect where a char layer is formed on the degrading biomass particle is not possible in Eulerian-Eulerian simulations. This study concluded that small biomass particles are preferred for fast pyrolysis applications in fluidized beds since they provide a good heat transfer mechanism. Also, smaller particle sizes reduce the effect of secondary reactions resulting in higher bio-oil yields [45].

Xue et al. [31] proposed a Euler-Euler multiphase CFD model for continuous fast pyrolysis of biomass in a fluidized bed reactor. A multi-stage kinetic model was applied to describe the devolatilization scheme. This publication appears to be the first in literature where a steady-state condition is achieved in a fluidized bed reactor. The product yields for the fast biomass pyrolysis of bagasse with a composition of 36 % cellulose, 47 % hemicellulose and 17 % lignin were 14.4 wt% char, 63.4 wt% tar and 21.5 wt% pyrolysis gas.

In later publications, model predictions are compared to experimental data produced in a lab-scale reactor as shown in Table 1-4. A parametric study of operating conditions was performed. Results indicate that biomass particle size and superficial gas velocity influence tar yield and residence time considerably [39]. Particle sizes varying from 200 µm to 1200 µm were investigated. Biomass particles with a particle diameter smaller than 500 µm appear to have a decrease in tar product yield and an increase of unreacted biomass. Increasing the diameter up to 900 µm appears to significantly increase tar yield from around 50 wt% for 450 µm particles to 65 %. For larger biomass particles no further difference was observed. The same phenomena was observed for the variation of product yields with respect to the nitrogen velocity. An increase of 20 % tar product yield was achieved by increasing the nitrogen velocity from 0.3 m/s to 0.6 m/s. For the range of operating temperatures studied, the kinetic model seemed to capture the trend of biomass decomposition and an optimal temperature of 500 °C for bio-oil production was reported [30].

Table 1-4: Product yields of fast biomass pyrolysis in a fluidized bed reactor, experimental results of red oak pyrolysis compared to CFD simulations with various particle diameters.

	Char (wt%)	Tar (wt%)	Pyrolysis gas (wt%)
Experiment	13.0	71.7	20.5
Simulation (d_p= 250 µm)	12.3	60.5	16.2
Simulation (d_p= 325 µm)	14.1	62.4	17.3
Simulation (d_p= 400 µm)	15.1	63.4	18.1

Xue et al. also reported that there is a good agreement for the product yields between the 2-D and 3-D simulations for fluidized bed reactors at steady-state. In later studies only the 2-D case is simulated since it reduces the computational time significantly [30].

Table 1-5: Product yields of fast biomass pyrolysis 2-D and 3-D simulations in a fluidized bed reactor.

	Char (wt%)	Tar (wt%)	Pyrolysis gas (wt%)
2D	14.0	63.5	20.5
3D	13.5	62.6	21.7

A generalized numerical framework for simulating biomass fast pyrolysis in fluidized-bed reactors was developed by Xiong et al. [41] The capability of this framework was tested by simulating a laboratory-scale bubbling fluidized bed reactor and the simulation results were validated by experimental data. These simulation results indicate that as the location of the reactor inlet is elevated or as the superficial velocity of feeding is increased, the tar yield will increase due to the reduced residence time. Less tar will be converted to syngas by secondary cracking reactions. Later this numerical framework was used to generate a BIOmass Thermochemical Conversion (BIOTC) code, a computer program within the framework of OpenFOAM which provides users freedom to extend this code by inserting sub-models while maintaining the user-friendly interface [40].

Table 1-6: Experimental fast biomass pyrolysis of cellulose results compared to the simulations of the BIOTC code [27].

	Char (wt%)	Tar (wt%)	Pyrolysis gas (wt%)
Experiment	13.0	71.7	20.5
Simulation	14.6	60.7	28.3

As previously discussed Xiong et al. [59] modeled the effects of drag force coefficients and heat transfer coefficients on fast biomass pyrolysis in fluidized beds. The research concluded that the EMMS drag model gives the most accurate results compared to the experimental data for gravitational fluidized-bed reactors. The choice of the heat transfer model only slightly influenced the

product distribution because of the relatively short response time for the adjustment of the interphase temperature difference.

One of the most extensive papers published by Xiong et al. [39] on the operating conditions of biomass fast pyrolysis in fluidized bed reactors investigates the influence of the wall side temperature, the temperature of nitrogen and the velocity of nitrogen on the product yields of a biomass fast pyrolysis riser reactor. It was observed that a wall temperature of 520 °C maximizes the tar yield. Also for the inlet temperature of nitrogen a maximum in tar yield was observed at 540 °C. These results agree with literature given that secondary cracking reactions are favored at high temperatures. The variation of product yields with respect to increasing nitrogen velocity results in a decrease of biochar and gas yield with an increasing amount of unreacted biomass. This is due to a reduced residence time resulting in a reduced secondary tar cracking but also a reduction in the primary decomposition reaction [39].

The biomass particle diameter was also varied from 200 to 1200 µm with an increasing tar product yield up to 65 wt% for a biomass particle diameter of 900 µm. For larger particles the biomass conversion yields seemed to be insensitive to the variation in biomass particle diameter. Product yields seemed to be independent of biomass feed rate in the range of 1.6 to 2.6 kg/h. All these results correspond with previously observed responses for both simulations and experiments. In the existing literature however, the effects of sand particle diameter have not been characterized yet. This research predicts an increase in tar yield up to a sand diameter of 800 µm, this observation gives a biased representation. It has to be noted that by increasing the sand diameter, the minimum fluidization velocity increases, resulting in a bed that is more difficult to be fluidized. So for increasing sand particle sizes, the nitrogen inlet velocity has to be increased. Therefore it is more correct to plot the product yields in function of the nitrogen inlet velocity [39].

Mellin et al. [48] developed a 3D Euler-Euler CFD model with a single-component single-step reaction mechanism as a way of predicting vapor phase dynamics and product distributions of fast biomass pyrolysis in fluidized bed reactors. In later research a more elaborate reaction scheme was developed, taking into account the complex breakdown of each biomass subcomponent. These reactions focus more on thermal cracking of tar compounds [49].

Mellin et al. [61] also investigated the possibility to use steam as fluidizing agent instead of nitrogen. Both profiles of primary product formation rates are comparable: steam results in a negligible increase of heat flux to the biomass. Although a comprehensive gas-phase kinetic model is required to further investigate the effects of steam since secondary reactions are not taken into account.

1.3.2. Other fluidized bed reactors

Fast pyrolysis for the production of liquid tar has developed considerably since the first experiments in the late 1970s [62]. Many reactors and processes have been investigated and developed to the point where fast pyrolysis is now an accepted feasible and viable route to renewable liquid fuels, chemicals and derived products. A wide range of reactor configurations, that show considerable diversity and innovation in meeting the basic requirements of fast pyrolysis, has been investigated. There is currently no “best available technology” with most established processes giving liquid yields between 67 - 75 %, based on dry biomass weight [13]. The main points of focus when designing a reactor for fast biomass pyrolysis are: very high heating and heat transfer rates, moderate and carefully controlled temperature and rapid cooling or quenching of the pyrolysis vapors [63, 64].

Taking these design specifications into account a lot of alternative reactors have been designed for fast biomass pyrolysis. The most discussed in scientific literature are the ablative reactor, circulating fluid bed reactor, entrained flow reactor, rotating cone reactor…

In order to get acquainted with all these available reactor types for fast biomass pyrolysis the reader is redirected to various reviews for further details [13, 17]. The reactor types that will be discussed here are the reactors wherefore computational fluid dynamics simulations for fast biomass pyrolysis have been performed.

Choi et al. [65] performed a computational fluid dynamics study using a Eulerian-Eulerian approach to investigate the fast pyrolysis characteristics of 200 µm diameter woody biomass particles in an inclined gravitational reactor. The inlet conditions and inclination angle of the reactor setup were changed in order to study their effects on the reaction. To analyze the pyrolysis reaction of the reactor, semi global two-stage chemical kinetics including a tar cracking mechanism was applied. This research concluded that the geometric shape and length of the reactor should be carefully designed in order to prevent secondary tar cracking.

A CFD study of biomass pyrolysis in a downer reactor equipped with a novel gas-solid separator was performed by Yu et al. A multi-fluid Eulerian-Eulerian model with constitutive relations adopted from the kinetic theory of granular flow was used to simulate the multiphase flow. Compared to other available biomass pyrolysis technologies, the proposed reactor, arranged in a dual fluidized bed system was found to be a viable option to ensure a narrow residence time distribution of the gas phase, as well as quick and efficient separation of the gas from the solid phase sand particles with an average diameter of 188 µm. This downer reactor setup was compared to a fluidized bed reactor. This study presented a robust CFD model for the simulation of the fast pyrolysis of biomass using a one-step global pyrolysis reaction scheme. The proposed separation mechanism has the potential to

achieve a separation efficiency over 99.9 % while allowing control of the pyrolysis gas residence time within 2 s. The multi-phase flow mixture shows a uniform temperature distribution along the reactor. The temperature profile confirms a short thermal entrance length, which is a desired feature for fast biomass pyrolysis [35, 66].

Another type of reactor type for fast biomass was proposed by Aramideh et al. Computational Fluid Dynamics simulations of biomass fast pyrolysis processes were conducted both in the fluidized-bed and the auger reactor. This auger reactor concept features a screw that mixes biomass with a heated bulk solid material that serves as a heat transfer medium. In this case chemical reactions were simulated using a multi-step reaction mechanism that considers multiple compounds in biomass and various gaseous species. The motion of the rotating screw in the auger reactor was modeled using the so-called rotating reference frame. The predicted product yields were found to agree well with the experimental data. The parametric study performed showed an optimal wall temperature for tar production of 823 K. High pre-treatment temperature of the biomass slightly decreased the tar yield and increases the syngas yield. A higher nitrogen inlet velocity resulted in a higher tar yield because of the shorter vapor residence time. It was also found that more unreacted biomass exited the reactor if the biomass feed rate was excessive, indicating the limitation of the auger reactor at high biomass feed rate [67].

1.4. Gas-solid vortex reactor

In the gas-solid vortex reactor (GSVR) a fluidized bed is generated in a centrifugal field by introducing the gas via tangential injection slots into the reactor chamber. The essential features for a fast pyrolysis process are very high heating and heat transfer rates, a carefully controlled temperature of about 500 °C and a rapid cooling of the pyrolysis vapors to give the bio-oil product [13]. The gas-solid vortex reactor (GSVR) meets all three criteria because of the high gas-solid slip velocities that result in high convective heat and mass transfer coefficients and the very short gas-phase residence time in the reactor.

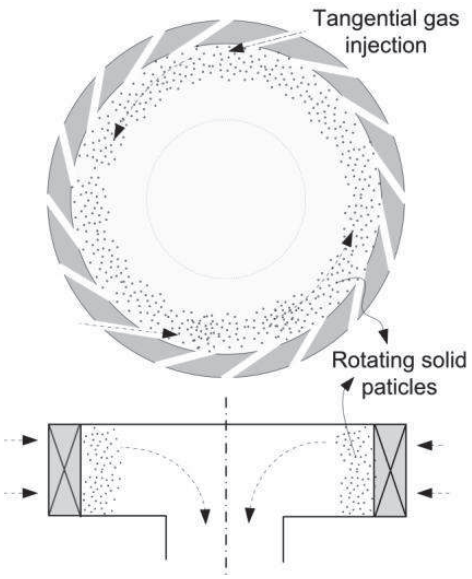

Figure 1-11: Schematic representation of the GSVR experimental setup with tangential feed inlets. Front view and side view [68].

1.4.1. Set-up of a gas-solid vortex reactor

The GSVR, also referred to as Rotating Fluidized Bed in Static Geometry (RFB-SG), is a novel fluidized reactor, allowing process intensification. The past decades have seen a relative resurgence of RFB-SG research in several different fields including nuclear technologies [69, 70], drying applications [71, 72] and chemical reactions [73-77]. The RFB-SG geometry has characteristics in between those of fluidized bed and packed bed reactors. These unique attributes allow it to significantly improve yields of processes that suffer from convective heat or mass-transfer limitations. Rotating fluidized beds (RFB), where the overall reactor geometry is rotated mechanically, is similar to GSVR and should be acknowledged as a competitor technology and as a source of information. These reactors share many of the same operating principles with a GSVR, but with increased mechanical complexity that comes with large rotating parts such as complex sealing, mechanical vibrations and wear and tear [78]. Both reactor types replace the gravitational force by a stronger centrifugal force. The centrifugal force of a RFB is generated by mechanically rotating the reactor vessel and sending in fluidizing gas

perpendicular to the reactor wall. In a RFB-SG the centrifugal field is introduced in a static disc-shaped geometry by the tangential injection of the gas phase through the injection slots. The main advantage of RFB over RFB-SG is that for rotating fluidized bed reactors the gas flow rate and the rotational velocity of the bed can be set independently.

The main advantage of all types of centrifugal reactors over gravitational fluidized riser reactors is that particles can be fluidized against a high-gravity (high-G) field. The radial fluidization of the particle bed is controlled by balancing the drag force exerted on the particles by a radially inwards flowing gas and the centrifugal force exerted on the particles radially outwards due to inertia of rotation. High-G fluidized beds can be operated densely and more uniformly at higher gas-solid slip velocity and, therefore, at intensified interfacial transfer of mass, momentum and heat [78-80]. The slip velocity is defined as the vector difference between the bulk gas-phase fluid velocity and the particle solids velocity.

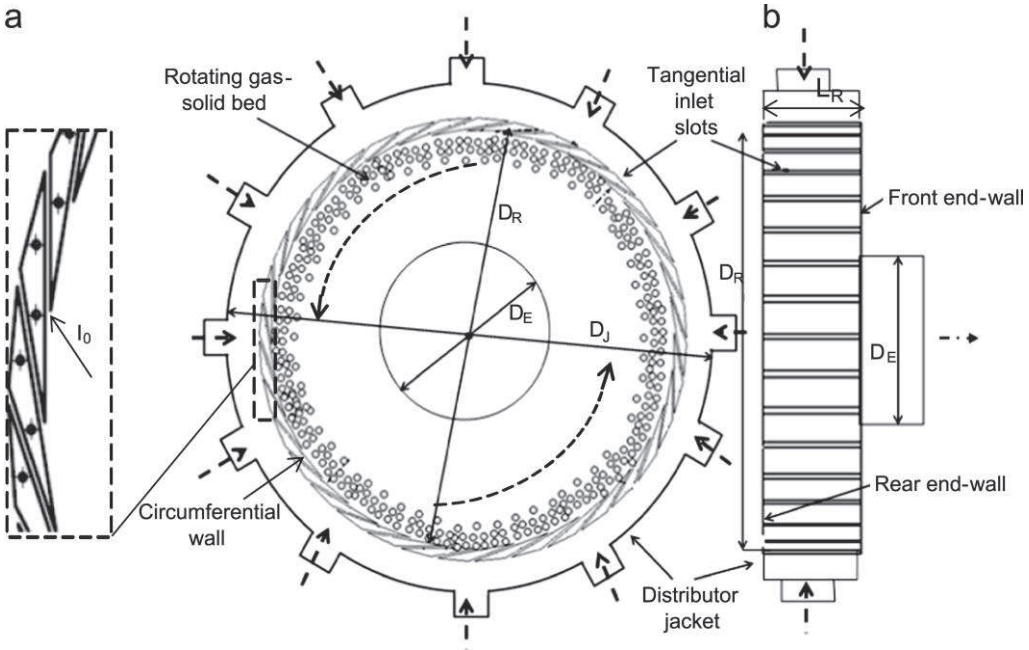

Figure 1-12: Schematic presentation of the GSVR experimental setup with tangential feed inlets. (a) Front view and (b) side view [81].

The work of Kovacevic et al. gives detailed information about the experimental setup of a GSVR at the Laboratory of Chemical Technology at Ghent University [82]. The gas-solid vortex reactor consists of two concentric cylinders, the distributor jacket and the reaction chamber. The front and rear end-wall of the cylinder is made of transparent polycarbonate glass (Makrolon®), allowing a visual observation of the rotating bed. The distributor jacket has 12 radial inlet distributor pipes, while the main reactor chamber composes of 36 tangentially inclined injection slots uniformly distributed along the circumferential wall, positioned at a 10° angle with respect to the tangent. A more detailed description of the reactor dimensions is given in Table 1-7:

Table 1-7: GSVR geometry and dimensions of the experimental setup.

Variable	Notation	
Distributor jacket diameter	D_J	0.68 m
Reactor diameter	D_R	0.54 m
Exhaust diameter	D_E	0.2 m
Reactor length	L_R	0.1 m
Number of jacket inlets	I_J	12
Number of reactor inlets-slots	I_N	36
Injection slot thickness	I_O	2 mm
Injection angle	ϑ	10°

Computational Fluid Dynamics simulations of gas-solid vortex reactors have only recently been reported in scientific publications. J. De Wilde et al. performed a numerical investigation of gas-solid heat transfer in rotating fluidized bed reactor in a static geometry [79]. A comparison with conventional gravitational fluidized beds was made. The higher specific fluidization gas flow rates and increased gas-solid slip velocities drastically increased the rate of gas-solid heat transfer. Bubble formation is also much less pronounced compared to the classical riser reactors, resulting in a more homogeneous fluidized bed [83-85]. Furthermore, rotating fluidized beds have a particle bed "width"-to-"height"-ratio much higher than conventional fluidized beds, in combination with higher allowable gas-solid slip velocities. The "width"-to-"height"-ratio of the vortex reactor can be calculated by dividing the reactor diameter by the reactor length. The higher gas-solid slip velocities allow to operate rotating fluidized beds in a static geometry at fluidization gas flow rates drastically higher than conventional fluidized beds. These combined properties make the GSVR reactor interesting for highly endothermic or exothermic reactions [79].

1.4.2. Fast Biomass Pyrolysis in a gas-solid vortex reactor

Fast biomass pyrolysis in a gas-solid vortex reactor was modelled using Computation Fluid Dynamics by Ashcraft et al. [86]. Pyrolysis of lignocellulosic biomass was modelled in order to assess the potential process intensification abilities. The production of pyrolysis gases, tar and char products was examined for various operating conditions using the previously discussed Broido-Shafizadeh reaction network [87]. The same GSVR reactor as described in Table 1-7 was modeled.

The CFD software package ANSYS Fluent 15.0 was used to perform the calculations. The reactor was modeled with a 2-D projection of 1/9th of the actual reactor using rotational periodic boundary conditions in order to reduce the computational cost of the simulations significantly. The non-reacting flow simulations of a 40° section showed that the primary observables, such as pressure drop, bed thickness, solids velocity and general bed structure were nominally the same as the values obtained from when simulating 360° geometry.

A constant mass of sand of 5 kg was chosen for the various simulations performed by Ashcraft, however the sand mass will affect the bed dynamics and hydrodynamics to some extent. [81, 88] The different operating conditions include: (1) an increased gas inlet temperature with increased volumetric gas flow rate to achieve the same inlet gas mass flow rate, (2) a case where dry biomass is injected, (3) cases with increasing reactor throughput in order to investigate process intensification possibilities and (4) operating conditions where no sand is present in the reactor but char is used as the heat transfer agent. A more detailed overview of the operating conditions is shown in Table 1-8.

Table 1-8: Independent operating variables for the GSVR simulation cases [86].

	T_{gas}^{inlet}(°C)	Inlet gas feed rate (kg/s)	Inlet gas volumetric flow rate (m³/s)	$T_{biomass}^{feed}$(°C)	Biomass feed rate (kg/s)	Biomass water (dry basis) (wt%)
Base	650	0.222	0.60	27	0.0348	10
(1) 973 K	650	0.222	0.63	27	0.0348	10
(2) No-water	650	0.222	0.60	27	0.0348	0
(3) 1.5x flow	650	0.333	0.90	27	0.0522	10
(3) 2x flow	650	0.444	1.20	27	0.0696	10
(4) No-sand	650	0.222	0.60	27	0.0348	10
(4)No-sand/No-water	650	0.222	0.60	27	0.0348	0

As shown in Table 1-9, the two cases that resulted in a higher gas outlet temperatures and higher average solids temperatures, achieved a reactor temperature closer to the recommended 500°C. The no-water case results in higher overall reactor temperatures keeping the same 650 °C inlet temperature as for the Base case, because energy is not needed to heat up and vaporize the water. The product distribution produced by both high-temperature cases results in a higher liquid tar yield as shown in Table 1-9. The no-water case allows for a close comparison to the classical fluidized bed (CFB) simulation performed by Xue et al. [31]. Their simulations and those performed in the work of Ashcraft et al. utilized the same biomass composition, biomass-to-nitrogen mass feed ratio, inlet gas temperature, reaction mechanism and kinetics, and a similar Eulerian-Eulerian framework. The simulation of the CFB reactor resulted in a product distribution of 14.4 wt% char, 63.4 wt% tar, 21.5 wt% pyrolysis gas and 0.7 wt% unreacted biomass. This corresponds to a significantly lower tar yield than the GSVR simulations. The no-water simulations yielded 76 wt% tar compared to 63.4 wt% for the simulations performed in the CFB reactor.

One of the main benefits of the GSVR is its potential to intensify processes via increased volumetric production rates. The much higher gas flow rate per reactor volume allows for proportionally higher biomass feed rate, resulting in a higher volumetric production rate for a fixed ratio of biomass to gas flow rate. Two simulations were performed with increased biomass and inlet gas feed rates, the 1.5x flow case and the 2x flow case. The increased flow rates allowed a stable simulation with a proportional increase in the volumetric production rate with a product distribution that is almost not affected by the increased production rate as shown in Table 1-9.

In fast biomass pyrolysis sand is typically used as a heat carrier. The presence of sand improves the breakup of the biomass particles and increases the heat transfer rate. In a GSVR setup sand is not necessary since there is already a high convective heat transfer from the gas. Performing GSVR experiments without sand may provide unique process simplifications. These simulations result in significantly different results compared to the cases involving sand as the unreacted biomass and char volume fractions in the reactor are much larger. Unreacted biomass occupies the outermost radial reactor locations since biomass is the most dense component in the reactor. Simulations also yielded a more oscillatory behavior of the char fraction in the vortex reactor.

Table 1-9: Product distribution results for all simulation cases as a percentage of fed dry biomass [86].

	Char (wt%)	Tar (wt%)	Pyrolysis gas (wt%)
Base	16.1	73.8	9.5
973 K	14.6	75.6	8.9
No-water	14.5	76.0	8.9
1.5x flow	16.3	73.8	9.2
2x flow	16.8	73.3	9.1
No-sand	17.1	73.6	9.3
No-sand/No-water	16.0	75.6	8.7

The high heat transfer coefficients inside the GSVR bed make the GSVR not only suitable for biomass conversion by fast pyrolysis. Numerical parametric evaluation of low temperature pyrolysis and gasification of biomass for process intensification has been studied intensively [89]. Biomass gasification produces syngas that can be converted via the Fischer-Tropsch synthesis to diesel fuel, low in sulfur content and with a desirable low cetane number. Primary pyrolysis, char combustion and gasification reactions are accounted for. The simulations are carried out feeding 650 μm biomass particles. The moisture content of the biomass fed is defined in wt% on a dry basis and fixed to 10 wt% in all simulations. The biomass is fed at room temperature (300 K), whereas the air fed is preheated to 600 K. Rotating fluidized beds in a static geometry offer extremely high specific biomass conversion rates, even when operating at lower temperatures. Specific biomass conversion rates easily two orders of magnitude higher than typical in circulating fluidized bed risers can be achieved. This opens perspectives for optimizing the liquids production and operation at temperatures below the ash melting temperature.

1.5. Conclusion

The literature study started giving the reader an introduction to sustainable biomass conversion processes. The focus of the rest of the literature study was on fast biomass pyrolysis since it is the most energy efficient biomass conversion process. The biomass components and the possible fast biomass pyrolysis reaction mechanisms were discussed.

A review on gravitational fluidized bed reactors has been provided as this classical reactor is the most extensively researched reactor type for fast biomass pyrolysis processes. An experimental setup was described before going into more detail on various publications on the topic. However there is still no “best available technology” with most established processes giving liquid tar yields between 67 -75 % based on dry biomass input.

Other fluidized bed reactors have been briefly discussed; and finally literature on the gas solid vortex reactor has been reviewed. The high gas-solid slip velocities inside this fluidized bed result in high convective heat transfer coefficients and very short gas-phase residence times, which are promising for fast biomass pyrolysis processes. First the experimental setup was discussed before going into more detail on the CFD models that will be used for the fast biomass pyrolysis simulations.

1.6. Bibliography

1. Suopajärvi, H., E. Pongrácz, and T. Fabritius, *The potential of using biomass-based reducing agents in the blast furnace: A review of thermochemical conversion technologies and assessments related to sustainability.* Renewable and Sustainable Energy Reviews, 2013. **25**: p. 511-528.
2. Aramideh, S., *Numerical simulation of biomass fast pyrolysis in fluidized bed and auger reactors*. 2014, Iowa State University: Iowa. p. 107.
3. Reijnders, L., *Conditions for the sustainability of biomass based fuel use.* Energy policy, 2006. **34**(7): p. 863-876.
4. Türe, S., D. Uzun, and I.E. Türe, *The potential use of sweet sorghum as a non-polluting source of energy.* Energy, 1997. **22**(1): p. 17-19.
5. Sheehan, J., et al., *An overview of biodiesel and petroleum diesel life cycles*. 2000, National Renewable Energy Lab., Golden, CO (US).
6. Mohan, D., C.U. Pittman, and P.H. Steele, *Pyrolysis of wood/biomass for bio-oil: A critical review.* Energy & Fuels, 2006. **20**(3): p. 848-889.
7. Tribe, M.A., M. Eraut, and R.K. Snook, *Photosynthesis*. 1975: Cambridge University Press.
8. Puhan, S., et al., *Mahua (Madhuca indica) seed oil: A source of renewable energy in India.* Journal of Scientific and Industrial Research, 2005. **64**(11): p. 890.
9. Demirbas, A., *Progress and recent trends in biofuels.* Progress in Energy and Combustion Science, 2007. **33**(1): p. 1-18.
10. Hallenbeck, P.C. and J.R. Benemann, *Biological hydrogen production; fundamentals and limiting processes.* International Journal of Hydrogen Energy, 2002. **27**(11-12): p. 1185-1193.
11. Chen, X.W., et al., *A highly efficient dilute alkali deacetylation and mechanical (disc) refining process for the conversion of renewable biomass to lower cost sugars.* Biotechnology for Biofuels, 2014. **7**: p. 11.
12. Czernik, S. and A.V. Bridgwater, *Overview of applications of biomass fast pyrolysis oil.* Energy & Fuels, 2004. **18**(2): p. 590-598.
13. Bridgwater, A.V. and G.V.C. Peacocke, *Fast pyrolysis processes for biomass.* Renewable & Sustainable Energy Reviews, 2000. **4**(1): p. 1-73.
14. Kaushal, P. and J. Abedi, *A simplified model for biomass pyrolysis in a fluidized bed reactor.* Journal of Industrial and Engineering Chemistry, 2010. **16**(5): p. 748-755.
15. Antal, M.J. and M. Gronli, *The art, science, and technology of charcoal production.* Industrial & Engineering Chemistry Research, 2003. **42**(8): p. 1619-1640.
16. Bridgwater, A.V., A.J. Toft, and J.G. Brammer, *A techno-economic comparison of power production by biomass fast pyrolysis with gasification and combustion.* Renewable & Sustainable Energy Reviews, 2002. **6**(3): p. 181-248.
17. Bridgwater, A.V., *Review of fast pyrolysis of biomass and product upgrading.* Biomass & Bioenergy, 2012. **38**: p. 68-94.
18. Klass, D.L., *Biomass for Renewable Energy, Fuels, and Chemicals*. 1998: Elsevier Science.
19. Tumuluru, J.S., et al. *A review on biomass classification and composition, co-firing issues and pretreatment methods*. in *Proceedings of the American Society of Agricultural and Biological Engineers Annual International Meeting*. 2011. Citeseer.

20. Roger C, P., *The Chemical Composition of Wood*, in *The Chemistry of Solid Wood*. 1984, American Chemical Society. p. 57-126.

21. Wertz, J.L., O. Bédué, and J.P. Mercier, *Cellulose Science and Technology*. 2010: EFPL Press.

22. Shen, D.K. and S. Gu, *The mechanism for thermal decomposition of cellulose and its main products.* Bioresource Technology, 2009. **100**(24): p. 6496-6504.

23. Resende, F.L.P. and P.E. Savage, *Kinetic model for noncatalytic supercritical water gasification of cellulose and lignin.* AIChE Journal, 2010. **56**(9): p. 2412-2420.

24. Goldstein, I.S., *Organic chemicals from biomass.* Organic chemicals from biomass., 1981.

25. Heitner, C., D. Dimmel, and J. Schmidt, *Lignin and Lignans: Advances in Chemistry*. 2011: CRC Press.

26. Huber, G.W. and A. Corma, *Synergies between bio- and oil refineries for the production of fuels from biomass.* Angewandte Chemie-International Edition, 2007. **46**(38): p. 7184-7201.

27. Neogi, D., et al., *Study of coal gasification in an experimental fluidized bed reactor.* AIChE Journal, 1986. **32**(1): p. 17-28.

28. Scott, D.S., et al., *A second look at fast pyrolysis of biomass - the RTI process.* Journal of Analytical and Applied Pyrolysis, 1999. **51**(1-2): p. 23-37.

29. Hamelinck, C.N. and A.P.C. Faaij, *Outlook for advanced biofuels.* Energy Policy, 2006. **34**(17): p. 3268-3283.

30. Xue, Q., et al., *Experimental validation and CFD modeling study of biomass fast pyrolysis in fluidized-bed reactors.* Fuel, 2012. **97**: p. 757-769.

31. Xue, Q., T.J. Heindel, and R. Fox, *A CFD model for biomass fast pyrolysis in fluidized-bed reactors.* Chemical Engineering Science, 2011. **66**(11): p. 2440-2452.

32. Xiong, Q.G., S. Aramideh, and S.C. Kong, *Assessment of Devolatilization Schemes in Predicting Product Yields of Biomass Fast Pyrolysis.* Environmental Progress & Sustainable Energy, 2014. **33**(3): p. 756-761.

33. Van de Velden, M., et al., *Fundamentals, kinetics and endothermicity of the biomass pyrolysis reaction.* Renewable Energy, 2010. **35**(1): p. 232-242.

34. Boateng, A.A. and P.L. Mtui, *CFD modeling of space-time evolution of fast pyrolysis products in a bench-scale fluidized-bed reactor.* Applied Thermal Engineering, 2012. **33-34**: p. 190-198.

35. Yu, X., et al., *A CFD study of biomass pyrolysis in a downer reactor equipped with a novel gas-solid separator - I: Hydrodynamic performance.* Fuel Processing Technology, 2014. **126**: p. 366-382.

36. Chan, W.C.R., M. Kelbon, and B.B. Krieger, *MODELING AND EXPERIMENTAL-VERIFICATION OF PHYSICAL AND CHEMICAL PROCESSES DURING PYROLYSIS OF A LARGE BIOMASS PARTICLE.* Fuel, 1985. **64**(11): p. 1505-1513.

37. Xue, Q. and R.O. Fox, *Multi-fluid CFD modeling of biomass gasification in polydisperse fluidized-bed gasifiers.* Powder Technology, 2014. **254**: p. 187-198.

38. Xue, Q.L. and R.O. Fox, *Computational Modeling of Biomass Thermochemical Conversion in Fluidized Beds: Particle Density Variation and Size Distribution.* Industrial & Engineering Chemistry Research, 2015. **54**(16): p. 4084-4094.

39. Xiong, Q.G., S. Aramideh, and S.C. Kong, *Modeling Effects of Operating Conditions on Biomass Fast Pyrolysis in Bubbling Fluidized Bed Reactors.* Energy & Fuels, 2013. **27**(10): p. 5948-5956.

40. Xiong, Q.G., et al., *BIOTC: An open-source CFD code for simulating biomass fast pyrolysis.* Computer Physics Communications, 2014. **185**(6): p. 1739-1746.

41. Xiong, Q.G., S.C. Kong, and A. Passalacqua, *Development of a generalized numerical framework for simulating biomass fast pyrolysis in fluidized-bed reactors.* Chemical Engineering Science, 2013. **99**: p. 305-313.

42. Papadikis, K., A.V. Bridgwater, and S. Gu, *CFD modelling of the fast pyrolysis of biomass in fluidised bed reactors, Part A: Eulerian computation of momentum transport in bubbling fluidised beds.* Chemical Engineering Science, 2008. **63**(16): p. 4218-4227.

43. Papadikis, K., S. Gu, and A.V. Bridgwater, *CFD modelling of the fast pyrolysis of biomass in fluidised bed reactors. Part B Heat, momentum and mass transport in bubbling fluidised beds.* Chemical Engineering Science, 2009. **64**(5): p. 1036-1045.

44. Papadikis, K., S. Gu, and A.V. Bridgwater, *CFD modelling of the fast pyrolysis of biomass in fluidised bed reactors: Modelling the impact of biomass shrinkage.* Chemical Engineering Journal, 2009. **149**(1-3): p. 417-427.

45. Papadikis, K., S. Gu, and A.V. Bridgwater, *Computational modelling of the impact of particle size to the heat transfer coefficient between biomass particles and a fluidised bed.* Fuel Processing Technology, 2010. **91**(1): p. 68-79.

46. Papadikis, K., et al., *Application of CFD to model fast pyrolysis of biomass.* Fuel Processing Technology, 2009. **90**(4): p. 504-512.

47. Xiong, Q., et al., *Modeling the impact of bubbling bed hydrodynamics on tar yield and its fluctuations during biomass fast pyrolysis.* Fuel, 2016. **164**: p. 11-17.

48. Mellin, P., et al., *An Euler-Euler approach to modeling biomass fast pyrolysis in fluidized-bed reactors - Focusing on the gas phase.* Applied Thermal Engineering, 2013. **58**(1-2): p. 344-353.

49. Mellin, P., E. Kantarelis, and W.H. Yang, *Computational fluid dynamics modeling of biomass fast pyrolysis in a fluidized bed reactor, using a comprehensive chemistry scheme.* Fuel, 2014. **117**: p. 704-715.

50. Ranzi, E., et al., *Chemical Kinetics of Biomass Pyrolysis.* Energy & Fuels, 2008. **22**(6): p. 4292-4300.

51. Bradbury, A.G.W., Y. Sakai, and F. Shafizadeh, *A kinetic model for pyrolysis of cellulose.* Journal of Applied Polymer Science, 1979. **23**(11): p. 3271-3280.

52. Miller, R. and J. Bellan, *A generalized biomass pyrolysis model based on superimposed cellulose, hemicelluloseand liqnin kinetics.* Combustion science and technology, 1997. **126**(1-6): p. 97-137.

53. Liden, A., F. Berruti, and D. Scott, *A kinetic model for the production of liquids from the flash pyrolysis of biomass.* Chemical Engineering Communications, 1988. **65**(1): p. 207-221.

54. Bradbury, A.G., Y. Sakai, and F. Shafizadeh, *A kinetic model for pyrolysis of cellulose.* Journal of Applied Polymer Science, 1979. **23**(11): p. 3271-3280.

55. Miller, R.S. and J. Bellan, *Numerical simulation of vortex pyrolysis reactors for condensable tar production from biomass.* Energy & Fuels, 1998. **12**(1): p. 25-40.

56. Gidaspow, D., R. Bezburuah, and J. Ding, *Hydrodynamics of circulating fluidized beds: Kinetic theory approach*. 1991. Medium: ED; Size: Pages: (8 p).

57. Syamlal, M., *The particle-particle drag term in a multiparticle model of fluidization*, in *Other Information: Portions of this document are illegible in microfiche products. Original copy available until stock is exhausted*. 1987. p. Medium: X; Size: Pages: 25.

58. Gunn, D.J., *Transfer of heat or mass to particles in fixed and fluidised beds.* International Journal of Heat and Mass Transfer, 1978. **21**(4): p. 467-476.

59. Xiong, Q.G. and S.C. Kong, *Modeling effects of interphase transport coefficients on biomass pyrolysis in fluidized beds.* Powder Technology, 2014. **262**: p. 96-105.

60. Wang, J., W. Ge, and J. Li, *Eulerian simulation of heterogeneous gas–solid flows in CFB risers: EMMS-based sub-grid scale model with a revised cluster description.* Chemical Engineering Science, 2008. **63**(6): p. 1553-1571.

61. Mellin, P., et al., *Simulation of Bed Dynamics and Primary Products from Fast Pyrolysis of Biomass: Steam Compared to Nitrogen as a Fluidizing Agent.* Industrial & Engineering Chemistry Research, 2014. **53**(30): p. 12129-12142.

62. Meier, D. and O. Faix, *State of the art of applied fast pyrolysis of lignocellulosic materials — a review.* Bioresource Technology, 1999. **68**(1): p. 71-77.

63. Diebold, J. and A. Bridgwater, *Overview of fast pyrolysis of biomass for the production of liquid fuels*, in *Developments in thermochemical biomass conversion*. 1997, Springer. p. 5-23.

64. Bridgwater, A. and G. Peacocke. *Engineering developments in fast pyrolysis for bio-oils*. in *Proceedings Biomass Pyrolysis Oil Properties and Combustion Meeting. NREL*. 1994.

65. Choi, H.S., Y.S. Choi, and S.J. Kim, *Numerical Study of Fast Pyrolysis of Woody Biomass in a Gravity-Driven Reactor.* Environmental Progress & Sustainable Energy, 2009. **28**(3): p. 418-426.

66. Yu, X., et al., *A CFD study of biomass pyrolysis in a downer reactor equipped with a novel gas-solid separator-II thermochemical performance and products.* Fuel Processing Technology, 2015. **133**: p. 51-63.

67. Aramideh, S., et al., *Numerical simulation of biomass fast pyrolysis in an auger reactor.* Fuel, 2015. **156**: p. 234-242.

68. Pantzali, M.N., et al., *Radial pressure profiles in a cold-flow gas-solid vortex reactor.* Aiche Journal, 2015. **61**(12): p. 4114-4125.

69. Anderson, L.A., S.H. Hasinger, and B. Turman, *Two-component vortex flow studies of the colloid core nuclear rocket.* Journal of Spacecraft and Rockets, 1972. **9**(5): p. 311-317.

70. DICKSON, P., et al., *An engineering study of the colloid-fueled reactor concept(Ground test reactor design based on colloid fueled reactor concept).* JOURNAL OF SPACECRAFT AND ROCKETS, 1970. **8**: p. 129-133.

71. Kochetov, L., B. Sazhin, and E. Karlik, *Experimental determination of the optimal ratios of structural dimensions in the whirl chamber for drying granular materials.* Chemical and Petroleum Engineering, 1969. **5**(2): p. 106-108.

72. Volchkov, E., et al., *Aerodynamics and heat and mass transfer of fluidized particle beds in vortex chambers.* Heat transfer engineering, 1993. **14**(3): p. 36-47.

73. Kuzmin, A., et al., *Vortex centrifugal bubbling reactor.* Chemical Engineering Journal, 2005. **107**(1): p. 55-62.

74. Loftus, P.J., D.B. Stickler, and R.C. Diehl, *A confined vortex scrubber for fine particulate removal from flue gases.* Environmental progress, 1992. **11**(1): p. 27-32.

75. Ryazantsev, A., et al., *Liquid-phase oxidation of hydrogen sulfide in centrifugal bubbling apparatus.* Russian Journal of Applied Chemistry, 2007. **80**(9): p. 1544-1548.

76. Ashcraft, R.W., et al., *Assessment of a Gas-Solid Vortex Reactor for SO2/NOx Adsorption from Flue Gas.* Industrial & Engineering Chemistry Research, 2013. **52**(2): p. 861-875.

77. Trujillo, W.R. and J. De Wilde, *Fluid catalytic cracking in a rotating fluidized bed in a static geometry: a CFD analysis accounting for the distribution of the catalyst coke content.* Powder Technology, 2012. **221**: p. 36-46.

78. De Wilde, J., *Gas–solid fluidized beds in vortex chambers.* Chemical Engineering and Processing: Process Intensification, 2014. **85**: p. 256-290.

79. de Broqueville, A. and J. De Wilde, *Numerical investigation of gas-solid heat transfer in rotating fluidized beds in a static geometry.* Chemical Engineering Science, 2009. **64**(6): p. 1232-1248.

80. De Wilde, J. and A. de Broqueville, *Rotating fluidized beds in a static geometry: experimental proof of concept.* AIChE journal, 2007. **53**(4): p. 793-810.

81. Ekatpure, R.P., et al., *Experimental investigation of a gas–solid rotating bed reactor with static geometry.* Chemical Engineering and Processing: Process Intensification, 2011. **50**(1): p. 77-84.

82. Kovacevic, J.Z., et al., *Bed stability and maximum solids capacity in a Gas-Solid Vortex Reactor: Experimental study.* Chemical Engineering Science, 2014. **106**: p. 293-303.

83. Qian, G.H., et al., *Gas-solid fluidization in a centrifugal field.* Aiche Journal, 2001. **47**(5): p. 1022-1034.

84. Watano, S., et al., *Microgranulation of fine powders by a novel rotating fluidized bed granulator.* Powder Technology, 2003. **131**(2-3): p. 250-255.

85. Quevedo, J., et al., *Fluidization of nanoagglomerates in a rotating fluidized bed.* Aiche Journal, 2006. **52**(7): p. 2401-2412.

86. Ashcraft, R.W., G.J. Heynderickx, and G.B. Marin, *Modeling fast biomass pyrolysis in a gas-solid vortex reactor.* Chemical Engineering Journal, 2012. **207**: p. 195-208.

87. Shafizadeh, F., *INTRODUCTION TO PYROLYSIS OF BIOMASS.* Journal of Analytical and Applied Pyrolysis, 1982. **3**(4): p. 283-305.

88. Dutta, A., et al., *Rotating fluidized bed with a static geometry: Guidelines for design and operating conditions.* Chemical Engineering Science, 2010. **65**(5): p. 1678-1693.

89. Staudt, N., et al., *Low-temperature pyrolysis and gasification of biomass: numerical evaluation of the process intensification potential of rotating-and circulating rotating fluidized beds in a static fluidization chamber.* International Journal of Chemical Reactor Engineering, 2011. **9**(1).

Chapter 2: Geometric Study of a Gas Solid Vortex Reactor

Table of Contents

List of Figures

List of Tables

2.1. Introduction GSVR geometry

In this study the influence of geometric parameters of a gas-solid vortex reactor (GSVR) on two phase hydrodynamics will be investigated. Cold flow simulations will be performed on various reactor geometries to investigate both the influence of injection slot angle and the injection slot thickness on process operating conditions, especially the local heat transfer coefficient and the radial and azimuthal velocities at various positions in the reactor. For this study nine 2-D reactor geometries have been generated with an injection slot angle varying from 10° to 20° and a varying injection slot thickness ranging from 1.0 mm to 2.0 mm. The geometric reactor parameters are given in Table 2-1:

Table 2-1: Independent geometric parameters of the GSVR.

Variable		
Distributor jacket diameter	D_J	0.68 m
Reactor diameter	D_R	0.54 m
Exhaust diameter	D_E	0.2 m
Reactor length	L_R	0.1 m
Number of injection slots	I_N	36
Injection slot thickness	I_O	1.0 mm-1.5 mm-2.0 mm
Injection slot angle	ϑ	10°-15°-20°

The goal of this study is to investigate the difference in heat transfer coefficient when comparing the more strict geometric specifications, 1.0 mm injection slot thickness and 10° injection slot angle, to an easier to construct geometry, 2.0 mm injection slot thickness and 20° injection slot angle. This will be done by analyzing the different azimuthal and radial velocity profiles in the different reactor geometries for a constant mass flow rate of gas.

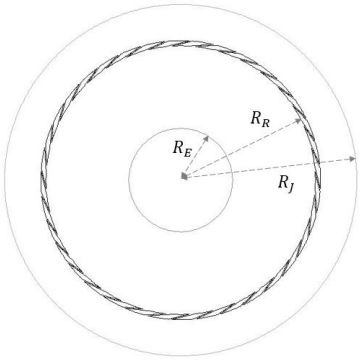

Figure 2-1: Visual representation of a gas-solid vortex reactor with the specified geometry.

2.2. Numerical methods

The finite-volume based CFD software Fluent, is used to numerically study the flow of a viscous incompressible gas in the gas-solid vortex reactor. 2-D simulations of a cross section of the reactor are performed for the 360° geometry. The highly turbulent flow inside the GSVR requires proper numerical turbulence modeling. The Reynolds Averaged Navier-Stokes (RANS) turbulence modeling approach is adopted, as the main goal of the present study is to investigate the hydrodynamics inside the GSVR. The Reynold Stress Model (RSM) is used to model the GSVR turbulence by resolving the Reynolds stresses and thus capturing the anisotropic nature of the Reynolds stresses owing to the curved nature of the reactor. The governing conservation equations and turbulence model equations are presented in Table 2-2.

Table 2-2: Conservation equations and turbulence models applied in the numerical simulations.

Mass Conservation:

$$\frac{\partial}{\partial t}\left(\varepsilon_i \rho_i\right)+\nabla\cdot\left(\varepsilon_i \rho_i \overline{U_i}\right)=0 \quad \text{with (i = g, s)} \tag{2.1}$$

Momentum Conservation:

Gas:

$$\frac{\partial}{\partial t}\left(\varepsilon_g \rho_g \overline{U_g}\right)+\nabla\cdot\left(\varepsilon_g \rho_g \overline{U_g}\,\overline{U_g}\right)=-\varepsilon_g \nabla P+\nabla\cdot\overline{\overline{\tau_g}}+\varepsilon_g \rho_g \bar{g}-\beta\left(\overline{U_g}-\overline{U_s}\right) \tag{2.2}$$

Solids:

$$\frac{\partial}{\partial t}\left(\varepsilon_s \rho_s \overline{U_s}\right)+\nabla\cdot\left(\varepsilon_s \rho_s \overline{U_s}\,\overline{U_s}\right)=-\varepsilon_s \nabla P-\nabla P_s+\nabla\cdot\overline{\overline{\tau_s}}+\varepsilon_s \rho_s \bar{g}-\beta\left(\overline{U_s}-\overline{U_g}\right) \tag{2.3}$$

Transport equation for k, turbulent kinetic energy:

$$\frac{\partial}{\partial t}\left(\varepsilon_i \rho_i k\right)+\nabla\cdot\left(\varepsilon_i \rho_i k \overline{U_i}\right)=\nabla\cdot\left(\varepsilon_i \frac{\mu_{t,i}}{\sigma_j}\nabla k\right)+\left(\varepsilon_i \mu_{t,i}\left(\nabla\overline{U_i}+\overline{U_i}^{T}\right):\nabla\overline{U_i}-\varepsilon_i \rho_i e\right)-\beta\left(2k\right) \quad \text{with (i = g, s)} \tag{2.4}$$

Transport equation for e, dissipation rate of turbulent kinetic energy:

$$\frac{\partial}{\partial t}\left(\varepsilon_i \rho_i e\right)+\nabla\cdot\left(\varepsilon_i \rho_i e \overline{U_i}\right)=\nabla\cdot\left(\varepsilon_i \frac{\mu_{t,i}}{\sigma_j}\nabla e\right)+C_{1s}\frac{e}{k}\left(\varepsilon_i \mu_{t,i}\left(\nabla\overline{U_i}+\overline{U_i}^{T}\right):\nabla\overline{U_i}\right)-C_{2s}\varepsilon_i \rho_i \frac{e^2}{k}-\beta\left(2k\right)C_{3s}\frac{e}{k} \tag{2.5}$$

with (i = g, s)

The turbulent viscosity $\mu_{t,i}$ in equations (2.4-2.5) can then be computed from:

$$\mu_{t,i}=\rho_i C_\mu \frac{k^2}{e} \qquad \text{with (i = g, s)} \tag{2.6}$$

The governing equations are spatially discretized using third order Monotone Upstream-Centered Schemes for Conservation laws (MUSCL). Pressure corrections are computed using the body force weighted Pressure Staggering Option (PRESTO!) scheme. A segregated solver is used for the pressure-velocity coupling following the Semi-Implicit Method for Pressure-Linked Equations (Simple) algorithm. A second order implicit time stepping scheme is used. The time step size during the transient simulations is 10^{-3} s with 40 iterations per time step. The physical properties of the gas phase and the gas-solid interactions are given in Table 2-3.

Table 2-3: The physical properties of the gas phase and the gas-solid interactions.

Gas phase stress tensor:

$$\overline{\overline{\tau_g}} = \varepsilon_g \left(\mu_g + \mu_{t,g}\right)\left(\nabla\overline{U_g} + \nabla\overline{U_g}^T\right) \tag{2.7}$$

Granular Temperature: [1]

$$\left(-P_s\overline{\overline{I}} + \overline{\overline{\tau_s}}\right) : \nabla\overline{U_s} - \gamma\Theta_s + 3\beta\Theta_s = 0 \tag{2.8}$$

Solids pressure: [2]

$$P_s = \rho_p\varepsilon_s\theta + 2(1+e_{ss})\rho_p\theta g_{0,ss}\left(\varepsilon_s\right)\varepsilon_s{}^2 \tag{2.9}$$

Gas-solid drag coefficient: [3]

$$\beta = \frac{3}{4}C_D\frac{\varepsilon_g\varepsilon_s\rho_g\left|\overline{U_{slip}}\right|}{d_p}\varepsilon_g{}^{-2.65} \quad (\text{for } \varepsilon_g > 0.8)$$

$$\text{where } C_D = 150\frac{24}{\varepsilon_g\,\mathrm{Re}_s}\left[1+0.15\left(\varepsilon_g\,\mathrm{Re}_s\right)^{0.687}\right];\quad \mathrm{Re}_s = \frac{\rho_g d_p\left|\overline{U_{slip}}\right|}{\mu_g} \tag{2.10}$$

$$\beta = 150\frac{\varepsilon_s^2\mu_g}{\varepsilon_g d_p^2} + 1.75\frac{\rho_g\varepsilon_s\left|\overline{U_{slip}}\right|}{d_p} \quad (\text{for } \varepsilon_g \le 0.8)$$

Radial distribution function: [4]

$$g_{0,ss} = \left[1-\left(\frac{\varepsilon_s}{\varepsilon_{s,\max}}\right)^{\frac{1}{3}}\right]^{-1} \tag{2.11}$$

Solid-phase shear stress tensor:

$$\overline{\overline{\tau_s}} = \varepsilon_s \mu_s \left(\nabla \overline{U_s} + \nabla \overline{U_s}^T \right) + \varepsilon_s \left(\lambda_s - \frac{2}{3} \left(\mu_{s,col} + \mu_{s,kin} + \mu_{s,fr} + \mu_{t,s} \right) \right) \nabla \cdot \overline{U_s} \overline{\overline{I}} \tag{2.12}$$

Solids collision viscosity: [3]

$$\mu_{s,col} = \frac{4}{5} \varepsilon_s \rho_s d_p g_{0,ss} (1 + e_{ss}) \left(\frac{\Theta_s}{\pi} \right)^{1/2} \tag{2.13}$$

Solids kinetic viscosity: [5]

$$\mu_{s,kin} = \frac{\varepsilon_s \rho_s d_p \sqrt{\Theta_s \pi}}{6(3 - e_{ss})} \left[1 + \frac{2}{5} \varepsilon_s g_{0,ss} (1 + e_{ss})(3e_{ss} - 1) \right] \tag{2.14}$$

Solids frictional viscosity: [6]

$$\mu_{s,fr} = \frac{P_s \sin\delta}{2\sqrt{I}} \tag{2.15}$$

Solids bulk viscosity: [2]

$$\lambda_s = \frac{4}{3} \varepsilon_s \rho_s d_p g_{0,ss} (1 + e_{ss}) \left(\frac{\Theta_s}{\pi} \right)^{1/2} \tag{2.16}$$

2.3. Mesh study

The first step in generating the required reactor geometries is defining an appropriate mesh. In order to select the appropriate meshing conditions for all geometries a mesh dependency study will be performed on one specific geometry, in this case the 1.0 mm injection slot thickness and 10° injection slot angle geometry. Four meshes were generated with an increasing number of cells as shown in Table 2-4:

Table 2-4: Four of the generated meshes for the 1.0 mm injection slot and 10° injection angle GSVR geometry with the corresponding number of cells.

Mesh name	Number of cells
(a) Extra Coarse mesh	43,631
(b) Coarse mesh	77,397
(c) Medium mesh	119,406
(d) Fine mesh	136,473

In previous simulations it was noted that meshes with a number of cells below 75,000 gave mesh dependent results. Two simulations are assumed to be mesh independent if for a different number of computational cells the output is similar after the same simulation time, in this case at steady-state after 2.0 s. The simulations were performed with the CFD software package ANSYS Fluent, using a 2-D model. The reactor is modeled using an unsteady, time-varying solver to capture the dynamics of the bed. The gas phase momentum was calculated using the realizable k-ε model and had a jacket injection velocity of 1.433 m/s, which corresponds to a volumetric flow rate of 1102 Nm^3/h.

In Figure 2-2 the azimuthal velocity of air is shown in function of radial distance, the velocity profiles for the fine and medium mesh are similar, implicating that the simulation is mesh independent for a number of cells larger than the number of cells in the medium mesh (c), around 120,000. The extra coarse and coarse mesh were added in Figure 2-2 to visually represent the mesh dependency for simulations with a shortage of computational cells. The azimuthal velocities have been calculated for a GSVR geometry with 24 injection slots and not the default 36 injection slots, resulting in higher azimuthal velocities, as can be intuitively expected since the total injection area is reduced with a factor 1/3 while keeping the volumetric air feeding rate constant.

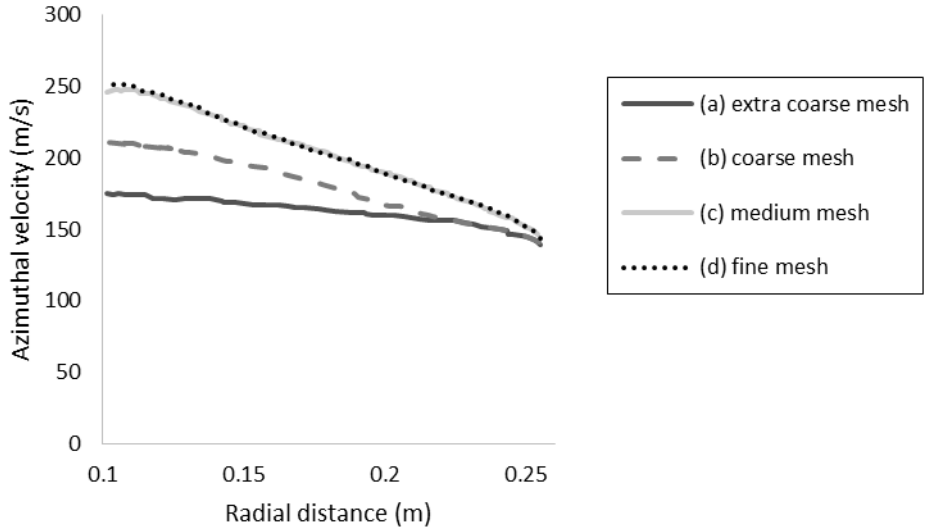

Figure 2-2: Azimuthal velocity in function of radial distance for various meshes of the same GSVR geometry after 2.0 s of gas feeding at steady-state.

The meshes for the other GSVR geometries were generated with the same conditions as the medium mesh case of the 1.0 mm injection slot thickness and 10° injection slot angle. The advantage of the medium mesh over the fine mesh is that a reduction in the number of cells significantly lowers the computational effort of the simulations. The injection slot angle is varied from 10° to 20° as shown in Figure 2-3. The variation in injection slot thickness is shown in Figure 2-4.

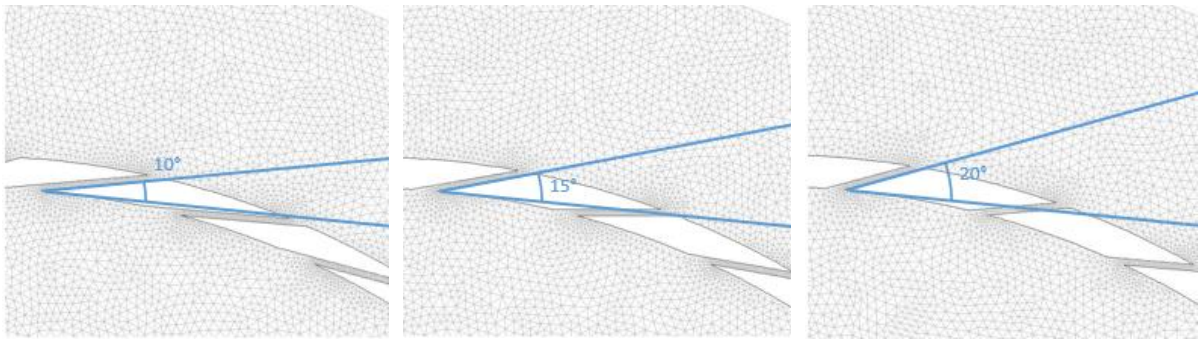

Figure 2-3: Meshes for geometries with injection slot angles varying from 10° to 20°.

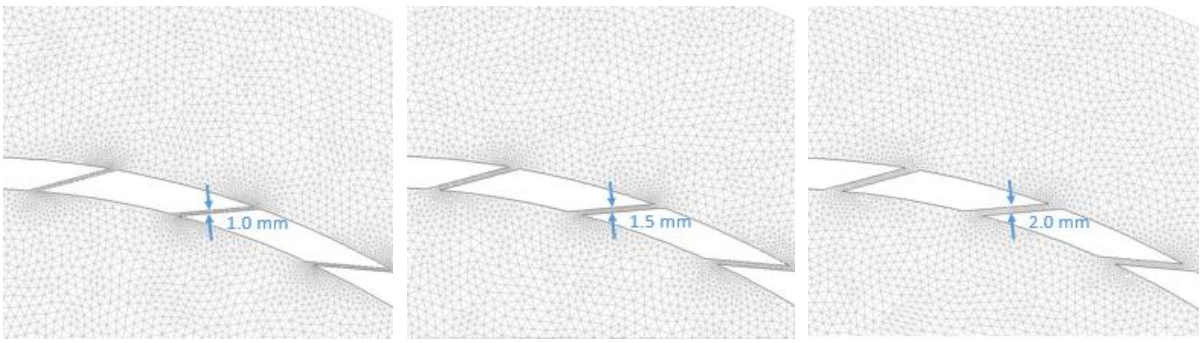

Figure 2-4: Meshes for injection slot thickness varying from 1.0 mm to 2.0 mm.

2.4. Gas only flow

Now that the nine GSVR meshes are available, the first simulations will be performed with only air entering the reactor at 1.433 m/s. In a next step polymer particles will be added in order to investigate the gas-solid interactions. Intuitively it is to be expected that reducing the slot thickness or reducing the injection slot angle will result in a higher azimuthal velocity.

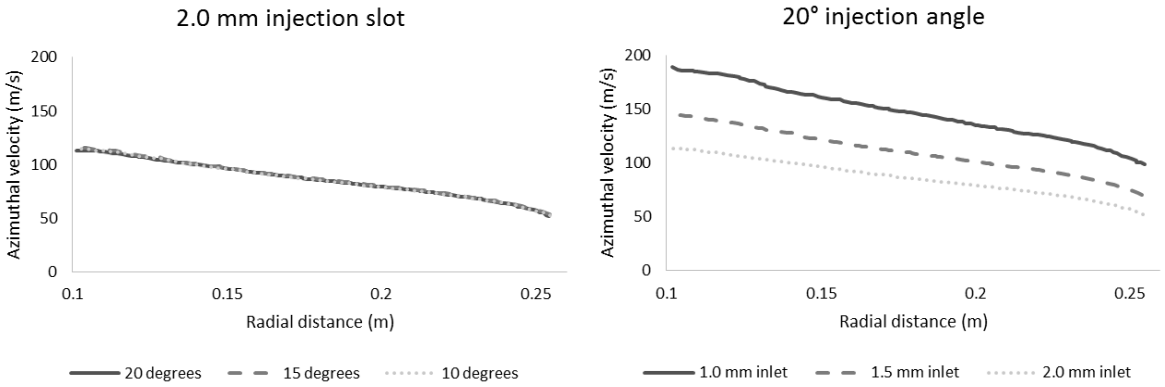

Figure 2-5: Azimuthal velocity in function of radial distance at steady-state for a constant injection slot thickness and varying injection slot angle (left) and for a constant injection slot angle with varying injection slot thickness (right).

Figure 2-5 shows that the azimuthal velocity increases significantly with decreasing slot thickness. The azimuthal velocity appears to be independent of the injection slot angle for gas only simulations.

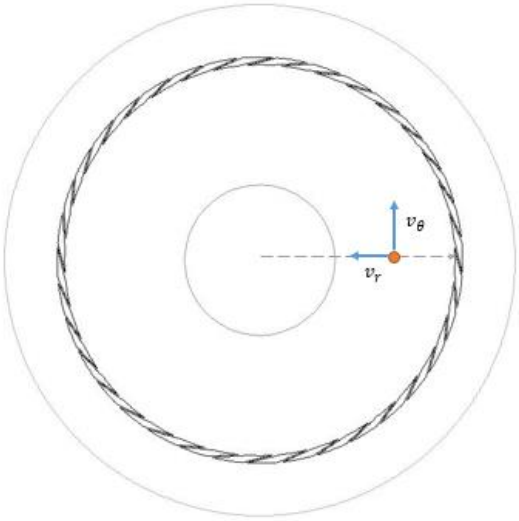

Figure 2-6: Visual representation of the azimuthal (also called tangential) and radial velocity (also known as axial velocity) vectors in a rotating GSVR.

However not only the azimuthal velocity of the gaseous phase is of importance. The ratio between the azimuthal, v_θ, and radial velocity, v_r, is called the swirl ratio and is indicative of the local ratio of angular momentum to radial momentum in a vortex [7, 8].

$$Swirl\ ratio = \left|\frac{v_\theta}{v_r}\right| \tag{2.17}$$

Figure 2-7 shows that the absolute value of the local swirl ratio increases with decreasing slot thickness. However this trend is less pronounced comparing the 2.0 mm inlet to the 1.5 mm inlet for a constant injection slot angle in Figure 2-5 looking only at the azimuthal velocity. This suggests that the radial velocity is increasing proportional to the azimuthal velocity for larger injection slots.

The injection angle appears to have no influence on the swirl ratio of the gas for a constant injection slot thickness. The swirl ratio is positive in Figure 2-7 despite the radial velocity being negative compared to the x-axis as shown in Figure 2-6, however only the absolute value of the swirl ratio is indicative for the magnitude.

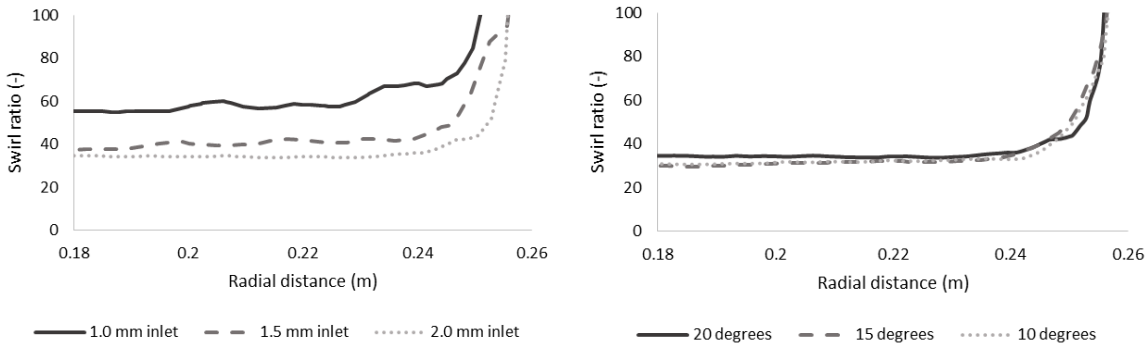

Figure 2-7: Swirl ratio in function of radial distance at steady-state for a constant injection slot thickness and varying injection slot angle (right) and for a constant injection slot angle with varying injection slot thickness (left).

It might be possible that the jacket gas flow rate is too high resulting in highly turbulent flow after the injection slot, so that the entrainment of the "jet" after the slots can no longer be distinguished for the different injection slot angles. Lower gas inlet velocities might result in different swirl ratios for different injection slot angles. These high velocity profiles in the reactor are necessary in case a second solid phase is added. Momentum will be transferred to the solid phase to generate a rotating bed, resulting in lower gas phase velocities.

2.5. Two phase flow

In a next step two-phase simulations will be performed with both polymer particles and air in the reactor. The Eulerian granular solids formulation was employed to model the particle behavior, using the per phase realizable k-ε model for turbulence. The Gidaspow model was used to model the fluid-solid drag interactions since the Gidaspow model is recommended for dense fluidized beds. [5] Turbulence interaction was accounted for using the Simonin-et-al model.[9] For the wall conditions of air the no-slip boundary condition was selected. Since the no-slip boundary condition is typically applied for fluids, the wall boundary condition for the polymer phase was changed to partial slip condition with a specularity coefficient of 0.1 in order to account for the solid properties of the polymer phase.

In order to generate a stable polymer bed, only gas is fed for 2.0 s until steady-state is reached. In a second step the polymer particles with a density of 950 kg/m^3 and a diameter of 1.0 mm, which corresponds to the experimental setup [10] are fed in the reactor for 2.5 s. To achieve a polymer bed of 2.0 kg the polymer phase is fed through the jacket inlet with a velocity of 0.1 m/s and with a volume fraction of 0.03942. After the polymer feeding step, only air is send through the GSVR until 8.0 s of simulation time has passed. In all simulations the polymer particles remained in the reactor generating a stable bed of 2.0 kg. This suggests that the 20° injection slot angle is still not the design limit and investigating an injection slot angle of 25° would be worthwhile as long as the particles don't leave entrained with the gas phase through the reactor outlet.

The dependency of the operating conditions on the geometric parameters will be divided into three parts. First the bed dynamics in terms of polymer volume fraction and packing will be investigated. In a second part the focus will be on the relative differences in azimuthal and radial velocity in function of increasing injection angle and increasing slot thickness. A third point will be relating these velocities to process conditions, with the emphasis on heat transfer coefficients. Before going into more detail on the dependency of the operating conditions on the geometric parameters, two observations were made:

A first observation comparing the two-phase simulations with the gas only simulations, is that the air velocity inside the reactor of the simulations with the polymer particles in the GSVR decreases significantly compared to gas only simulations. The air injection velocity at the slots outlet is the same in both cases, but in the case of a polymer bed the momentum of the air phase is transferred to the polymer phase in order to generate a rotating bed.

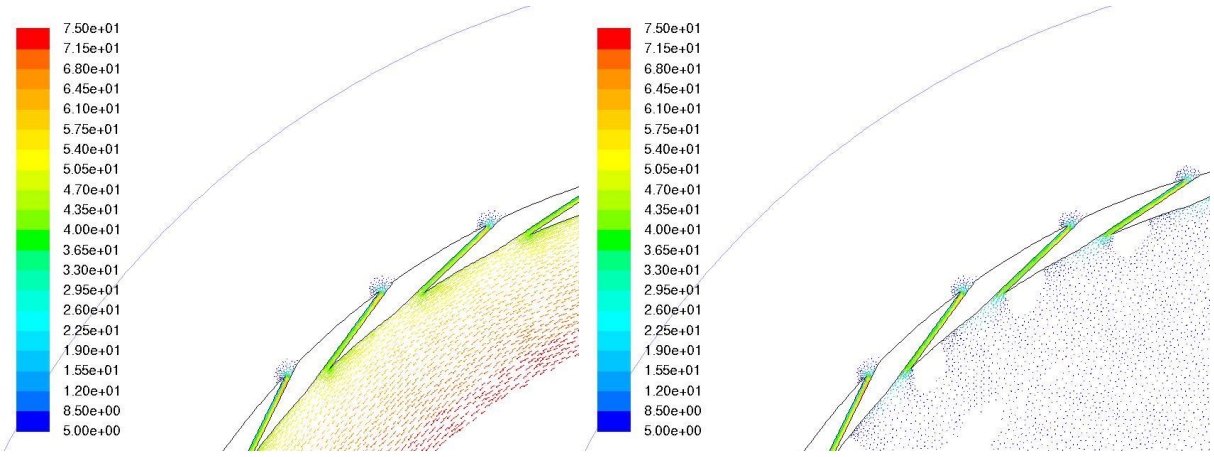

Figure 2-8: Vector plots of the air velocity in a GSVR with 2.0 mm injection slot thickness and 10° injection angle after 2.0 s at the end of the gas only stage (left) and after 8.0 s when a stable polymer bed has been formed (right).

A second observation is that feeding 1.0 mm polymer particles through 1.0 mm injection slots is impossible as shown in Figure 2-9. This result is consistent with the intuition, however the polymer phase is assumed to be fluidized. The polymer feeding fails because the pressure drop over the injection slots is too high. Another feeding possibility will have to be considered for these simulations, for example feeding to the reactor via an inclined inlet tube at specific locations in the reactor chamber as in the experimental setup or by a user-defined function, which would homogeneously distribute the feeding over the entire GSVR between two specific radii. For the rest of the geometric study no simulations were performed with 1.0 mm injection slot thickness in order to keep the feeding process similar for all simulations.

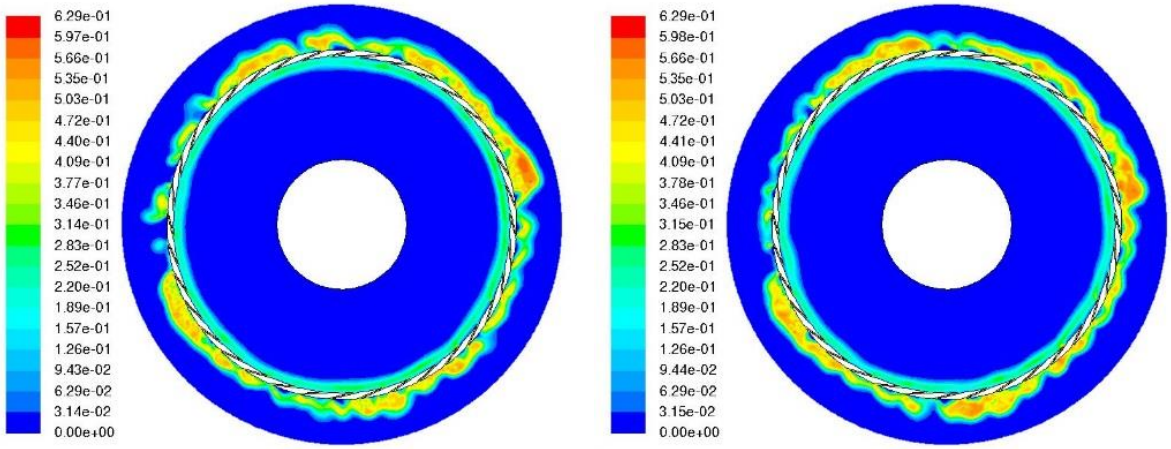

Figure 2-9: Contour plots of the polymer volume fraction after 4.0 s (left) and 9.0 s (right) of simulation time for an injection slot thickness of 1.0 mm with a 10° injection slot angle.

The remaining geometries with an injection slot thickness of 1.5 mm and 2.0 mm with varying injection slot angle will be discussed in the next chapter. The polymer volume fraction and polymer distribution inside the reactor will first be compared before focusing on the azimuthal and radial velocities which describe the fluidized bed dynamics in more detail.

2.5.1. Solids volume fraction

Contour plots of volume fraction can give a first visual representation of the fluidized bed dynamics in the gas-solid vortex reactor. For instance Figure 2-10 shows that there is an azimuthal dependency of the volume fraction for both simulations with the 10° and 20° injection angle, channeling of gas occurs through the fluidized bed. The maximum packing limit is reached in several zones in both cases.

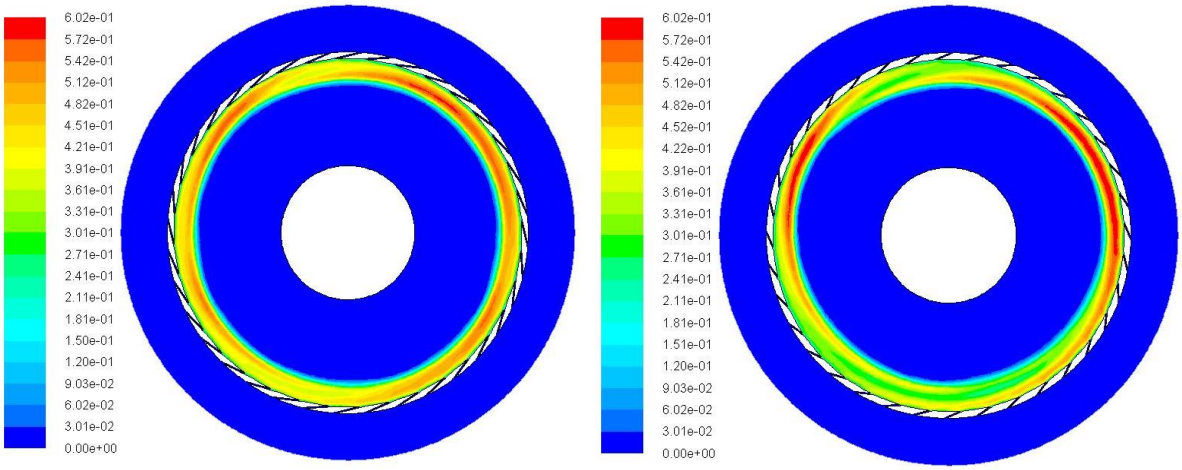

Figure 2-10: Contour plots of the polymer volume fraction after 8.0 s of simulation time for an injection slot thickness of 2.0 mm with a 10° injection angle (left) and a 20° injection angle (right).

In order to have a more quantitative representation of this angular dependency the volume fraction of the polymer phase is given in Figure 2-12. The radial lines over which the volume fractions are calculated are shown in Figure 2-11.

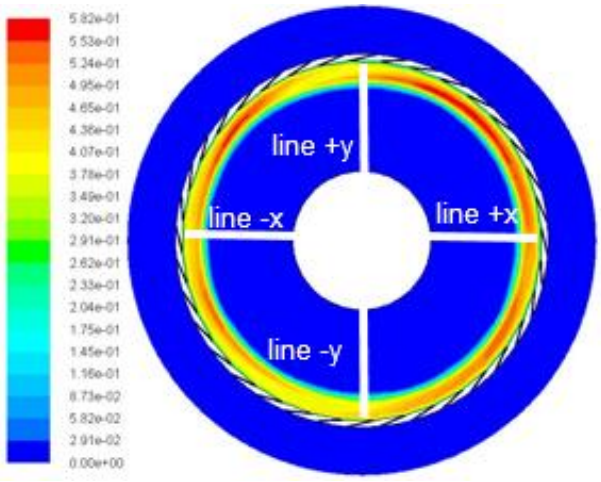

Figure 2-11: Visual representation of the cross-sections used to generate plots of the volume fraction in function of radial distance for the 2.0 mm injection slot thickness and 10° injection angle geometry.

To compare the simulation results of the different GSVR geometries, properties such as volume fraction but also azimuthal and radial velocity will have to be averaged by integrating over a specific radius or integrating over a time period to get the appropriate average properties.

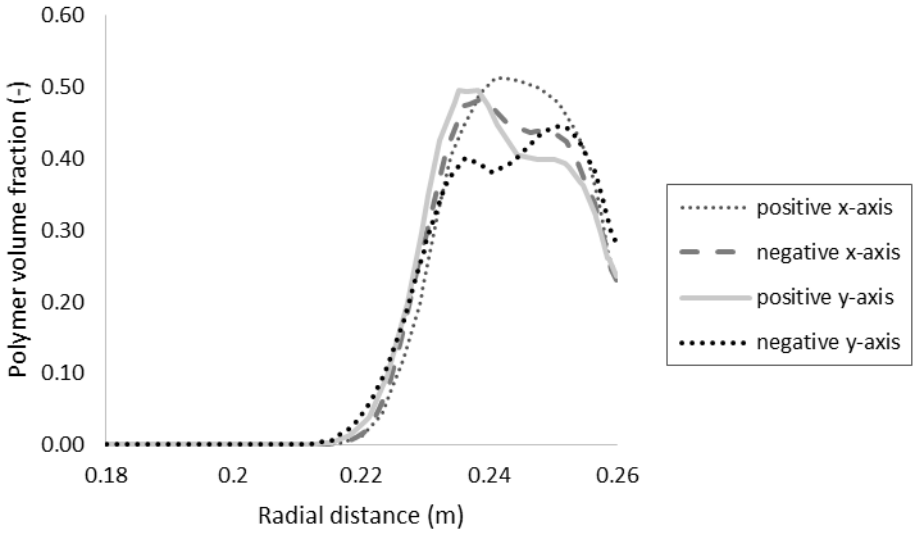

Figure 2-12: Polymer volume fraction in function of radial distance for the various cross-sections show in Figure 2-11.

Another observation that can be drawn from the contour plots of the polymer volume fraction is that the angular dependency of the volume fraction is more pronounced for larger injection slot angles. A quantitative expression of this observation is formulated in Table 2-5 by taking the standard deviation of the average polymer volume fraction at specific radii as shown later in Figure 2-16.

Table 2-5: Standard deviation of the polymer volume fraction at specific radii for a GSVR geometry with 2.0 mm injection slot thickness.

	r = 0.240 m	**r = 0.245 m**	**r = 0.250 m**	**r = 0.255 m**
10°	0.058	0.061	0.042	0.032
15°	0.094	0.092	0.076	0.063
20°	0.116	0.106	0.087	0.071

This quantitative validation for the slugging behavior only holds if the standard deviation is larger for the same or even smaller average polymer volume fractions. Table 2-6 shows the average polymer volume fractions at the same radii as the standard deviation polymer volume fractions shown previously. All polymer beds have a height of 4 cm and are situated between 0.22 and 0.26 m as can be seen on Figure 2-12.

Table 2-6: Average polymer volume fraction at specific radii for a GSVR geometry with 2.0 mm injection slot thickness.

	r = 0.240 m	r = 0.245 m	r = 0.250 m	r = 0.255 m
10°	0.489	0.474	0.462	0.413
15°	0.434	0.454	0.464	0.412
20°	0.427	0.442	0.458	0.407

Contour plots of the polymer volume fraction for a GSVR with varying slot thickness are show on Figure 2-13. The bed height is comparable for both simulations as shown in Figure 2-14, but the velocity profiles inside the reactor chamber differ significantly as shown in the next section.

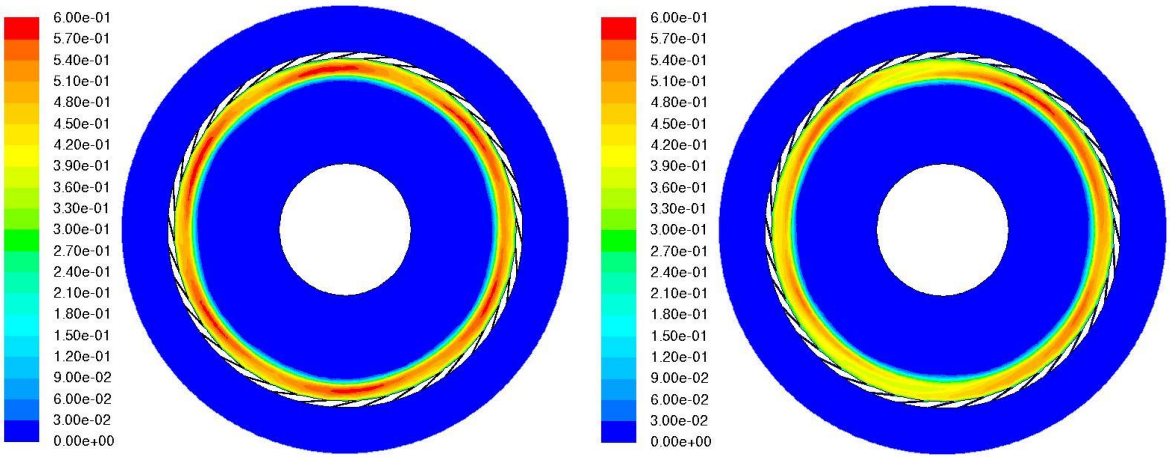

Figure 2-13: Contour plots of the polymer volume fraction after 8.0 s of simulation time for an injection slot angle of 10° with a 1.5 mm injection slot thickness (left) and a 2.0 mm injection slot thickness (right).

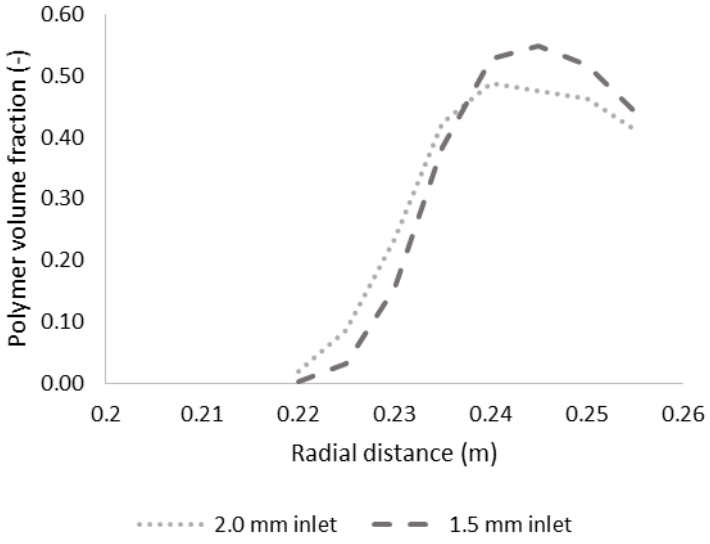

Figure 2-14: Representation of the bed height after 8.0 s of simulation time for an injection slot angle of 10° with an injection thickness of 2.0 mm and 1.5 mm

2.5.2. Solids velocity field

When comparing different injection slot angles and injection slot thicknesses, the goal is to determine what is the cost of selecting a geometry with wider injection slots and larger angles, which is easier to construct, compared to a smaller injection slot and a smaller injection angle, which is expected to result in favorable high azimuthal and slip velocities.

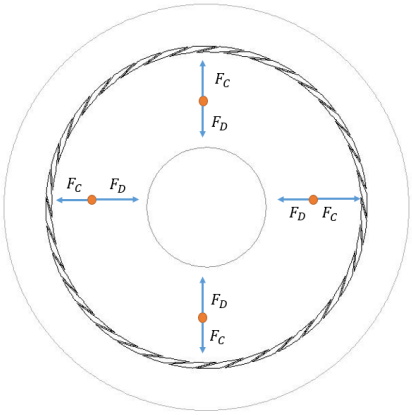

Figure 2-15: Schematic representation of the radial forces acting on a particle in the polymer bed at different positions in the GSVR. The gravitational forces are neglected since it is assumed that the centrifugal acceleration is larger than the gravitational constant g.

The fluidized bed dynamics inside the GSVR are determined by the ratio between the radial drag and centrifugal forces working on the polymer particles. A higher centrifugal force reduces the bed height and the radial drag force tends to expand the bed. A visual representation without taking the gravitational forces into consideration is given in Figure 2-15.

As discussed previously and shown in Figure 2-12, there is an angular dependency of the volume fraction. Since this is also the case for the azimuthal and radial velocity profiles, the values will be averaged over the entire 360° section for specific radii shown in Figure 2-16:

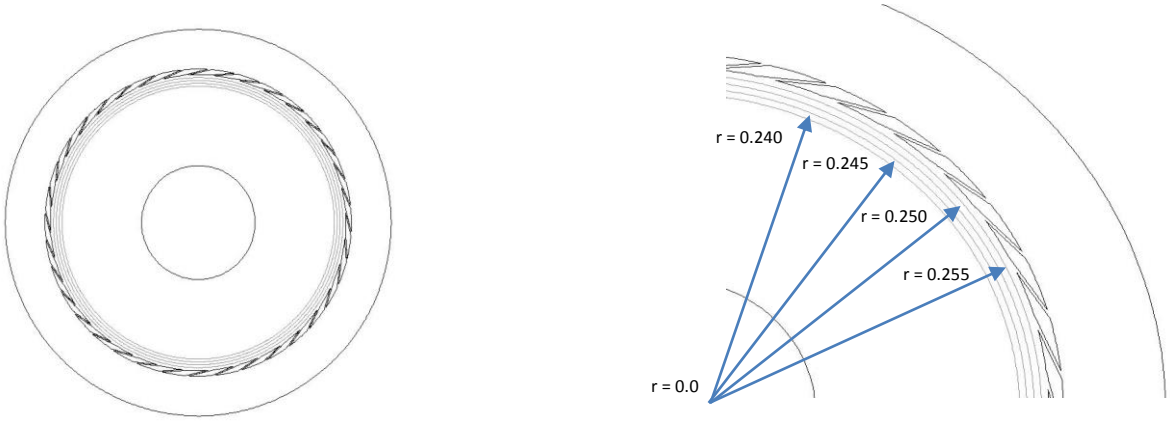

Figure 2-16: The azimuthal and radial velocity at a radius of r = 0.240 m, 0.245 m, 0.250 m, 0.255 m will be averaged over the entire 360° reactor geometry.

Solids azimuthal velocity

By averaging the azimuthal velocity over a constant radius, averaged azimuthal velocities for a constant injection angle and a varying slot thickness can be compared as shown in Figure 2-17.

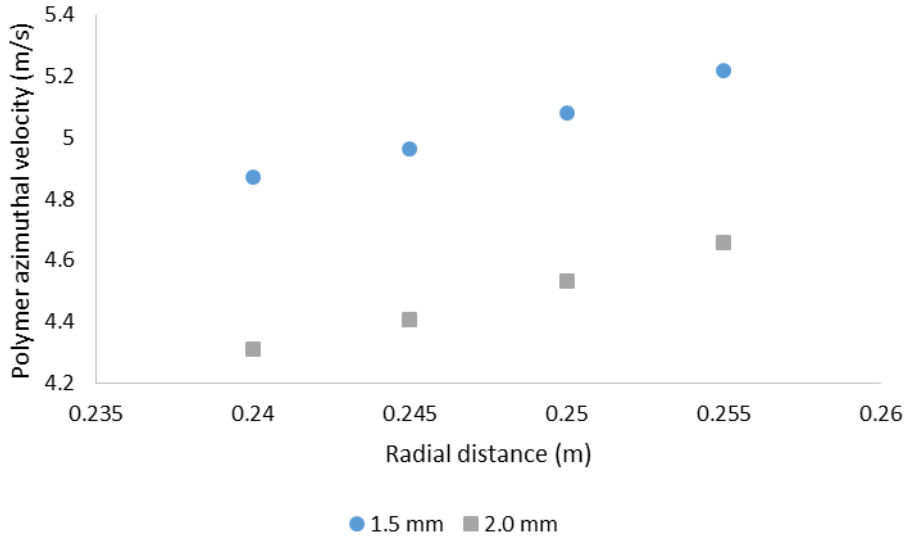

Figure 2-17: Azimuthal velocity of the polymer particles at specific radii for a GSVR geometry with 20° injection angle and with varying injection slot thicknesses.

As intuitively expected the azimuthal velocity of the polymer phase in a GSVR with constant injection angle decreases with increasing slot thickness. This increase is related to an increased velocity of the gas phase in the injection slots due to reduction of available injection slot area while keeping the volumetric feeding rate constant. In case of a higher gas phase velocity, more momentum will be transferred to bring the polymer bed in rotation. Reducing the injection slot thickness to 1.5 mm results in a gas velocities up to 75 m/s inside the injection slots compared to 50 m/s maximum for 2.0 mm injection slot thickness geometries, this increase is related to the conservation of mass. The solid azimuthal velocity increases nearly constant along the bed as shown in Figure 2-17.

In a next step the azimuthal velocity will be compared for GSVR geometries with a constant injection slot thickness but a varying injection slot angle. The expected results of a decreasing azimuthal polymer velocity for increasing injection slot angle are in agreement with the results obtained from simulations as shown in Figure 2-18.

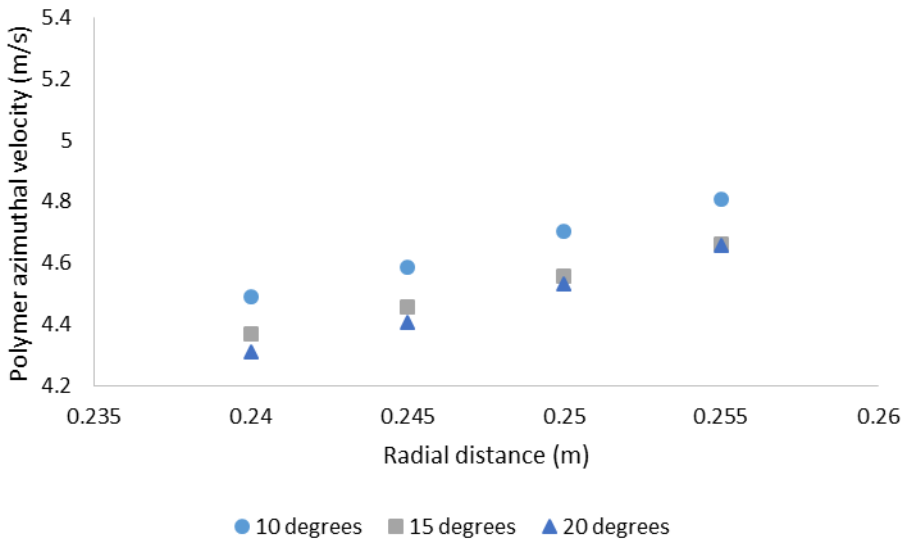

Figure 2-18: Azimuthal velocity of the polymer particles at specific radii for a GSVR geometry with 2.0 mm slot thickness and a varying injection slot angle.

At first sight, these differences in azimuthal velocity of the polymer phase seem rather negligible as shown in Figure 2-18. On average a reduction of 3 % in azimuthal velocity is observed when increasing the injection slot angle from 10° to 15° and a reduction of 4 % is observed when an injection angle is varied from 10° to 20°. However the differences in absolute value for azimuthal velocity are rather large compared to the jacket superficial velocity of 1.433 m/s for the air phase.

Another interesting aspect of varying the geometric parameters is that stepwise changing the injection slot angle or a change in the injection slot thickness will affect the azimuthal momentum change to different degrees. This difference in azimuthal momentum is calculated for several cases to see which geometric adjustments affect the flow more. The total gas momentum can always be divided in a radial and an azimuthal contribution. Increasing the injection slot thickness from 1.5 mm to 2.0 mm corresponds to a decrease of azimuthal momentum of around 1/3. Changing the injection slot angle from 20° to 15°, the angular momentum is expected to increase around 2.8 % and further reducing the injection slot angle to 10° is expected to result in an increase of angular momentum of 2.0 %. The formula used to calculate the difference in angular momentum for a decreases of Δx in injection slot angle is given in (2.18):

$$\Delta p = \frac{\cos(x - \Delta x) - \cos(x)}{\cos(x)} \tag{2.18}$$

Gas swirl ratio

In a second comparison, the geometric dependency of the swirl ratio will be investigated. The swirl ratio is the ratio of the azimuthal and radial velocity. One of the main differences between static gas-solid vortex reactors and rotating geometry fluidized bed reactors is that the azimuthal and radial velocities cannot be controlled independently for the static gas-solid vortex reactors. This characteristic makes the investigation of the dependency of the swirl ratio on the geometric reactor parameters interesting for selecting an optimal reactor design [11].

The swirl ratio of the gas phase will be calculated. The radial velocity of the polymer phase can be considered negligible because the polymer bed is rotating at a more or less fixed radial position. The gas swirl ratio indirectly gives an idea how long the entering gas is in contact with the solids bed. A high swirl ratio indicates that the gas will complete more turns in the bed and hence the gas-solid contact time will increase. The averaged radial velocity of the gas phase inside the polymer bed region for 1.5 mm and 2.0 mm injection slot thickness is given in Table 2-7. Closer to the injection slots, the radial velocity for the 1.5 mm injection slot geometry is higher because of the higher velocity of the gas phase through the injection slots. At the end of the polymer bed at a radius of 0.220 m, the radial velocity for the 1.5 mm injection slot geometry is lower compared to larger injection slots, suggesting that more momentum is transferred to the polymer phase.

Table 2-7: Radial velocity of the gas phase at specific radii for a GSVR geometry with 20° injection angle.

	r = 0.220 m	**r = 0.230 m**	**r = 0.240 m**	**r = 0.250 m**
1.5 mm	2.270 m/s	3.002 m/s	3.993 m/s	3.842 m/s
2.0 mm	2.482 m/s	3.265 m/s	3.530 m/s	3.595 m/s

The averaged radial velocities of the gas phase for a constant injection slot thickness and a varying injection slot angle are given in Table 2-8. These values will be used together with the tangential gas phase velocities for the calculation of the swirl ratios.

Table 2-8: Radial velocity of the gas phase at specific radii for a GSVR geometry with 2.0 mm injection slot thickness.

	r = 0.220 m	**r = 0.230 m**	**r = 0.240 m**	**r = 0.250 m**
10°	2.251 m/s	2.990 m/s	4.027 m/s	3.713 m/s
15°	2.408 m/s	3.237 m/s	3.633 m/s	3.647 m/s
20°	2.482 m/s	3.265 m/s	3.530 m/s	3.595 m/s

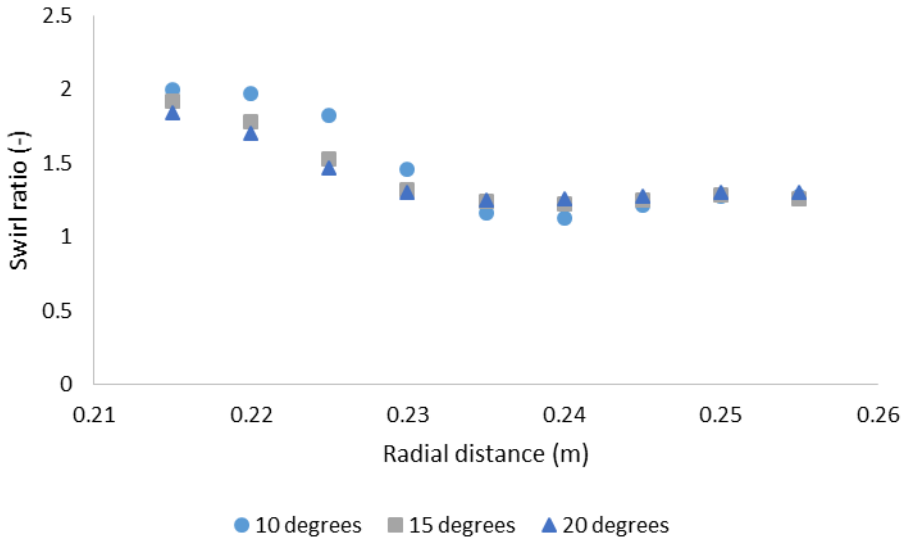

Figure 2-19: Swirl ratio of the gas phase in function of radial distance for a GSVR geometry with 2.0 mm slot thickness.

The ratio of the azimuthal and radial gas phase velocities for a constant slot thickness is shown above in Figure 2-19 and for a constant injection slot angle with a varying slot thickness below in Figure 2-20. These swirl ratio plots are completely different from the gas phase only simulations because of the momentum transfer from the gas phase to the polymer phase.

The figures show that in the solid bed the gas swirl ratio is lower than downstream of the bed. It can be deduced that particles are causing gas to bend radially by providing resistance. The gas flow out of the polymer bed does not encounter this resistance causing the swirl ratio to rise again.

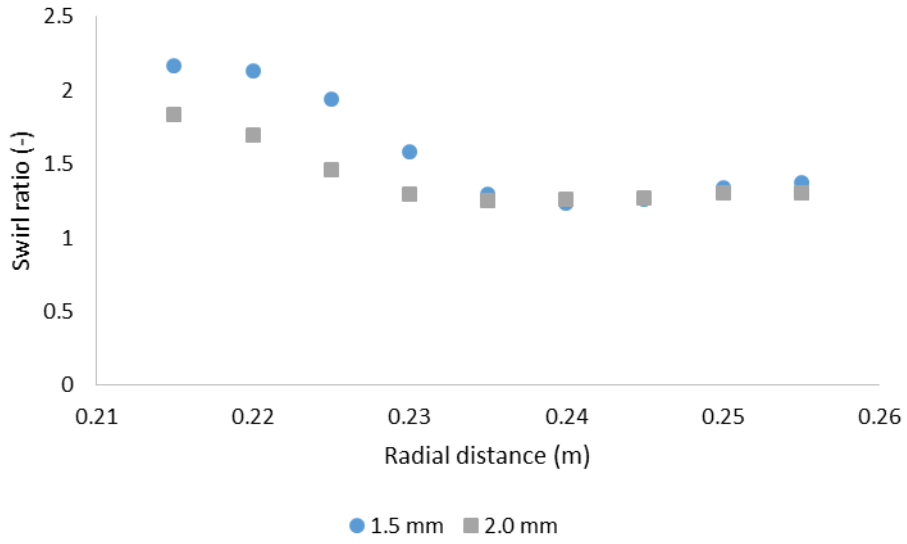

Figure 2-20: Swirl ratio of the gas phase in function of radial distance for a GSVR geometry with 20° injection slots.

2.5.3. Centrifugal and drag forces

The fluid-solid momentum equation in ANSYS Fluent uses a multi-fluid granular model to describe the flow behavior of a fluid-solid mixture. The conservation of momentum at steady-state without lift or virtual mass forces for the solid phase is given by:

$$\varepsilon_s . \nabla p = K(v_g - v_s) \tag{2.19}$$

With K the fluid-solid momentum exchange coefficient and ε_s the solid void fraction. Using the Gidaspow drag model for the fluid-solid interactions, the fluid-solid exchange coefficient is given by the Ergun equation for dense fluidized beds [3, 12]:

$$K = 150\frac{\varepsilon_s(1-\varepsilon_l)\mu_l}{\varepsilon_l d_s^2} + 1.75\frac{\varepsilon_s \rho_l |v_g - v_s|}{d_s} \tag{2.20}$$

The drag force operating on the solid particle as shown in Figure 2-15 is given by the following experimental expression defined by de Broqueville and De Wilde [13] and states that the value of 1/36 allows no mixing or overlap between gases injected via successive gas inlet slots. In the absence of mixing between gases injected via successive gas inlet slots, the fluidization gas injected via a given gas inlet slot is allowed to cover a 10° section. This factor of 1/36 was added to more accurately describe the experimentally observed results.

$$F_D = K v_{slip}\frac{V\varepsilon}{36} = \frac{150}{d_p^2}\frac{(1-\varepsilon)^2}{\varepsilon} v_{slip}\frac{V}{36} + \frac{1.75\rho_g}{d_p}(1-\varepsilon)v_{slip}^2\frac{V}{36} \tag{2.21}$$

A value for the centrifugal force can be estimated for the case of a stable or semi-stable bed as:

$$F_c = \frac{W_{s,max}}{36}\frac{v_{s,t}^2}{r} \tag{2.22}$$

Indicative value for the acceleration that the bottom of a bed in a GSVR is experiencing is given in function of the drag and centrifugal force by $(F_C - F_D)\left({}^{m_{bed}}/_{36}\right)^{-1}$. Since these expressions for centrifugal and drag forces are based on experimental behavior, their relative values are of more importance than their absolute values when selecting the desired GSVR process conditions.

These experimentally derived expressions for centrifugal and drag forces operating on the polymer bed correspond to other formulations encountered in literature [14]. The Ergun equation is given by:

$$F_{D,r} = 150\frac{\mu_g(1-\varepsilon)^2}{\varepsilon^3 d_p^2}v_{g,r} + 1.75\frac{(1-\varepsilon)\rho_g}{\varepsilon^3 d_p}v_{g,r}^2 \tag{2.23}$$

The centrifugal force per unit volume is proportional to the racial coordinate assuming the angular velocity ω remains constant throughout the bed:

$$F_{C,r} = \rho_s(1-\varepsilon)r\omega^2 \tag{2.24}$$

However for the GSVR, the angular velocity ω is dependent on the radius and can be calculated by rescaling the azimuthal velocity, v_{θ,r_m}, at a specific radius:

$$\omega = \frac{v_{\theta,r_m}}{r_m} \tag{2.25}$$

Drag and centrifugal forces for varying injection slot thickness are given in Figure 2-21, an extra geometry with 2.5 mm injection slot thickness was added to visualize the increase of drag and centrifugal forces with decreasing slot thickness. Figure 2-22 shows the drag and centrifugal forces operating in a GSVR for varying injection slot angles.

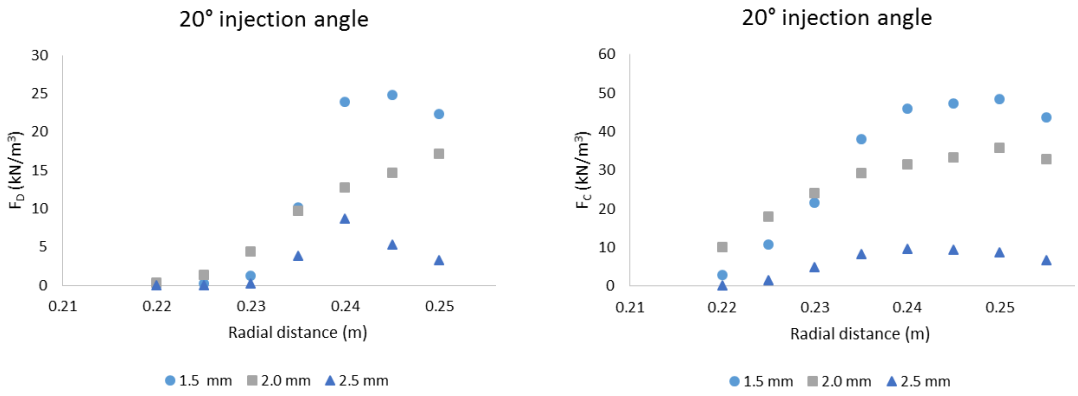

Figure 2-21: Drag (left) and centrifugal (right) forces working on the polymer bed in function of radial distance for a GSVR geometry with 20° injection slot angle.

Integrating the drag and centrifugal forces over the polymer bed volume results in the total drag and centrifugal forces given in Table 2-9. Because of the really low centrifugal and drag forces for the 2.5 mm case, it is possible that in experimental setups gravitational forces will have an influence on the bed dynamics. The ratio of the centrifugal over the drag forces appears to be independent of the slot thickness as shown in the last column of Table 2-9.

Table 2-9: Total drag and centrifugal force working on the polymer bed for a GSVR geometry with 20° injection slot angle.

Slot thickness	Drag force (N)	Centrifugal force (N)	Ratio F_C/F_D (-)
1.5 mm	40.91	85.11	2.08
2.0 mm	29.65	63.62	2.15
2.5 mm	9.53	16.34	1.71

There appears to be no clear difference between the forces operating on the polymer bed for injection slot angles higher than 15° as can be seen in Figure 2-22.

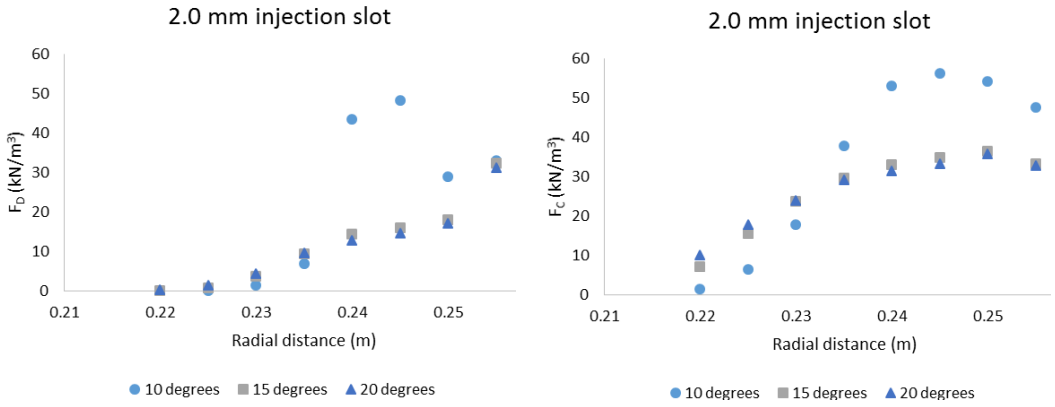

Figure 2-22: Drag (left) and centrifugal (right) forces working on the polymer bed in function of radial distance for a GSVR geometry with 2.0 mm injection slot thickness.

Table 2-10: Total drag and centrifugal force working on the polymer bed for a GSVR geometry with 2.0 mm injection slot thickness.

injection angle	Drag force (N)	Centrifugal force (N)	Ratio F_C/F_D (-)
10°	63.43	97.87	1.54
15°	31.38	64.52	2.06
20°	29.65	63.62	2.15

The centrifugal force is higher than the drag force operating in the bed, generating a stable bed where the polymer particles do not elutriate with the gas phase. The total gravitational force on the bed is in the order of 19.62 N, calculated using the straightforward relation that the force of gravity is proportional to the mass with a factor g, the acceleration of gravity. The centrifugal forces working on the polymer bed are a multiple of the gravitational forces ranging from 8 to 10 g for the geometries with varying injection slot angle shown in Table 2-10, this may lead to the conclusion that neglecting the gravitational acceleration might be practicable.

2.5.4. Heat transfer coefficient

In the case of granular flows ANSYS Fluent uses a Nusselt number correlation by Gunn [15] which is applicable in a porosity range of 0.35 – 1.0 and for Reynolds numbers up to 10^5:

$$Nu_p = \frac{h_p . d_p}{\lambda_g} = (7 - 10\varepsilon_g + 5{\varepsilon_g}^2)(1 + 0.7 . Re_p^{0.2} . Pr^{0.5}) + (1.33 - 2.4\varepsilon_g + 1.2{\varepsilon_g}^2) . Re_p^{0.7} . Pr^{0.5} \quad (2.25)$$

In this equation, h_p is the particle-scale convective heat transfer coefficient, ε_g is the gas volume fraction, λ_g the thermal conductivity of the gas, Pr the Prandtl number of the gas phase and Re_p the particle Reynolds number based on the superficial gas-solid slip velocity:

$$Re_p = \frac{\rho_p . d_p . |v_g - v_s|}{\mu_g} \quad (2.26)$$

The cold-flow Fluent simulations were performed without solving the energy equation. It has to be pointed out that the heat transfer coefficient is calculated during the post processing of the simulations, based on the gas-solid slip velocity, the gas volume fraction and the Prandtl number. The Prandtl number is a dimensionless number defined as the ratio of momentum diffusivity to thermal diffusivity and is usually assumed to be 0.707 for air at room temperature.

Heat transfer coefficients in function of radial distance for varying slot thickness are given below in Figure 2-23, again an additional geometry was added. Apparently the average heat transfer coefficient over the bed does not change significantly when going from a 1.5 mm to a 2.0 mm injection slot thickness.

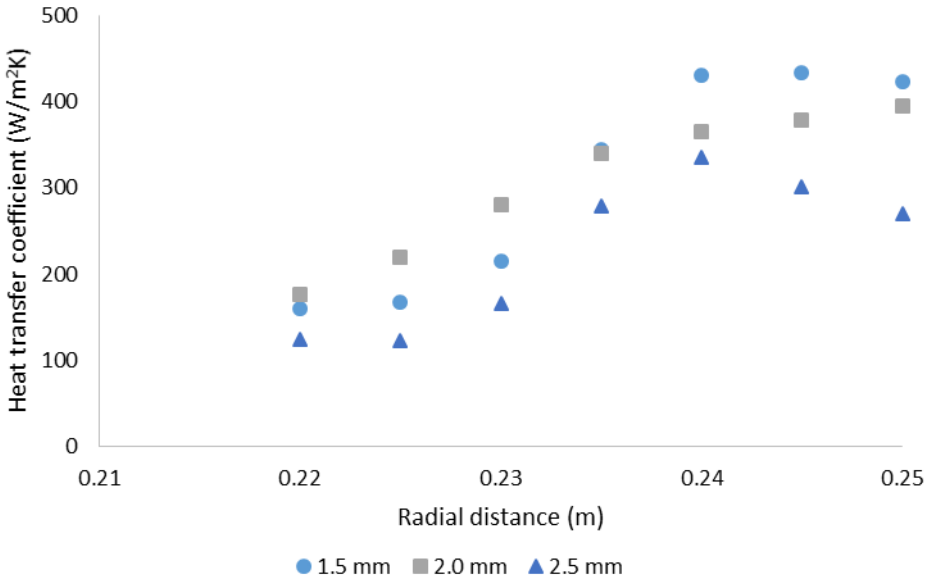

Figure 2-23: Heat transfer coefficient in function of radial distance for a GSVR geometry with 20° injection slot angle.

By taking a closer look at Figure 2-24, it can be observed that for the simulations with an injection slot angle larger than 10° there is on average a lower heat transfer coefficient between the two phases. Between the 15° and 20° injection slot, the differences are less pronounced.

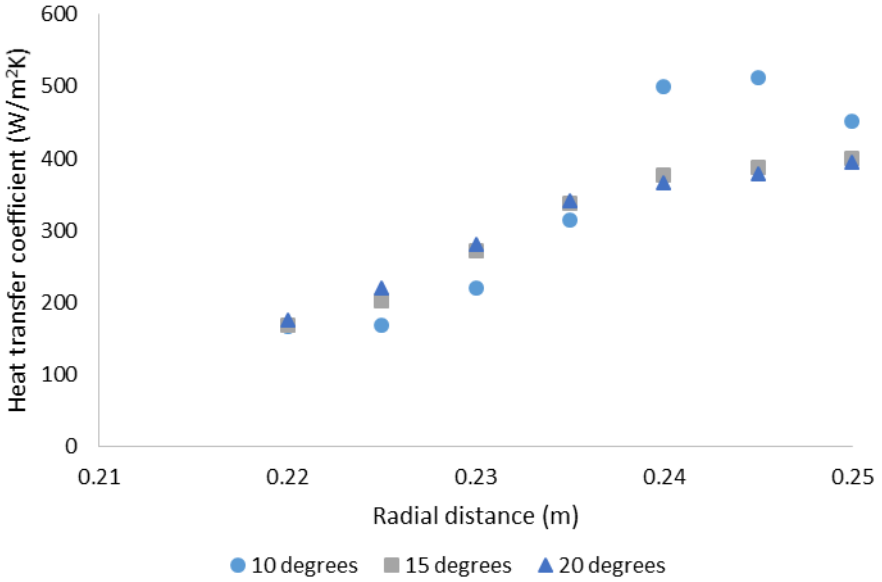

Figure 2-24: Heat transfer coefficient in function of radial distance for a GSVR geometry with 2.0 mm injection slot thickness.

2.6. Conclusion

The goal of this chapter was to determine the difference in operating conditions when selecting a less strict GSVR geometry with wider inlet slots and a higher injection angle compared to the most rigorous reactor geometry with 1.0 mm injection slot thickness and 10° injection angle.

After specifying an appropriate mesh for the different geometries, gas only simulations were performed. For different injection slot thicknesses an increase in swirl ratio and azimuthal velocity was observed for GSVR geometries with a reduced injection slot thickness. For the gas only simulations, changing the injection slot angle magnitude did not result in different gas velocity profiles.

Two-phase simulations were performed with a polymer bed inside the GSVR while feeding the same volumetric gas flow rate as in the gas only simulations. A first observation was that the polymer phase could not be fed through the reactor inlet slots for the 1.0 mm geometries. For the other simulations a polymer bed was formed where channeling of gas occurred through the bed resulting in time and angular dependent phase properties. Averaging of velocity profiles was necessary to be able to quantitatively compare the operating conditions of the various simulations.

Because of the momentum transfer from the gas phase to the polymer phase to keep the fluidized polymer bed in motion, the velocity profiles of the two-phase simulations are significantly different from the gas only simulations. For the two-phase simulations an increase of azimuthal velocity of the polymer phase was observed for smaller injections slot angles. For the two-phase simulations an increase in angular velocity was also observed for numerical simulations where the gas phase is injected more tangentially. However this difference in polymer and gas tangential velocity is less pronounced for a varying injection slot angle compared to a change in injection slot thickness. This observation could be verified by decoupling the momentum fed through the injection slots in a radial and a azimuthal contribution. The change in azimuthal momentum suggests that varying the injection slot thickness will have more influence on the azimuthal velocity than varying the injection slot angle.

When comparing heat transfer coefficients inside the polymer bed it was observed that reducing the injection slot thickness and selecting a more azimuthal injection angle results in higher heat transfer coefficients, especially in the regions where the polymer bed is the most dense.

2.7. Bibliography

1. Jenkins, J. and S. Savage, *A theory for the rapid flow of identical, smooth, nearly elastic, spherical particles.* Journal of Fluid Mechanics, 1983. **130**: p. 187-202.
2. Lun, C., et al., *Kinetic theories for granular flow: inelastic particles in Couette flow and slightly inelastic particles in a general flowfield.* Journal of fluid mechanics, 1984. **140**: p. 223-256.
3. Gidaspow, D., R. Bezburuah, and J. Ding, *Hydrodynamics of circulating fluidized beds: Kinetic theory approach*. 1991. Medium: ED; Size: Pages: (8 p).
4. Ogawa, Y. and P. Diosey, *Surface roughness and thermal stratification effects on the flow behind a two-dimensional fence—I. Field study.* Atmospheric Environment (1967), 1980. **14**(11): p. 1301-1308.
5. Syamlal, M., W. Rogers, and T.J. O'Brien, *MFIX documentation: Theory guide.* National Energy Technology Laboratory, Department of Energy, Technical Note DOE/METC-95/1013 and NTIS/DE95000031, 1993.
6. Schaeffer, D.G., *Instability in the evolution equations describing incompressible granular flow.* Journal of differential equations, 1987. **66**(1): p. 19-50.
7. Bloor, M.I.G. and D.B. Ingham, *The flow in industrial cyclones.* Journal of Fluid Mechanics, 1987. **178**: p. 507-519.
8. Liu, Z. and T. Ishiharab. *Effects of the swirl ratio on the turbulent flow fields of tornado-like vortices by using LES turbulent model*. in *Proceedings of the 7th International Colloquium on Bluff Body Aerodynamics and Applications*. 2012.
9. Simonin, C. and P. Viollet, *Predictions of an oxygen droplet pulverization in a compressible subsonic coflowing hydrogen flow.* Numerical Methods for Multiphase Flows, FED91, 1990: p. 65-82.
10. Ekatpure, R.P., et al., *Experimental investigation of a gas–solid rotating bed reactor with static geometry.* Chemical Engineering and Processing: Process Intensification, 2011. **50**(1): p. 77-84.
11. De Wilde, J. and A. de Broqueville, *Rotating fluidized beds in a static geometry: experimental proof of concept.* AIChE journal, 2007. **53**(4): p. 793-810.
12. Ergun, S., *Fluid flow through packed columns.* Chem. Eng. Prog., 1952. **48**: p. 89-94.
13. de Broqueville, A. and J. De Wilde, *Numerical investigation of gas-solid heat transfer in rotating fluidized beds in a static geometry.* Chemical Engineering Science, 2009. **64**(6): p. 1232-1248.
14. Kovacevic, J.Z., et al., *Solids velocity fields in a cold-flow Gas–Solid Vortex Reactor.* Chemical Engineering Science, 2015. **123**: p. 220-230.
15. Gunn, D.J., *Transfer of heat or mass to particles in fixed and fluidised beds.* International Journal of Heat and Mass Transfer, 1978. **21**(4): p. 467-476.

Chapter 3: Fast Biomass Pyrolysis in a Gas Solid Vortex Reactor

Table of Contents

List of Figures

List of Tables

3.1. Introduction

The gas solid vortex reactor has the ability to meet the necessary criteria for fast biomass pyrolysis. The high gas-solid slip velocities, that result in high convective heat transfer coefficients and short gas phase residence time in the reactor, ensure a high heat transfer rate, precise temperature control and rapid cooling of the pyrolysis vapors, the three main characteristics for fast pyrolysis processes outlined by Bridgwater and Peacocke [1].

The goal of this chapter is to step-by-step model fast biomass pyrolysis in a gas-solid vortex reactor with the CFD software package ANSYS Fluent 15.0. The simulations will be set up by first modeling a stable sand bed inside the GSVR. In a second step lignocellulosic biomass will be fed inside the GSVR. The biomass-sand interactions will be investigated before enabling the fast biomass pyrolysis kinetics. The final goal is to generate a stable reactor bed at temperatures suitable for fast biomass pyrolysis 450 – 500 °C, in order to calculate biomass conversions and to compare the results with the classical fluidized riser reactors used for fast biomass pyrolysis. All simulations were performed in the same GSVR geometry with 2.0 mm injection slot thickness and 10° injection slot angle.

The performed 360° numerical simulations will also be compared to the work of R. Ashcraft on fast biomass pyrolysis in a 40° section of a GSVR [2]. Possible further investigation routes and considerations for building a gas-solid vortex reactor pilot unit will be discussed at the end.

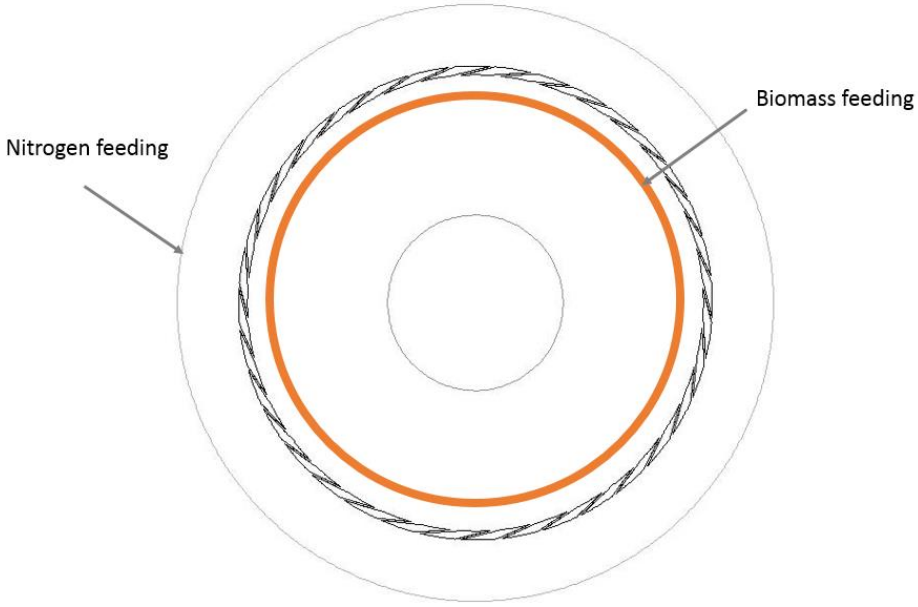

Figure 3-1: Visual representation of the GSVR setup used during the CFD simulations.

3.2. Biomass pyrolysis model

3.2.1. Definition of phases

In order to simulate fast biomass pyrolysis in a gas solid vortex reactor using ANSYS Fluent, four Eulerian phases have to be considered for the simulations: the primary gas phase, the biomass particulate phase, the char particulate phase and the sand particulate phase.

Several components of these phases are modeled as pseudo-components with thermochemical properties that have been specified to achieve certain bulk enthalpies of reaction and appropriate stoichiometric relationships. The breakdown of the Eulerian phases as shown in Table 3-1, is the most commonly used in literature for fast biomass pyrolysis [3].

Table 3-1: Overview of the Eulerian phases defined as mixture materials. The biomass phase contains in total six biomass species since the reaction mechanism makes a distinction between virgin (v) and activated (a) biomass.

Gas phase	Biomass phase	Char phase	Sand phase
nitrogen*	cellulose (v/a) ^{r}	cellulose char^{p}	sand*
tar^{p}	hemicellulose (v/a) ^{r}	hemicellulose char^{p}	
pyrolysis gas^{p}	lignin (v/a) ^{r}	lignin char^{p}	
water*			

* inert phases, ^{p} products, ^{r} reactants

The gas phase contains nitrogen which is fed through the reactor inlet jacket at 923 K, water which is fed in the gaseous phase together with the biomass and at last tar and pyrolysis gas which are formed by the conversion of activated biomass as shown in the reaction network in Figure 3-2 [4].

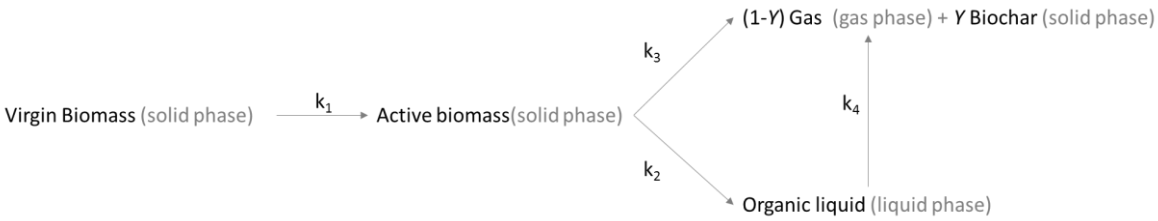

Figure 3-2: Reaction steps for the implemented multiple component multiple-step devolatilization scheme.

Water is fed together with the biomass phase using a user-defined source term. The enthalpy of vaporization is included using a heat sink term in the gas phase. Dealing with the vaporization in a discrete manner in Fluent is not evident and certainly not the focus of this study. In practice it is almost impossible to obtain perfectly dry biomass. Hence 10 wt% of the fed biomass (dry basis) will be

assumed to be water vapor. Nitrogen and water properties can be found in the Fluent database. The properties of tar were modeled after phenol and the properties of ethylene were used to model pyrolysis gas [5-7].

Biomass consisting of 36 wt% cellulose, 17 wt% hemicellulose and 47 wt% lignin, is homogeneously fed inside the reactor chamber at 300 K with a feeding location positioned between radial values of 0.25 and 0.255 m as shown schematically in Figure 3-1, close to the gas injection slots. In a first reaction step these virgin components are activated as shown in the reaction network displayed in Figure 3-2. The biomass properties were taken from various literature sources as shown in Appendix E [8-10].

The char phase contains three char species that are each associated with a biomass species. The reason for this distinction between char components is that each biomass component generates a specific amount of char per kg of biomass, resulting in char species with different densities.

In fast biomass pyrolysis reactions, the sand phase is used as a high-density inert heat carrier. The sand particles are supposed to break up biomass particle agglomerates in an experimental setup. A less obvious contribution of the sand phase to the GSVR bed dynamics is the fact that due to the high density of sand, momentum is transferred form the fed gas resulting in significantly lower gas velocities inside the GSVR compared to simulations where sand is not present, these lower velocities facilitate the homogeneous biomass feeding. In order to get a more extensive overview of the dynamic properties of the various phases implemented in the numerical simulations, the reader is referred to Appendix E.

3.2.2. Phase interactions

The gas phase is defined as the primary phase using the ideal gas law for the density and the mass-weighted mixing law for viscosity and thermal conductivity. The secondary phases: biomass, char and sand are all defined as granular phases with a particle diameter of 500 µm.

Fluid-solid drag interactions are accounted for using the Gidaspow model and solid-solid drag forces are modeled using the Syamlal-O'brein symmetric drag model [11, 12]. The Gunn correlation is used to calculate the heat exchange coefficient for fluid-solid interactions [13]. So far the description of the phase interactions corresponds to the polymer-air GSVR simulations of the previous chapter. Since more than one particulate phase is present in the fast biomass pyrolysis simulations, solid-solid heat transfer has to be accounted for. This heat transfer is assumed to consist mainly out of radiation, which can be implemented manually by a user-defined function for every particulate phase [2].

$$Q_i = \left[\frac{W}{m^3}\right] = \left(\frac{6}{d_p}\right) \cdot \frac{\epsilon \cdot \sigma}{\varepsilon_s} \sum_{solids} \varepsilon_k \left(T_k^4 - T_i^4\right) \tag{3.1}$$

Here, Q_i is the volumetric heat source term, d_p is the particle diameter (m), ϵ is the emissivity of the material which is assumed to be 0.75 for all particulate phases, the Stefan-Boltzmann constant σ equals $5.676 \times 10^{-8}\, W/m^2 \cdot K^4$, ε_s is the total solids volume fraction, and T is the absolute temperature in Kelvin. For example the expression for the biomass (b) source term in function of the char (c) and sand (s) temperature goes as follows:

$$Q_b = \left(\frac{6}{d_p}\right) \cdot \frac{\epsilon \cdot \sigma}{\varepsilon_b} \cdot \left[\varepsilon_c \left(T_c^4 - T_b^4\right) + \varepsilon_s \left(T_s^4 - T_b^4\right)\right] \tag{3.2}$$

After implementing these phase properties, the goal is to obtain a stable GSVR fast biomass pyrolysis simulation. This is done step-by-step in the next sections, taking into account the challenging aspects of these simulations including the multiple phases, the definition of solid-phase species, implementing appropriate user-defined functions to achieve continuous feeding, dealing with the radiation heat transfer, and the non-isothermal nature of the reactor.

3.3. Fast biomass pyrolysis simulations

3.3.1. Sand feeding

Initially only nitrogen is sent through the GSVR reactor jacket at a velocity of 1.433 m/s at 923 K which corresponds to a feeding rate of 0.113 kg/s using the ideal gas law. After 2.0 s when steady-state is reached, the sand phase is send through the reactor jacket for 1.0 s in order to reach a rotating sand bed of 2.0 kg in the reactor chamber. The sand phase is fed at 750 K with a volume fraction of 0.03534 and a velocity of 0.1 m/s. After the feeding step, again only nitrogen is sent through the reactor jacket to ensure that all the sand migrates to the reactor chamber and forms a stable bed.

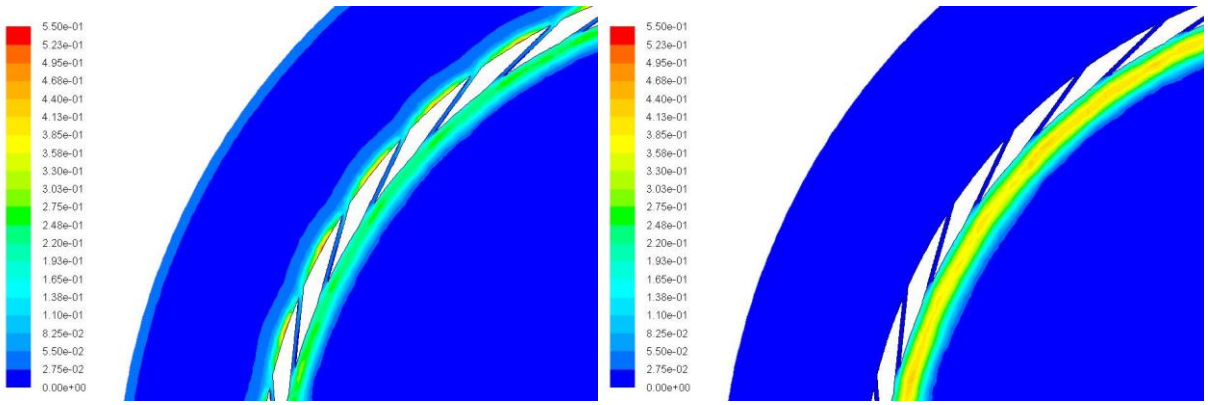

Figure 3-3: Contour plots of sand volume fraction at the end of the sand feeding step (left) and 2.0 s later when all the sand is in the reactor chamber (right).

This feeding process of sand is similar to the way polymer particles were fed in the previous cold flow chapter where the geometric parameters of the GSVR were varied. Volume fraction and feeding time of sand are different since the density of sand 2650 kg/m^3 is a multiple of the density of the polymer phase, which was assumed to be 950 kg/m^3, resulting in a shorter feeding time for a similar volume fraction in order to obtain the same reactor bed mass.

3.3.2. Biomass feeding

After obtaining a stable sand bed the biomass feeding is enabled. A user-defined function ensures that lignocellulosic biomass consisting of 36 wt% cellulose, 17 wt% hemicellulose and 47 wt% lignin, is fed homogeneously at 300 K in the reactor chamber at a radial distance between 0.25 and 0.255 m. The main reason why the biomass has to be fed differently from the sand is because the feeding of the biomass occurs continuously compared to the sand phase, which stays inside the reactor chamber during the entire simulation. Feeding the biomass through the reactor jacket, analogously to the sand feeding mechanism, would be unrealistic in practice taking the reaction kinetics into account, as the GSVR is designed to have the reactions occurring in the reaction chamber and not before the injection slots. During this feeding phase biomass is fed at a source rate of 0.03868 kg/s for 2.5 s. The resulting contour plots of sand and biomass are shown in Figure 3-4.

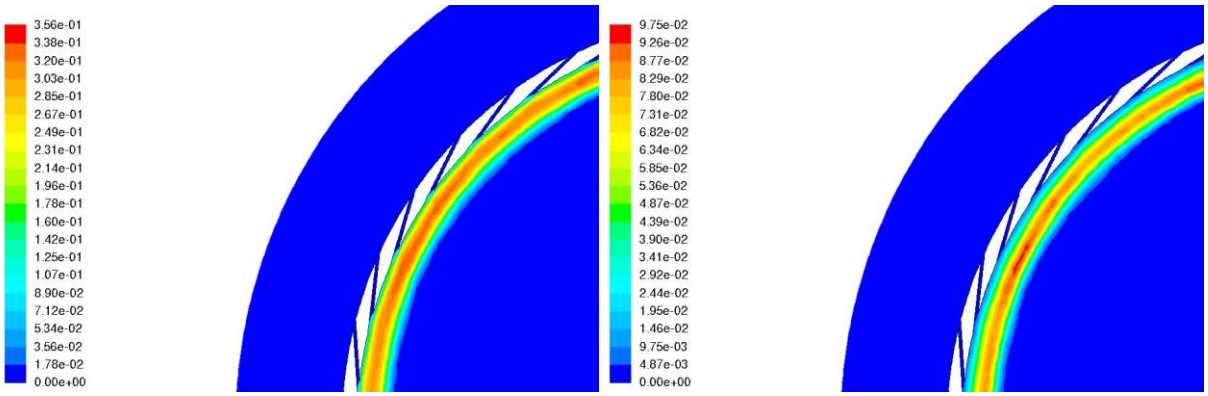

Figure 3-4: Contour plots of sand (left) and biomass (right) volume fractions after 2.5 s of biomass feeding.

In contrast to the simulations with the polymer phases, there is no azimuthal dependency of the sand and biomass bed. Taking a radial cross section of the GSVR gives a better visual representation of the solid beds as shown in Figure 3-5. Segregation of both phases is expected to occur but in this case both bed masses differ in order of magnitude, 96.70 g of biomass compared to 2.0 kg of sand.

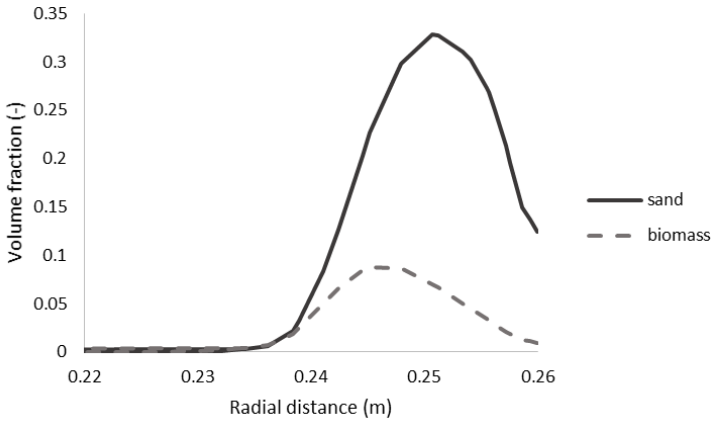

Figure 3-5: Volume fraction of sand and biomass in function of radial distance after 2.5 s of biomass feeding.

Sand is present as an inert heat transfer agent and will in break up biomass agglomerates in the reactor. In literature, fast biomass pyrolysis simulations have been performed with the absence of the sand phase. In this GSVR setup momentum of the gas phase is transferred from the gas phase to the sand bed in order to generate a stable rotating bed in the static geometry. Performing these simulations without the sand phase, gives gas velocities up to 155 m/s in the reactor chamber as shown in Figure 3-6.

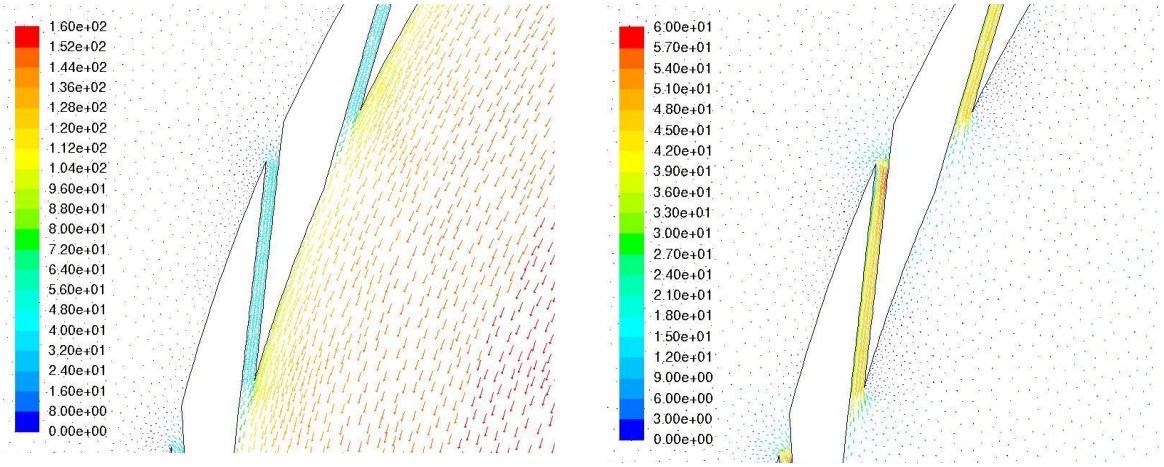

Figure 3-6: Velocity vectors of the gas phase for simulations without sand (left) and with sand inside the GSVR (right).

Injecting biomass particles inside these high velocity fields, will immediately destabilize the biomass bed, resulting in channeling and slugging. Reducing the gas velocity at reactor jacket inlet could be an alternative to get smaller Reynolds numbers inside the biomass bed, but this volumetric nitrogen flow rate is necessary is required to heat up the biomass entering at 300 K. These isolated biomass slugs as shown in Figure 3-7 were also observed in experimental setups during startup with not enough solids present to achieve a stable bed.

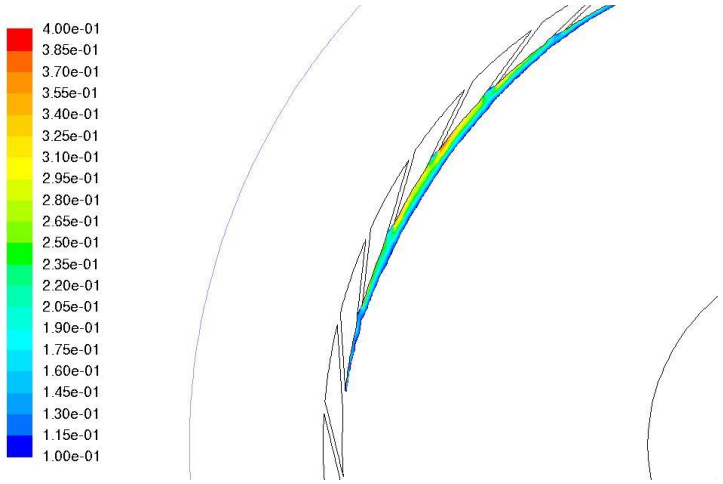

Figure 3-7: Contour of the biomass volume fraction after 1.0 s of feeding in the GSVR without the presence of sand.

One way to circumvent this biomass feeding problem in the absence of sand, is to feed the same mass of biomass as is done in the sand feeding stage. Since the density of sand is assumed to be 2650 kg/m^3 and the cellulose, hemicellulos and lignin density is 500 kg/m^3, this results an increased volumetric feeding rate with a factor five compared to the sand feeding.

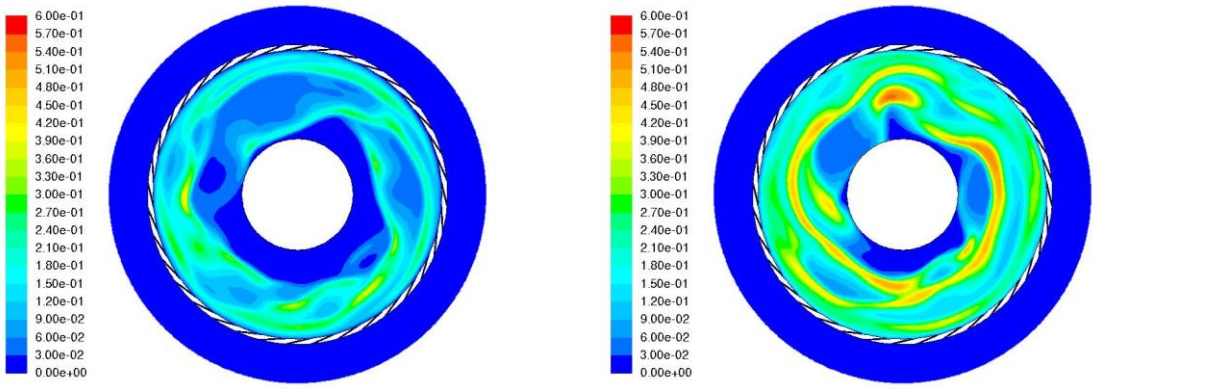

Figure 3-8: Contour plots of the biomass volume fraction in a GSVR without the presence of the sand bed at the end of the biomass feeding step for 1.0 kg of biomass (left) and 2.0 kg of biomass (right).

Figure 3-8 shows that there are still feeding problems when increasing the biomass feeding rate to rates comparable to the sand feeding rate of 2.0 kg/s. In the next step fast biomass pyrolysis reaction kinetics will be implemented on the stable biomass-sand bed simulations shown in Figure 3-5. However the problem of injecting this low density biomass phase inside a high velocity nitrogen field will be of importance for future work where the GSVR setup is going to be scaled down. Since nitrogen is expensive, a smaller GSVR geometry is being constructed at the LCT in order to perform fast biomass pyrolysis experiments. Experiments in this smaller geometry will be performed in the absence of sand. However the next simulations are performed with the sand phase being present in the GSVR in order to get results comparable with fluidized bed reactor simulations performed in scientific literature.

3.3.3. Reaction mechanism

After generating a stable sand bed and imposing a continuously growing polymer bed, the reaction kinetics can be implemented. Up until this point of the simulations, not only the biomass pyrolysis reaction was disabled but also solid-solid heat transfer was not taken into account and the feeding of the water vapor was ignored. The gas phase has an average temperature of 923 K corresponding to the feeding temperature and the sand phase is present at 750 K. Enabling the heat transfer mechanisms too soon generates an unstable bed. Since the goal of these simulations is to reach a stable solid bed, the reaction kinetics will be enabled once a stable biomass bed is formed.

Table 3-2: Pyrolysis reaction mechanism and related data [3, 8-10].

	Reaction	ΔH_{rxn} (kJ/kg)	A_f(1/s)	E_a (kJ/mol)
1a	$CL_v \rightarrow CL_a$	0	2.80×10^{19}	242.4
1b	$HC_v \rightarrow HC_a$	0	2.10×10^{16}	186.7
1c	$LG_v \rightarrow LG_a$	0	9.60×10^{8}	107.6
2a	$CL_a \rightarrow$ tar	255	3.28×10^{14}	196.5
2b	$HC_a \rightarrow$ tar	255	8.75×10^{15}	202.4
2c	$LG_a \rightarrow$ tar	255	1.50×10^{9}	143.8
3a	$CL_a \rightarrow 0.35\ char_c + 2.6$ Pgas	-20	1.30×10^{10}	150.5
3b	$HC_a \rightarrow 0.60\ char_h + 1.6$ Pgas	-20	2.60×10^{11}	145.7
3c	$LG_a \rightarrow 0.75\ char_l +$ Pgas	-20	7.70×10^{6}	111.4
4	tar $\rightarrow$ 4 Pgas	-42	4.25×10^{6}	108.0

In this secondary biomass feeding step, the biomass is assumed to be wet containing an additional 10 wt% of water, this will result in a water vapor feeding of 3.868 g/s analogously to the biomass feeding process. The reaction kinetics were enabled after 2.5 s of biomass feeding when a biomass bed of 0.0967 kg was formed inside the reactor chamber. Table 3-3 shows the bed mass of the different phases up to 3.0 s after implementing the reaction network, which corresponds to 8.0 s of simulation time.

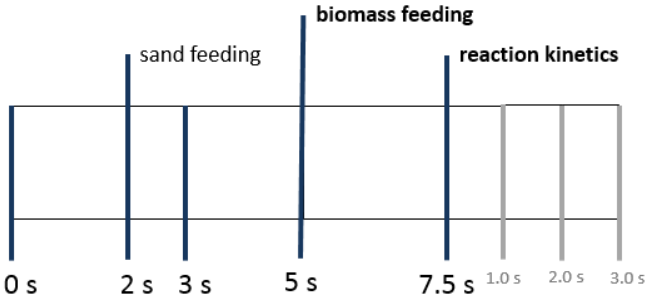

Figure 3-9: Timeline of the fast biomass pyrolysis simulations. The adjustments indicated in bold are from that step onwards, the sand feeding step lasted only one second.

The timeline shown in Figure 3-9 tends to give a better overview of the performed simulation. Once the reaction mechanism is enabled after 7.5 s of simulation time, data is taken each second to investigate the bed hydrodynamics in function of time. Figure 3-10 compares the volume fractions of the various solid phases in function of radial distance 1.0 s after the reaction kinetics were enabled with the data obtained by Ashcraft et al. The sand bed volume fraction is in the same order of magnitude, even though Ashcraft used a 5.0 kg sand bed during his simulations. After 1.0 s of fast biomass pyrolysis the char volume fraction is not in steady state and is expected to increase. The biomass volume fraction differs but is in the same order of magnitude compared to the larger sand volume fraction.

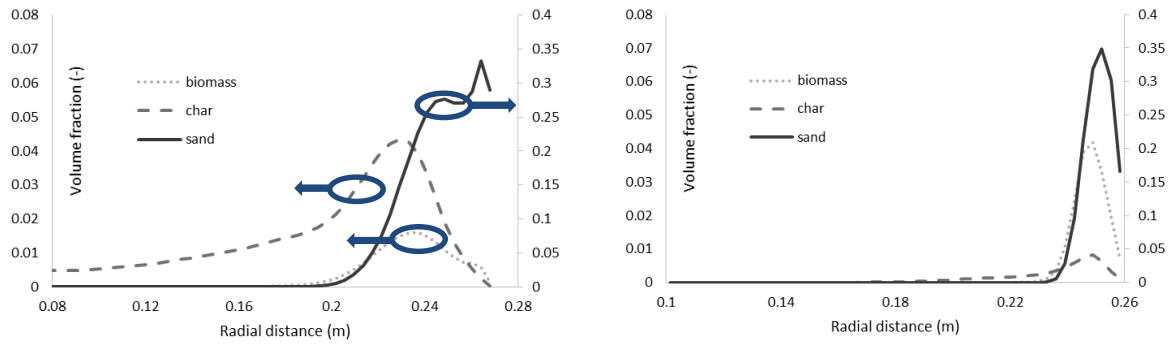

Figure 3-10: Bed volume fractions of the different solid phases of the simulation performed by R. Ashcraft (left) and of the described simulation 1.0 s after enabling the reaction mechanism.

The sand bed appears to be stable, but apparently the biomass bed increases. A more quantitative representation of this increase of biomass and char bed is shown in Table 3-3.

Table 3-3: Char, biomass and sand bed mass inside the GSVR 1.0, 2.0 and 3.0 s after enabling the reaction mechanism.

	1.0 s	2.0 s	3.0 s
char	9.71 g	12.44 g	15.55 g
biomass	45.49 g	58.74 g	72.87 g
sand	2.0 kg	2.0 kg	2.0 kg

The increase of biomass bed mass can be explained by looking at Figure 3-11. Up to this point, no attention has been paid to the temperature profiles of the various phases in the reactor chamber. Biomass is fed at 300 K and gas is fed at 923 K, a heat balance can be set up over the reactor as shown in Appendix G. Nitrogen is the only source of heat, which has to heat up the wet biomass phase to fast biomass pyrolysis process temperatures. Setting up the heat balance with the given wet biomass inlet conditions, nitrogen inlet conditions and reaction enthalpies results in a positive enthalpy balance, which allows for a decrease of the temperature of the solid phases in time as shown in Figure 3-11.

This heat balance will only be used to get an idea of the order of magnitude of the nitrogen inlet flow rate required to provide enough heating to enable the endothermic process. A more detailed study of the reaction network is necessary to calculate the product selectivities, fortunately most of the supplied heat is used to heat up the wet biomass. This implies that the heat required for the endothermic reaction has a minor contribution to the heat balance.

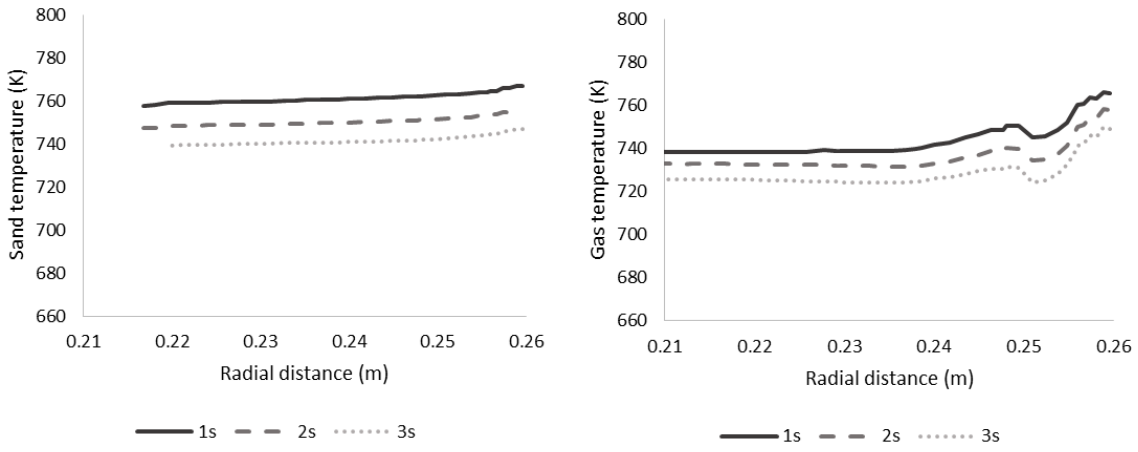

Figure 3-11: Sand (left) and gas (right) temperature in function of radial distance at various time steps after enabling the reaction mechanism.

There are two ways to increase the reactor temperature to the appropriate temperature range for fast biomass pyrolysis. One possibility is to increase the nitrogen inlet temperature, this is the most straightforward way to control the bed temperature during computational fluid dynamic simulations but is more difficult to monitor in an experimental setup. The second possibility consists of increasing the nitrogen flow rate, , a disadvantage of this adjustment is that rapidly increasing the volumetric flow rate might destabilize the reactor bed. In this case there was opted to increase the nitrogen gas flow rate. Setting up an energy balance yielded that equilibrium was obtained when feeding 2.73 m/s of nitrogen through the reactor jacked instead of the initial 1.433 m/s.

However, the reactor temperature doesn't only have to be in steady state, the reactor has to be heated up to the initial temperatures suitable for fast biomass pyrolysis. In order to heat the entire bed up, the heat capacities, the initial temperatures and the bed mass of the sand, biomass and char in the reactor chamber were necessary to calculate how much energy was needed to heat up the reactor.

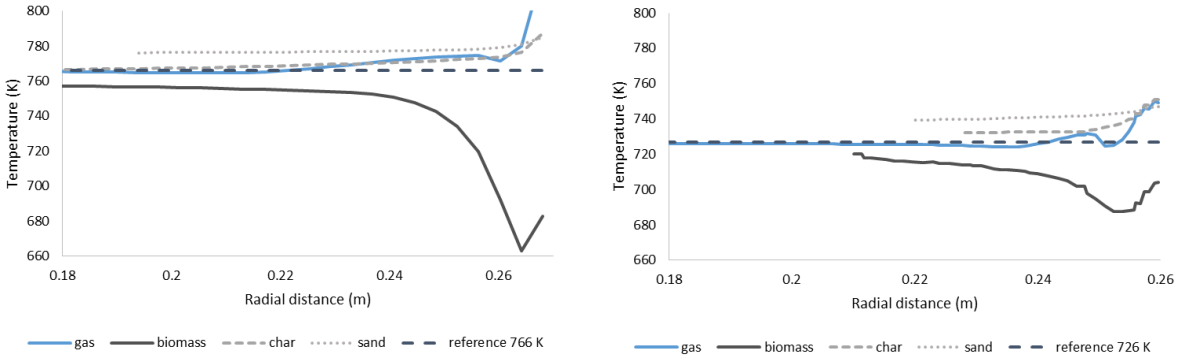

Figure 3-12: Temperature profiles inside the reactor chamber for R. Ashcraft's simulations (left) and after 3.0 s of reaction for the described simulation (right).

Figure 3-12 shows that the reactor temperatures are indeed too low to have an industrially feasible fast biomass pyrolysis process. The gas outlet temperature was added as a reference point in order to visualize the difference in operating temperatures. These low operating temperatures were the reason for the low reaction rates resulting in increasing biomass concentration in the reactor bed. Increasing the nitrogen inlet flow rate ensures that sufficient heat is supplied to stabilize the reactor temperatures and prevents a further temperature drop. Biomass temperatures ranging from 720 K to 770 K are optimal for tar production by fast pyrolysis. As shown on the left side of Figure 3-12 the biomass temperature is below 720 K for the entire biomass bed, in the simulations performed by Ashcraft biomass particles are heated up to temperatures above 750 K. The biomass bed will need to be heated up in a next step.

In order to get an overview of the performed fast biomass pyrolysis simulation inside the GSVR the timeline previously shown in Figure 3-9 was updated to visualize the various simulation steps. For the first two seconds only nitrogen was sent inside the GSVR at 923 K and with jacket inlet velocity of 1.433 m/s. When steady state was reached, sand was fed at 750 K for one second to get a 2.0 kg sand bed inside the reactor chamber. After 3.0 s only nitrogen was fed through the reactor jacket to stabilize the sand bed until steady state was reached. At 5.0 s the biomass feeding started and after 2.5 s, when a biomass bed was formed inside the GSVR the reaction kinetics were switched on. However since the temperature dropped inside the GSVR starting from 7.5s, more heat had to be supplied to counteract this drop in temperature this was done starting from 11.0 s. Afterwards at 13.0 s when the temperature profile was stabilized, the reactor had to be heated up to temperatures between 450 and 500 °C suitable for fast biomass pyrolysis. This temperature increase was done by increasing the nitrogen inlet temperature by 100 °C for 2.0 s, this temperature increase can be validated by checking the energy balance. The next paragraphs will focus on stabilizing the reactor bed temperature by increasing the net volumetric gas flow rate and the nitrogen inlet temperature.

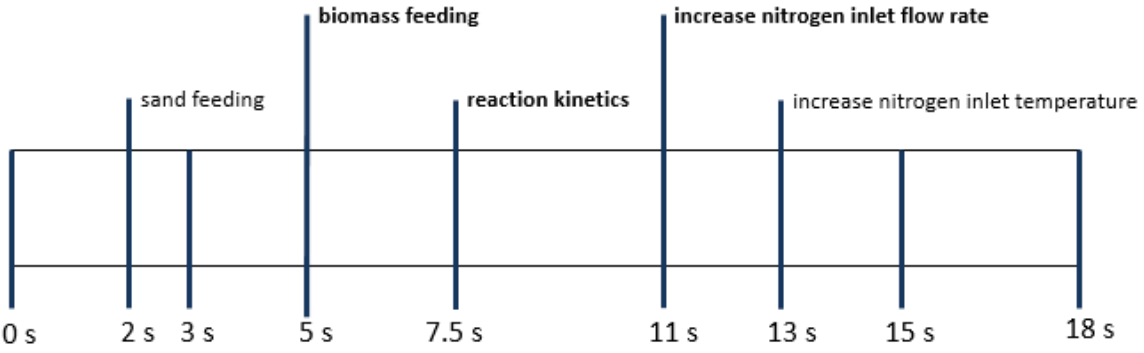

Figure 3-13: Timeline of the fast biomass pyrolysis simulations. The adjustments indicated in bold are from that step onwards, the sand feeding and nitrogen inlet temperature increase were only applied for a specified time period.

Increase nitrogen inlet flow rate

After 11.0 s the nitrogen inlet flow was increased from 1.433 m/s to 2.73 m/s to prevent further reactor temperature drop. To maintain a stable solid bed the volumetric nitrogen inlet feed was increased stepwise in three steps each after 0.1 s. Figure 3-14 shows that further temperature drop of the solid bed is prevented by an increase in nitrogen flow rate. To visualize the differences in operating temperatures the gas outlet temperature was again added as a reference.

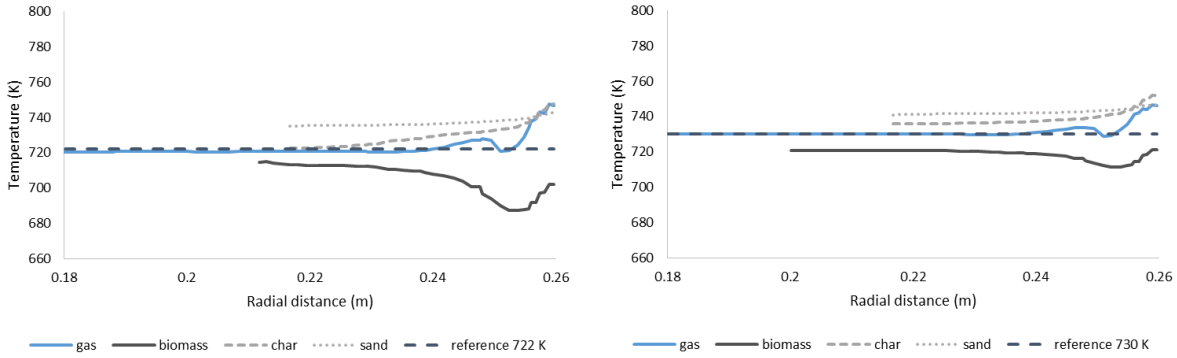

Figure 3-14: Temperature profiles inside the reactor chamber after 11.0 s (left) and after increasing the nitrogen flow rate for 2.0 s (right).

Increase nitrogen inlet temperature

Increasing the nitrogen inlet temperature to 1023 K for 2.0 s will increase the reactor bed temperature. Afterwards the feeding temperature is again reduced to the initial feeding temperature of 923 K. It can be observed that after 18.0 s the reactor is finally operating at temperatures between 450 and 500 °C.

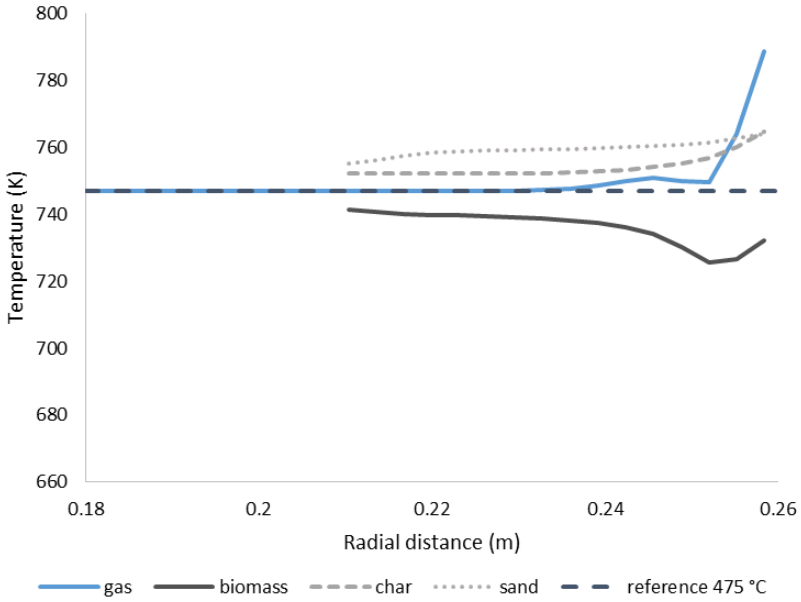

Figure 3-15: Temperature profiles inside the reactor chamber after 18.0 s after the reactor bed is heated up to temperatures around 750 K.

These operating temperatures are related to the reaction rates shown in Figure 3-16. Activation occurs at the beginning of the biomass bed closest to the injection slots and the biomass conversion occurs deeper inside the reactor. Secondary tar cracking is negligible and occurs even deeper inside the reactor chamber, this can be seen by plotting the reaction rate on a logarithmic scale.

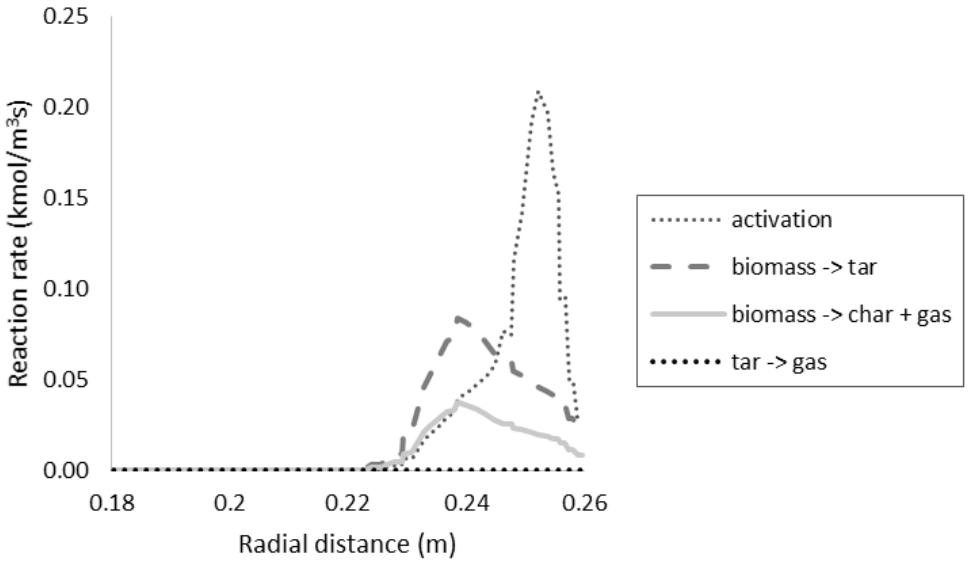

Figure 3-16: Reaction rates for the various steps in the reaction mechanism.

After 18.0 s the conversion of the dry biomass phase can be calculated by monitoring the reactor outlet. The pyrolysis gas and the main product tar leave the reactor outlet, in contrast with the char particles and unreacted biomass which both accumulate in the fluidized bed. The formation rate of char was determined by monitoring the increase of char bed mass over the entire reactor. Table 3-4 gives the product distribution in function of fed biomass after 18.0 s of simulation time.

Table 3-4: Product distribution in function of fed biomass, the results are averaged over 2.0 s in order to average out the minor oscillatory bed behavior.

	wt%
pyro gas	8.95 ± 0.07
tar	66.85 ± 0.64
biomass	3.21 ± 0.36
char	20.24 ± 0.07

Table 3-5 shows the accumulative behavior of both the biomass and the sand phase:

Table 3-5: Char, biomass and sand bed mass inside the GSVR after 18.0 and 20.0 s of simulation.

	18.0 s	20.0 s
char	63.00 g	78.63 g
biomass	101.69 g	104.36 g
sand	2.0 kg	2.0 kg

Figure 3-17 shows contour plots of the volume fractions of the three different solid phases present in the vortex reactor. The biomass conversion depends on the composition of the fed biomass. The bed dynamics do not depend on the biomass composition since density and viscosity are the same for all biomass components.

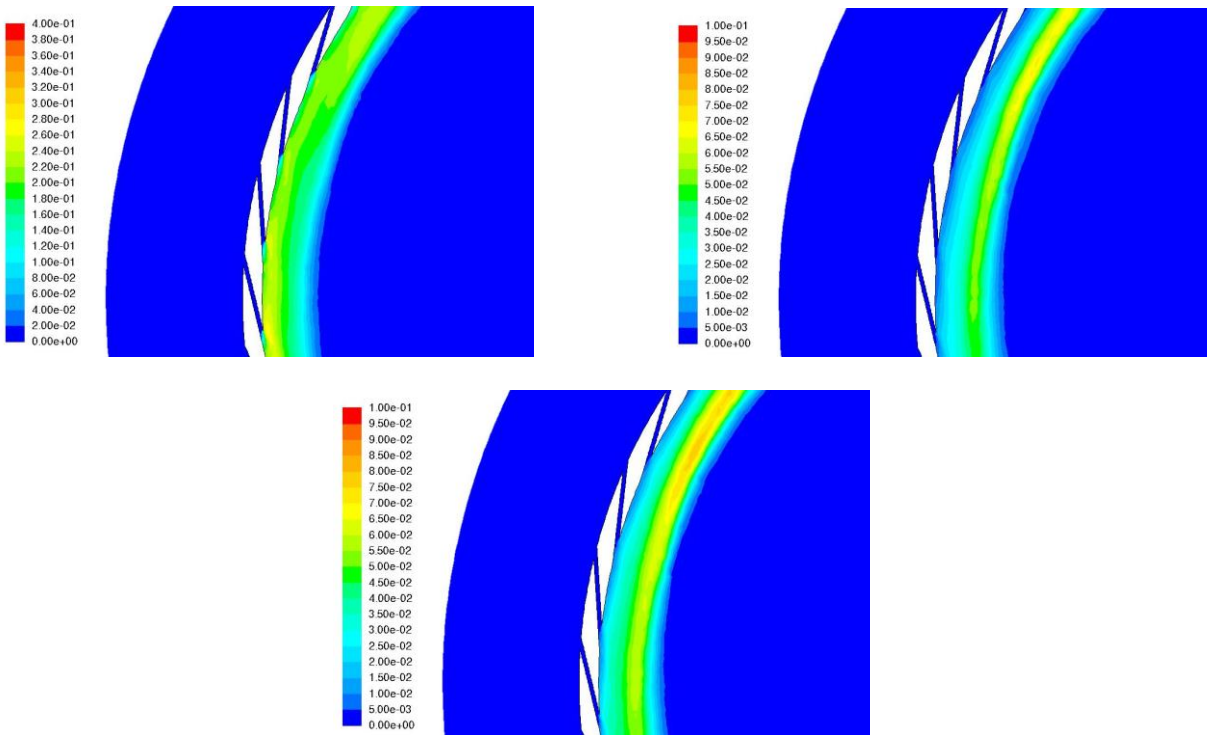

Figure 3-17: Contour plots of sand (upper left), biomass (middle down) and char (upper right) volume fractions inside the GSVR after 18.0 s of simulation.

R. Ashcraft used a biomass composition of 36 wt% cellulose, 47 wt% hemicellulose and 17 wt% lignin [2] which corresponds to the composition of bagasse previously used for fast biomass pyrolysis simulations in a fluidized-bed riser-reactor by Fox et al. [3, 14]. Changing the biomass feed to the same composition gives after reaching steady state:

Table 3-6: Reaction products in weight percentage of the fed biomass for the performed simulations in comparison with scientific literature.

	Simulation	R. Ashcraft	Fox
pyro gas	9.91 ± 0.01 wt%	9.5 wt%	21.5 wt%
tar	73.17 ± 0.05 wt%	73.8 wt%	63.4 wt%
char	16.9 ± 0.06 wt%	16.1 wt%	14.4 wt%

In literature there is an incentive to shift to other biomass materials for example red oak or switchgrass with compositions given in Table 3-7. In order to be able to more quantitatively compare conversions simulations should be performed with pure cellulose

Table 3-7: Possible biomass compositions in weight percentage.

	Pure cellulose	Bagasse	Switchgrass	Red oak
Cellulose	100.0 wt%	36.0 wt%	42.0 wt%	41.0 wt%
Hemicellulose	0.0 wt%	47.0 wt%	34.0 wt%	32.0 wt%
Lignin	0.0 wt%	17.0 wt%	24.0 wt%	27.0 wt%

3.3.4. Discussion of the fast biomass pyrolysis simulations

Even when continuing the simulations for an extended time period, the char phase remains trapped in the reactor chamber. This accumulation of char over time is contrary to the claim that char would leave the vortex reactor through the central exhaust entrained in the gas phase. This char phase behavior would be a benefit of the GSVR for fast biomass pyrolysis compared to the classical riser reactors since reducing the char residence time in the reactor will prevent unnecessary secondary reactions to set in. The modeling limitation in this specific setup is the constant char diameter used for the char phase. Granular phases are defined in Fluent with a constant particle diameter, in contrast to reality where the biomass particles will gradually be reduced to a char particle, shrinking in diameter until the particles are small enough to leave the reactor with the gas phase. Taking this particle shrinkage into account during the simulations would mean an implementation of other Eulerian phases.

Char particle diameter of 100 µm

The char particle diameter will however in the next simulations be reduced to 100 µm, in reality a distribution of char particle diameters will be encountered. Figure 3-18 show the biomass and char bed mass for a fast biomass pyrolysis simulation in a GSVR. The reaction mechanism is enabled 2.5 s after the biomass feeding has started. Analogously to the previous simulations a stable sand bed was established before the biomass feeding step.

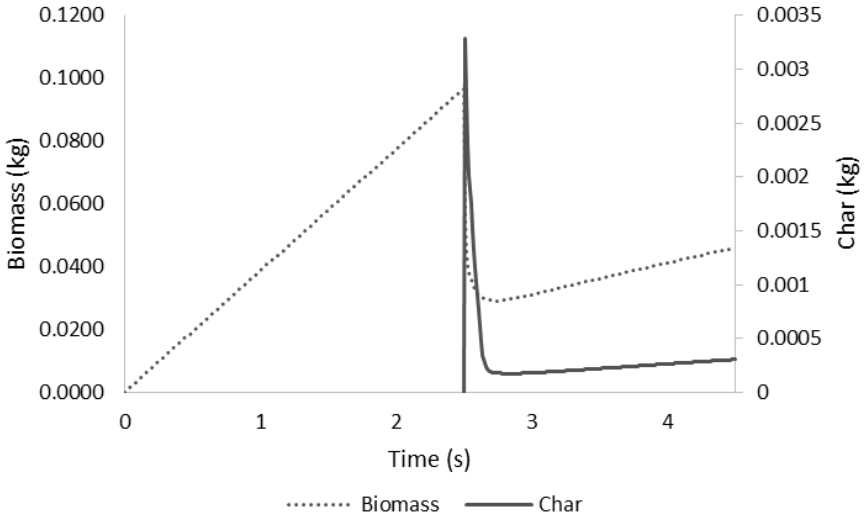

Figure 3-18: Biomass and char bed mass in the GSVR in function of time. The reaction mechanism is enabled after 2.5 s of simulation.

Figure 3-18 shows that the char bed mass is negligible, this compared to the previous simulation where already a 10 g char bed was formed after 2.5 s of reaction. It has to be noted that the nitrogen feeding rate is different for both cases, but the focus of Figure 3-19 is on the behavior of the char phase. The char phase can be seen leaving the reactor entrained in the gas phase.

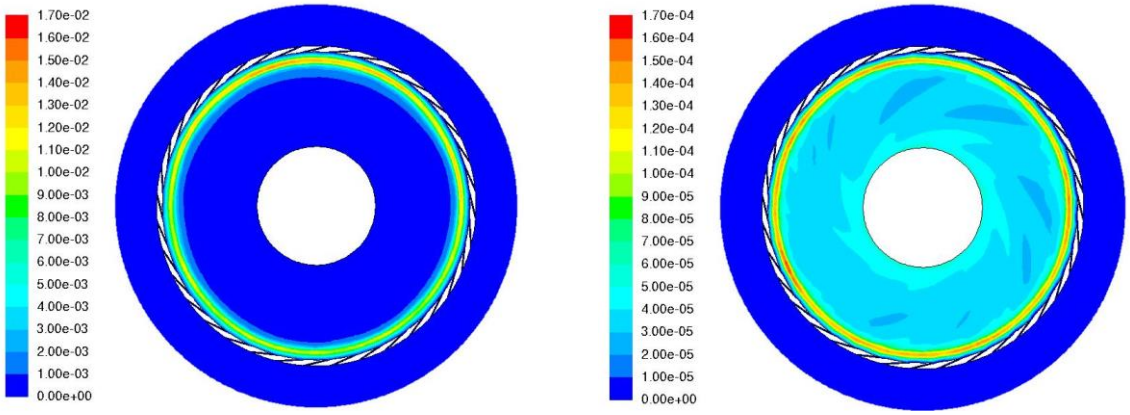

Figure 3-19: Contours of volume fraction of the char phase in the original simulation (left) and for char diameter reduced to 100 µm (right) both taken 1.5 s after enabling the reaction mechanism.

Another way of describing the difference in char behaviour is shown in Figure 3-20, compared to previous simulations, the char particles leave the reactor through the outlet.

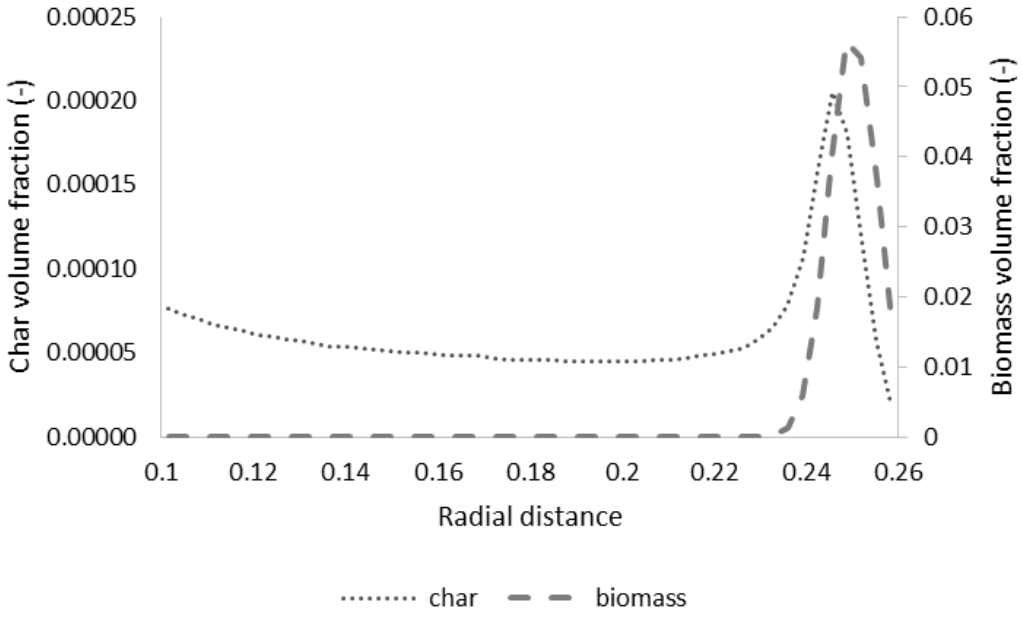

Figure 3-20: Char and biomass volume fractions in function of radial distance 3.5 s after enabling the reaction mechanism.

Particle diameters of 100 µm are on the edge of the surface to volume ratio where Van der Waals forces have to be taken into account [15]. Van der Waals forces should definitely be taken into account for particle diameters smaller than 100 µm. Fluent relies on user-defined functions to calculate Van der Waals forces, the previous simulation was performed without taking these forces into consideration. Implementing Van der Waals forces in Fluent will require additional assumptions, modeling particle attraction inversely proportional to the distance between them would only partially cover the problem. In order to avoid dealing with Van der Waals forces the was opted for char particle diameters of 100 µm.

Comparison to 40° GSVR section

In the results of R. Ashcraft the char particles of 500 µm were reported to leave the reactor. This conclusion might have been a result of the geometry used for the simulations. Ashcraft used a 40° section of the GSVR with periodic boundary conditions to describe the fast biomass pyrolysis process. The setup is assumed to be periodic but instabilities leading to slugging might occur when using the 40° section, in comparison with the 360° section where oscillatory behavior is damped out.

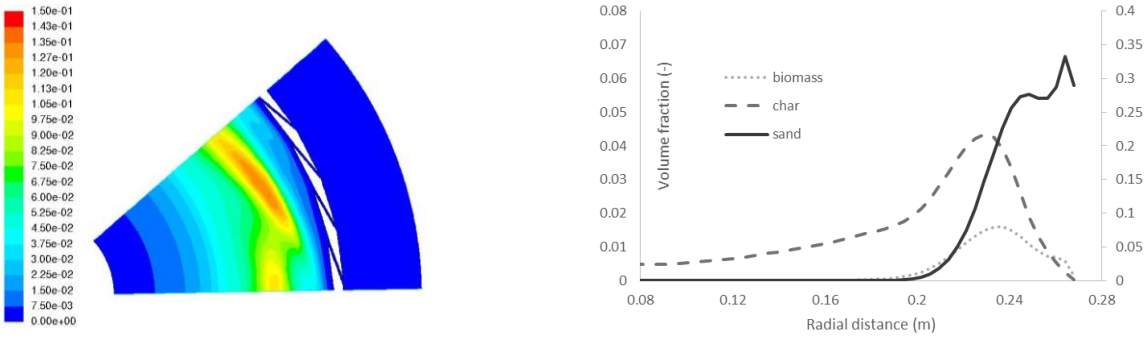

Figure 3-21: Contour plot of the volume fraction of the char phase (left) and volume fractions in function of radial distance for the granular phases (right).

Because of the solid bed showing oscillatory behavior, the solid volume fractions shown on the right side of Figure 3-21 are averaged out over 5.0 s. This bed dynamic could push the char particles to the outlet.

3.4. Future work

3.4.1. Scale down

An experimental GSVR setup is currently being built at the LCT. Because nitrogen is expensive, the entire setup will be scaled down compared to the cold flow gas-solid vortex unit. The performed CFD simulations confirm the claim that fast biomass pyrolysis is feasible compared to traditional technologies. However experimental results are required to validate the computational simulations. The CFD fast biomass pyrolysis simulations should also be repeated for the smaller experimental geometry in order to get a better quantitative comparison.

3.4.2. Gas density model

During the initial simulations the gas phase was modeled using the incompressible ideal gas law. In order to more accurately describe heat transfer phenomena ANSYS Fluent is able to define density using the compressible ideal gas law. For the standard ideal gas law the solver will compute the density for an incompressible flow as:

$$\rho = \frac{p_{op}}{\frac{R}{M_W}T} \tag{3.3}$$

In this form the density depends only on the operating pressure, p_{op}. Taking the local relative pressures into account for the GSVR calculations of the gas phase density should result in a temperature drop related to a pressure drop after the injection slots.

In further simulations, a more elaborate study on the pressure profiles during the fast biomass pyrolysis inside the GSVR might be meaningful to conduct since some of the elementary steps in the reaction mechanism are pressure dependent.

3.5. Conclusion

In this chapter a reactive CFD simulation of fast biomass pyrolysis in a gas-solid vortex reactor was modeled. The high tar yield of 73.2 wt% confirms the claim that the gas-solid vortex reactor offers process intensification possibilities compared to classical riser reactors where only 63.4 wt% of the fed bagasse is converted to the desired tar product. The simulations were performed by feeding the particulate sand phase once a steady-state gas profile was obtained in the reactor chamber. In a next step biomass was fed homogeneously inside the reactor chamber at radial values between 0.25 and 0.255 m. Once the reaction kinetics were enabled, the nitrogen feeding rate had to be adjusted in order to supply enough heat to enable the endothermic reaction mechanism and to heat up the biomass from room temperature to temperatures suitable for fast biomass pyrolysis.

Char was reported to stay in the reactor chamber. However this is undesired, in reality it is to be expected that the char will leave the reactor through the outlet entrained in the gas phase. To account for this experimentally expected behavior, the model was adjusted by reducing the char particle diameter from 500 µm to 100 µm. For these particle sizes Van de Waals forces should just be avoided. Comparing the 360° simulations to the previously performed 40° simulations, gives some interesting differences. The solid bed shows oscillatory behavior for the 40° simulations, since this is not the case for the 360° geometry simulations, it might be that the complete geometry damps out turbulent behavior. Where the periodicity of the 40° section enforces minor disturbances.

3.6. Bibliography

1. Bridgwater, A.V. and G.V.C. Peacocke, *Fast pyrolysis processes for biomass.* Renewable & Sustainable Energy Reviews, 2000. **4**(1): p. 1-73.
2. Ashcraft, R.W., G.J. Heynderickx, and G.B. Marin, *Modeling fast biomass pyrolysis in a gas-solid vortex reactor.* Chemical Engineering Journal, 2012. **207**: p. 195-208.
3. Xue, Q., T.J. Heindel, and R. Fox, *A CFD model for biomass fast pyrolysis in fluidized-bed reactors.* Chemical Engineering Science, 2011. **66**(11): p. 2440-2452.
4. Shafizadeh, F., *INTRODUCTION TO PYROLYSIS OF BIOMASS.* Journal of Analytical and Applied Pyrolysis, 1982. **3**(4): p. 283-305.
5. Carmichael, L. and B. Sage, *Viscosity and thermal conductivity of nitrogen—n-heptane and nitrogen—n-octane mixtures.* AIChE Journal, 1966. **12**(3): p. 559-562.
6. Vogel, E. and A.-K. Neumann, *Vapor-phase viscosity of phenol.* International journal of thermophysics, 1993. **14**(4): p. 805-818.
7. Yaws, C., *Chemical Properties Handbook: Physical, Thermodynamics, Environmental Transport, Safety & Health Related Properties for Organic &*. 1999: McGraw-Hill Professional.
8. Bradbury, A.G.W., Y. Sakai, and F. Shafizadeh, *A kinetic model for pyrolysis of cellulose.* Journal of Applied Polymer Science, 1979. **23**(11): p. 3271-3280.
9. Liden, A., F. Berruti, and D. Scott, *A kinetic model for the production of liquids from the flash pyrolysis of biomass.* Chemical Engineering Communications, 1988. **65**(1): p. 207-221.
10. Miller, R. and J. Bellan, *A generalized biomass pyrolysis model based on superimposed cellulose, hemicelluloseand liqnin kinetics.* Combustion science and technology, 1997. **126**(1-6): p. 97-137.
11. Gidaspow, D., R. Bezburuah, and J. Ding, *Hydrodynamics of circulating fluidized beds: Kinetic theory approach*. 1991. Medium: ED; Size: Pages: (8 p).
12. Syamlal, M., W. Rogers, and T.J. O'Brien, *MFIX documentation: Theory guide.* National Energy Technology Laboratory, Department of Energy, Technical Note DOE/METC-95/1013 and NTIS/DE95000031, 1993.
13. Papadikis, K., et al., *Application of CFD to model fast pyrolysis of biomass.* Fuel Processing Technology, 2009. **90**(4): p. 504-512.
14. Lathouwers, D. and J. Bellan, *Modeling of dense gas–solid reactive mixtures applied to biomass pyrolysis in a fluidized bed.* International Journal of Multiphase Flow, 2001. **27**(12): p. 2155-2187.
15. Parsegian, V.A., *Van der Waals Forces: A Handbook for Biologists, Chemists, Engineers, and Physicists*. 2005: Cambridge University Press.

Chapter 4: Conclusions and Future Work

4.1. Conclusions

A literature study is performed comparing the gas solid vortex reactor to gravitational fluidized bed reactors. The gas solid vortex reactor shows promising characteristics for various processes including fast biomass pyrolysis because of the high gas-solid slip velocities inside the fluidized bed, resulting in high heat transfer coefficients, and the short gas phase residence times. Other biomass conversion processes have been reviewed, with the emphasis on fast biomass pyrolysis since it is one of the most energy efficient biomass conversion processes.

The main disadvantage of the gas solid vortex reactor compared to other rotating bed reactors is that the gas flow rate and the rotational velocity of the bed cannot be controlled independently, however geometric adjustments can be made in the reactor design particularly changing the injection slot thickness and the injection slot angle, which will influence the velocity field inside the reactor chamber. In experimental setups fluidizing gas is expensive, this is an excellent incentive to look closer into the bed hydrodynamics for various geometries with a fixed volumetric gas flow rate. Numerical cold flow simulations inside a gas solid vortex reactor are performed for varying injection slot thicknesses and varying injection slot angles to investigate how the azimuthal momentum and gas-solid slip velocities can be increased by changing only geometric parameters. Reducing the injection slot angle and reducing the injection slot thickness appears to result in an increased azimuthal velocity, maintaining the same volumetric gas mass flow rate through the GSVR jacket. However this increase in azimuthal velocity is less pronounced for reducing the in the injection slot angle compared to reducing the injection slot thickness. These more strict geometric specifications have the disadvantage that a more tangential injection slot angle and a smaller injection slot thickness are more difficult to construct in an experimental setup. Additionally these geometries result in a higher pressure drop over the injection slots which results in feeding problems for too small injection slots. For the fast biomass pyrolysis simulations a compromise has to be made between the pressure drop and the gas-solid slip velocities in the vortex reactor.

Numerical simulations of a fast biomass pyrolysis process are performed in a 360° vortex reactor geometry. A stable solid bed is obtained with a product distribution around 76 wt% tar, 16 wt% char and 9 wt% pyrolysis gas, which is higher than the tar yield obtained in gravitational reactors. Compared to 40° sectional simulations in a GSVR performed by Ashcraft et al. no oscillatory behavior of the bed is observed. Henceforth it is advised to work with a 360° section especially for reactive flow. Another advantage of the GSVR over gravitational fluidized bed reactors is that the byproduct char can leave the reactor through the exhaust entrained in the gas phase. In the numerical simulations performed char was initially reported to stay inside the reactor chamber. To account for the experimentally expected char behavior, the model is adjusted by reducing the char particle diameter from 500 µm to 100 µm, which results in simulations where char leaves the reactor.

4.2. Future work

Two phase cold flow numerical simulations will have to be performed and compared to experimental results in order to better understand the hydrodynamics between two solid phases. Segregation phenomena and a different solid packing is expected to occur with two solid phases being present in the gas-solid vortex reactor. A better understanding of these cold flow interactions between the two solid phases will give more insight in reactive simulations where is solid phase is produced.

With the computational fluid dynamic simulations performed for fast biomass pyrolysis in a gas-solid vortex reactor, the next step is to verify these simulations by performing experiments in an experimental setup. At the LCT an experimental setup is currently being built for testing reactive flow in the geometry such as biomass pyrolysis and oxidative coupling of methane. The developed computational model can be scaled down and be used for further investigation of experimental data. Unlike experimental data the numerical simulations can be instrusive in nature and more accurately describe the physical process.

The global devolatilization scheme that has been used to simulate the fast biomass pyrolysis reaction scheme can also be improved to better describe the fast biomass pyrolysis process. Although this scheme is the most extensively used biomass pyrolysis reaction scheme throughout the scientific literature, improvements can be made to the lumped reactants and products connected via these several simplified elementary reactions. Especially to account for the reaction from activated biomass to char and particle shrinkage effects more elaborate kinetics are required.

In the numerical fast biomass pyrolysis simulations, the influence of the inert nitrogen will need to be further investigated. There are two aspects to the nitrogen feeding: the fed nitrogen is used to impart azimuthal momentum resulting in a stable rotating bed and the nitrogen is also required to heat up the fed biomass. A more elaborate study will need to point out the minimum amount of nitrogen required to have a stable bed at sufficiently high temperatures for fast biomass pyrolysis. This minimum required nitrogen feeding will be most economically feasible for the experimental setup.

Appendix

Table of Contents

Appendix A: Performed simulations

Geometric study

Files\Cold_Flow_Simulations\GSVR_10dgr_1.0mm

Files\Cold_Flow_Simulations\GSVR_10dgr_1.5mm

Files\Cold_Flow_Simulations\GSVR_10dgr_2.0mm

Files\Cold_Flow_Simulations\GSVR_15dgr_1.0mm

Files\Cold_Flow_Simulations\GSVR_15dgr_1.5mm

Files\Cold_Flow_Simulations\GSVR_15dgr_1.5mm

Files\Cold_Flow_Simulations\GSVR_15dgr_2.0mm

Files\Cold_Flow_Simulations\GSVR_20dgr_1.0mm

Files\Cold_Flow_Simulations\GSVR_20dgr_1.5mm

Files\Cold_Flow_Simulations\GSVR_20dgr_2.0mm

Files\Cold_Flow_Simulations\GSVR_20dgr_2.5mm

Fast Biomass Pyrolysis

Files\Fast_Biomass_Pyrolysis\Reaction

Files\Fast_Biomass_Pyrolysis\Bagasse

Files\Fast_Biomass_Pyrolysis\ReducedCharDiameter

Appendix B: Journal files geometric study

```
solve/set/flow-warnings? no
solve/set/limiter-warnings? no

/* gas only for 2.0 s until steady state is reached */
define/boundary-conditions/velocity-inlet inlet polymer no no yes yes no 0 no no no yes 5 0.1
no 0.0001 no 0
solve/iterate 1
solve/dual-time-iterate 2000 40
file/write-data gsvr_gasfeedend.dat yes

/* polymer feeding for 2.5 s */
define/boundary-conditions/velocity-inlet inlet polymer no no yes yes no 0.1 no no no yes 5
0.1 no 0.0001 no 0.03942
solve/dual-time-iterate 2500 40
file/write-data gsvr_polymerfeedend.dat yes

/* gas only for 3.5 s to get a stable polymer bed inside the GSVR */
define/boundary-conditions/velocity-inlet inlet polymer no no yes yes no 0 no no no yes 5 0.1
no 0.0001 no 0
solve/dual-time-iterate 3500 40
file/write-data gsvr_simulationend.dat yes
```

Appendix C: Properties CFD simulation geometric study

FLUENT

Version: 2d, dp, pbns, eulerian, spe, rke, transient (2d, double precision, pressure-based, Eulerian, species, realizable k-epsilon, transient)
Release: 15.0.0
Title:
Models

Model Settings

Space	2D
Time	Unsteady, 1st-Order Implicit
Viscous Realizable	k-epsilon turbulence model
Wall Treatment	Standard Wall Functions
Multiphase	k-epsilon Models k-epsilon Model for Each Phase
Heat Transfer	Disabled
Solidification and Melting	Disabled
Radiation	None
Species	Non-Reacting
Coupled Dispersed Phase	Disabled
NOx Pollutants	Disabled
SOx Pollutants	Disabled
Soot	Disabled
Mercury	Pollutants Disabled

GAS PHASE

Material: (air) (fluid)

Property	Units	Method	Value(s)
Density	kg/m3	constant	1.225
Viscosity	kg/m-s	constant	1.7894e-05

POLYMER PHASE

Material: (polymer) (fluid)

Property	Units	Method	Value(s)
Density	kg/m3	constant	950
Viscosity	kg/m-s	constant	1.7894e-05

Appendix D: Journal files fast biomass pyrolysis

```
solve/set/flow-warnings? no
solve/set/limiter-warnings? no
define/user-defined/user-defined-memory 6
define/user-defined/execute "udm_rename6::libudf"
file/confirm-overwrite y

/* gas only for 2.0 s until steady state is reached */
/solve/initialize/initialize-flow ok
/solve/iterate 1
/solve/dual-time-iterate 2000 40

/* sand feeding for 1.0 s */
/define/boundary-conditions/velocity-inlet inlet sand no no yes yes no 0.1 no 750 no no no yes
5 0.1 no 0.0001 no 0.03534
/solve/dual-time-iterate 1000 40

/* gas only for 2.0 s to get a stable sand bed inside the GSVR */
/define/boundary-conditions/velocity-inlet inlet sand no no yes yes no 0 no 750 no no no yes 5
0.1 no 0.0001 no 0
/solve/dual-time-iterate 2000 40
file/write-data endsandfeeding.dat


/* dry biomass feeding for 2.5 s to get a biomass bed in the GSVR */
/define/boundary-conditions/fluid surface_body biomass yes 1 no yes "biomass_total::libudf" 0
0 0 0 1 no no 1 no yes "lign_feed::libudf" 1 no no 1 no yes "hemi_feed::libudf" 1 no no 0 no
no 0 no 0 no no no
/solve/dual-time-iterate 2500 40
file/write-data endbiomassfeeding.dat

/* enable radiative heat transfer and shift to wet biomass */
/define/boundary-conditions/fluid surface_body biomass yes 1 no yes "biomass_total::libudf" 0
0 0 0 1 no no 1 no yes "hemi_feed::libudf" 1 no no 1 no yes "lign_feed::libudf" 1 no no 2 no
yes "heat_rad_biomass::libudf" no yes "heat_gen::libudf" no no 0 no 0 no no no
/define/boundary-conditions/fluid surface_body gas-phase yes 0 0 0 0 0 1 no yes
"water_feed_gas::libudf" 0 0 1 no yes "heat_gen_gas::libudf" no no 0 no 0 no no no
/define/boundary-conditions/fluid surface_body sand yes 0 0 0 0 0 1 no yes
"heat_rad_sand::libudf" no no 0 no 0 no no no
/define/boundary-conditions/fluid surface_body char yes 0 0 0 0 0 0 0 1 no yes
"heat_rad_char::libudf" no no 0 no 0 no no no

/* enable reaction kinetics */
/define/phases/interaction-domain no no no no no no no 0 10 "cell_act" 1 biomass vcell 1 1
biomass acell 1 "rr_cel_act::libudf" "rr_cell_act::libudf" "hemi_act" 1 biomass vhemi 1 1
biomass ahemi 1 "rr_hemi_act::libudf" "lign_act" 1 biomass vlign 1 1 biomass align 1
"rr_lign_act::libudf" "cell_tar" 1 biomass acell 1 1 gas-phase tar 1 "rr_cell_tar::libudf"
"hemi_tar" 1 biomass ahemi 1 1 gas-phase tar 1 "rr_hemi_tar::libudf" "lign_tar" 1 biomass
align 1 1 gas-phase tar 1 "rr_lign_tar::libudf" "cell_char" 1 biomass acell 1 2 char char_c
0.35 gas-phase pyro_gas 2.6 "rr_cell_char::libudf" "hemi_char" 1 biomass ahemi 1 2 char char_h
0.6 gas-phase pyro_gas 1.6 "rr_hemi_char::libudf" "lign_char" 1 biomass align 1 2 char char_l
0.75 gas-phase pyro_gas 1 "rr_lign_char::libudf" "tar_gas" 1 gas-phase tar 1 1 gas-phase
pyro_gas 4 "rr_tar_gas::libudf" no no

/* continue simulation */
solve/dual-time-iterate 32500 40
file/write-data endsimulation.dat
```

Appendix E: Properties CFD simulation fast biomass pyrolysis

FLUENT
Version: 2d, dp, pbns, eulerian, spe, rke, transient (2d, double precision, pressure-based, Eulerian, species, realizable k-epsilon, transient)
Release: 15.0.0
Title:
Models

Model Settings

Space	2D
Time	Unsteady, 1st-Order Implicit
Viscous Realizable	k-epsilon turbulence model
Wall Treatment	Standard Wall Functions
Multiphase	k-epsilon Models k-epsilon Model for Each Phase
Heat Transfer	Enabled
Solidification and Melting	Disabled
Radiation	None
Species	Non-Reacting
Coupled Dispersed Phase	Disabled
NOx Pollutants	Disabled
SOx Pollutants	Disabled
Soot	Disabled
Mercury	Pollutants Disabled

Material Properties

CHAR PHASE

Material: char_phase (mixture)

Property	Units	Method	Value(s)
Mixture Species		names((char_c char_h char_l) () ())	
Density	kg/m3	volume-weighted-mixing-law	#f
Cp (Specific Heat)	j/kg-k	mixing-law	#f
Thermal Conductivity	w/m-k	mass-weighted-mixing-law	#f
Viscosity	kg/m-s	constant	1.72e-05
Mass Diffusivity	m2/s	constant-dilute-appx (	2.8799999e-05)
Speed of Sound	m/s	none	#f

Material: (char_l . char_phase) (fluid)

Material: (char_l . char_phase) (fluid)

Property	Units	Method	Value(s)
Density	kg/m3	constant	375
Cp (Specific Heat)	j/kg-k	constant	1100
Thermal Conductivity	w/m-k	constant	0.071000002
Molecular Weight	kg/kgmol	constant	100
Standard State Enthalpy	j/kgmol	constant	-9767000
Reference Temperature	k	constant	298.14999
Speed of Sound	m/s	none	#f

Material: (char_h . char_phase) (fluid)

Property	Units	Method	Value(s)
Density	kg/m3	constant	300
Cp (Specific Heat)	j/kg-k	constant	1100
Thermal Conductivity	w/m-k	constant	0.071000002
Molecular Weight	kg/kgmol	constant	100
Standard State Enthalpy	j/kgmol	constant	-17530000
Reference Temperature	k	constant	298.14999
Speed of Sound	m/s	none	#f

Material: (char_c . char_phase) (fluid)

Property	Units	Method	Value(s)
Density	kg/m3	constant	175
Cp (Specific Heat)	j/kg-k	constant	1100
Thermal Conductivity	w/m-k	constant	0.071000002
Molecular Weight	kg/kgmol	constant	100
Standard State Enthalpy	j/kgmol	constant	-45270000
Reference Temperature	k	constant	298.14999
Speed of Sound	m/s	none	#f

BIOMASS PHASE

Material: biomass_phase (mixture)

Property	Units	Method	Value(s)
Mixture Species		names((align vlign ahemi vhemi acell vcell) () ())	
Density	kg/m3	volume-weighted-mixing-law	#f
Cp (Specific Heat)	j/kg-k	mixing-law	#f
Thermal Conductivity	w/m-k	mass-weighted-mixing-law	#f
Viscosity	kg/m-s	constant	1.72e-05
Mass Diffusivity	m2/s	constant-dilute-appx	(2.8799999e-05)
Speed of Sound	m/s	none	#f

Material: (vcell . biomass_phase) (fluid)

Property	Units	Method	Value(s)
Density	kg/m3	constant	500
Cp (Specific Heat)	j/kg-k	constant	1400
Thermal Conductivity	w/m-k	constant	0.20900001
Molecular Weight	kg/kgmol	constant	100
Standard State Enthalpy	j/kgmol	constant	0
Reference Temperature	k	constant	298.14999
Speed of Sound	m/s	none	#f

Material: (acell . biomass_phase) (fluid)

Property	Units	Method	Value(s)
Density	kg/m3	constant	500
Cp (Specific Heat)	j/kg-k	constant	1400
Thermal Conductivity	w/m-k	constant	0.20900001
Molecular Weight	kg/kgmol	constant	100
Standard State Enthalpy	j/kgmol	constant	0
Reference Temperature	k	constant	298.14999
Speed of Sound	m/s	none	#f

Material: (vhemi . biomass_phase) (fluid)

Property	Units	Method	Value(s)
Density	kg/m3	constant	500
Cp (Specific Heat)	j/kg-k	constant	1400
Thermal Conductivity	w/m-k	constant	0.20900001
Molecular Weight	kg/kgmol	constant	100
Standard State Enthalpy	j/kgmol	constant	0
Reference Temperature	k	constant	298.14999
Speed of Sound	m/s	none	#f

Material: (ahemi . biomass_phase) (fluid)

Property	Units	Method	Value(s)
Density	kg/m3	constant	500
Cp (Specific Heat)	j/kg-k	constant	1400
Thermal Conductivity	w/m-k	constant	0.20900001
Molecular Weight	kg/kgmol	constant	100
Standard State Enthalpy	j/kgmol	constant	0
Reference Temperature	k	constant	298.14999
Speed of Sound	m/s	none	#f

Material: (vlign . biomass_phase) (fluid)

Property	Units	Method	Value(s)
Density	kg/m3	constant	500
Cp (Specific Heat)	j/kg-k	constant	1400
Thermal Conductivity	w/m-k	constant	0.20900001
Molecular Weight	kg/kgmol	constant	100
Standard State Enthalpy	j/kgmol	constant	0
Reference Temperature	k	constant	298.14999
Speed of Sound	m/s	none	#f

Material: (align . biomass_phase) (fluid)

Property	Units	Method	Value(s)
Density	kg/m3	constant	500
Cp (Specific Heat)	j/kg-k	constant	1400
Thermal Conductivity	w/m-k	constant	0.20900001
Molecular Weight	kg/kgmol	constant	100
Standard State Enthalpy	j/kgmol	constant	0
Reference Temperature	k	constant	298.14999
Speed of Sound	m/s	none	#f

SAND

Property	Units	Method	Value(s)
Density	kg/m3	constant	2650
Cp (Specific Heat)	j/kg-k	constant	800
Thermal Conductivity	w/m-k	constant	0.75
Viscosity	kg/m-s	constant	1.7894001e-05
Molecular Weight	kg/kgmol	constant	28.966
Standard State Enthalpy	j/kgmol	constant	0
Reference Temperature	k	constant	298.14999
Thermal Expansion Coefficient	1/k	constant	0
Speed of Sound	m/s	none	#f

GAS-PHASE

Material: gas-phase (mixture)

Property	Units	Method	Value(s)
Mixture Species		names ((h2o tar pyro_gas n2) () ())	
Density	kg/m3	incompressible-ideal-gas	#f
Cp (Specific Heat)	j/kg-k	mixing-law	#f
Thermal Conductivity	w/m-k	mass-weighted-mixing-law	#f
Viscosity	kg/m-s	mass-weighted-mixing-law	#f
Mass Diffusivity	m2/s	constant-dilute-appx	(2.8799999e-05)
Speed of Sound	m/s	none	#f

Material: (water-vapor . gas-phase) (fluid)

Property	Units	Method	Value(s)
Cp (Specific Heat)	j/kg-k	polynomial	(300-1000: 1563.0767 1.6037546 -0.0029327841 3.2161008e-06 -1.1568267e-09) (1000-5000: 1233.2338 1.4105233 -0.0004029141 5.5427719e-08 -2.949824e-12)
Thermal Conductivity	w/m-k	constant	0.0261
Viscosity	kg/m-s	constant	1.34e-05
Molecular Weight	kg/kgmol	constant	18.014999
Standard State Enthalpy	j/kgmol	constant	-2.418379e+08
Reference Temperature	k	constant	298.14999
Speed of Sound m/s none #f			

Material: (nitrogen . gas-phase) (fluid)

Property	Units	Method	Value(s)
Cp (Specific Heat)	j/kg-k	polynomial	(300-1000: 979.04298 0.4179639 -0.0011762792 1.6743943e-06 -7.2562971e-10) (1000-5000: 868.62291 0.44162954 -0.00016872295 2.9967875e-08 -2.0043858e-12)
Thermal Conductivity	w/m-k	constant	0.0242
Viscosity	kg/m-s	constant	1.663e-05
Molecular Weight	kg/kgmol	constant	28.0134
Standard State Enthalpy	j/kgmol	constant	0
Reference Temperature	k	constant	298.15
Speed of Sound	m/s	none	#f

Material: (tar . gas-phase) (fluid)

Property	Units	Method	Value(s)
Cp (Specific Heat)	j/kg-k	polynomial	(200 740) (400 1443) (600 1939) (800 2254) (1000 2470) (1500 2790)
Thermal Conductivity	w/m-k	polynomial	(200 0.0091000004) (400 0.020500001) (600 0.0328) (800 0.045899998) (1000 0.059500001) (1500 0.0955)
Viscosity	kg/m-s	polynomial	(200 4.5199999e-06) (400 9.6000003e-06) (600 1.43e-05) (800 1.94e-05) (1000 2.48e-05) (1500 3.9999999e-05)
Molecular Weight	kg/kgmol	constant	100
Standard State Enthalpy	j/kgmol	constant	25500000
Reference Temperature	k	constant	298.14999
Speed of Sound	m/s	none	#f

Material: (pyro_gas . gas-phase) (fluid)

Property	Units	Method	Value(s)
Cp (Specific Heat)	j/kg-k	polynomial	(200 1261) (400 1893) (600 2518) (800 2991) (1000 3346) (1500 3929)
Thermal Conductivity	w/m-k	polynomial	(200 0.0196) (400 0.050700001) (600 0.088399999) (800 0.1311) (1000 0.178) (1500 0.31040001)
Viscosity	kg/m-s	polynomial	(200 8.2099996e-06) (400 1.42e-05) (600 1.9499999e-05) (800 2.4499999e-05) (1000 2.92e-05) (1500 4.0300001e-05)
Molecular Weight	kg/kgmol	constant	25
Standard State Enthalpy	j/kgmol	constant	0
Reference Temperature	k	constant	298.14999
Speed of Sound	m/s	none	#f

Appendix F: User-defined functions

Solid sources

```
#include "udf.h"

/* source rate of 0.115 kg/s for 2d periodic section
   equals 0.03481 kg/s for our GSVR (0.03868*9/10)*/
real total_source = 0.03868; /* total mass source rate kg/s */
real total_sink = 0; /* total mass sink rate kg/s */

/* define biomass composition */
real y_h2o_0 = 0.10;  /* initial biomass water mass fraction, dry basis */

real y_cell_0 = 0.36;   /* DRY BASIS mass fraction for biomass */
real y_hemi_0 = 0.47;
real y_lign_0 = 0.17;

real rho_0 = 500;  /* density of biomass, kg/m3 */
real Cp_biomass = 1400;  /* heat capacity in J/kg-K */
real Cp_h2o = 4184;
real Cp_total;
real T_inject = 300;  /* system temperature in K */
real T_ref = 298.15;  /* reference temperature in K */
real volume_source = 0.0007996013; /* 0.00142439; total volume of feed region */
real volume_sink = 0.001287635; /*0.00090455;  total volume of sink region */
real rs_min = 0.20;  /* minimum & maximum radius of sink */
real rs_max = 0.21;
real rf_min = 0.25;  /* minimum & maximum radius of source */
real rf_max = 0.255;

real total_bed_vol;
real vol_check;


DEFINE_ON_DEMAND(init_bed_vol_calc)
{
    Domain *d_pri, *d_sec;
    Material *sp;
        cell_t c;
        Thread *t_s;
    int i;
    real xc[ND_ND];     /* cell position*/
    real rad_c2;

    volume_source = 0;
    volume_sink = 0;

        d_sec = Get_Domain(3);  /* get gas phase domain information */

    thread_loop_c(t_s, d_sec) {

          begin_c_loop_int(c, t_s) {

            C_CENTROID(xc, c, t_s);
            rad_c2 = sqrt(xc[0]*xc[0] + xc[1]*xc[1]);
            if (rad_c2 > rf_min && rad_c2 < rf_max) {
                volume_source += C_VOLUME(c,t_s);
            }
            if (rad_c2 > rs_min && rad_c2 < rs_max) {
                volume_sink += C_VOLUME(c,t_s);
            }
        }
        end_c_loop_int(c, t_s)
        /*Message("bed mass = %f (kg), node: %d \n",total_bed_mass,myid);*/
    }
    #if RP_NODE
    volume_source = PRF_GRSUM1(volume_source);
    volume_sink = PRF_GRSUM1(volume_sink);
    #endif

    Message("source_vol = %e, sink_vol = %e, node: %d \n",volume_source,volume_sink,myid);
}
```

```
DEFINE_SOURCE(biomass_total,c,tp,dS,eqn)
{

    real source;            /* local mass source term kg/m3*s */
    real xc[ND_ND];     /* cell position*/
    real rad_c2, mod_source, fresh_feed, recyc_feed;

    C_CENTROID(xc, c, tp);
    rad_c2 = sqrt(xc[0]*xc[0] + xc[1]*xc[1]);

    if (rad_c2 > rf_min && rad_c2 < rf_max) {
        mod_source = (1 + 0.05*vol_check)*total_source;

          source = mod_source/volume_source;
        /*if (xc[1] > 0.05 && xc[1] < 0.051) {
            Message("tot_source = %e, mod_source = %e, vol_source = %e, source = %e
\n",total_source,mod_source,volume_source,source);
        }
        source = 0.0;*/
    }
    else if (rad_c2 > rs_min && rad_c2 < rs_max) {
        /* scale the sink terms by the density to ensure constant volume bed */
        source = 0;
    }
    else {
        source = 0.0;

    }

    /* dS[eqn] = 0.0; */

    return source;
}

DEFINE_SOURCE(heat_gen,c,tp,dS,eqn)
{

    real source;            /* local mass source term J/m3*s */
    real xc[ND_ND];     /* cell position*/
    real rad_c2, mod_source, fresh_feed, recyc_feed;

    C_CENTROID(xc, c, tp);
    rad_c2 = sqrt(xc[0]*xc[0] + xc[1]*xc[1]);

    if (rad_c2 > rf_min && rad_c2 < rf_max) {
        mod_source = (1 + 0.05*vol_check)*total_source;

        fresh_feed = mod_source/volume_source;

        Cp_total = Cp_biomass;

        source = fresh_feed*Cp_total*(T_inject-T_ref);
    }
    else if (rad_c2 > rs_min && rad_c2 < rs_max) {
          /* scale the sink terms by the density to ensure constant volume bed

        Cp_total = C_YI(c,tp,0)*Cp_h2o + (1-C_YI(c,tp,0))*Cp_biomass;*/

        source = 0;
    }
    else {
        source = 0.0;
    }



    /* dS[eqn] = 0.0; */

    return source;
}
/* NOTE:

The virgin cellulose feed is calculated as the difference between the total source and the
water/hemi/lignin sources
because it is the last species int he phase list.
*/
```

```
DEFINE_SOURCE(hemi_feed,c,tp,dS,eqn)
{

    real source;            /* local mass source term kg/m3*s */
    real xc[ND_ND];     /* cell position*/
    real rad_c2, mod_source, fresh_feed, recyc_feed;

    C_CENTROID(xc, c, tp);
    rad_c2 = sqrt(xc[0]*xc[0] + xc[1]*xc[1]);

    if (rad_c2 > rf_min && rad_c2 < rf_max) {

        mod_source = (1 + 0.05*vol_check)*total_source;

        source = mod_source/volume_source*y_hemi_0;
    }
    else if (rad_c2 > rs_min && rad_c2 < rs_max) {
        /* scale the sink terms by the density to ensure constant volume bed */
        source = 0;
    }
    else {
        source = 0.0;
    }

    /* dS[eqn] = 0.0; */

    return source;
}


DEFINE_SOURCE(lign_feed,c,tp,dS,eqn)
{
       Analogous to hemi_feed
}


DEFINE_SOURCE(water_feed_gas,c,tp,dS,eqn)
{
       Analogous to hemi_feed
}

DEFINE_SOURCE(heat_gen_gas,c,tp,dS,eqn)
{

    real source;            /* local mass source term W/m3 */
    real xc[ND_ND];     /* cell position*/
    real rad_c2, mod_source, fresh_feed, recyc_feed;
    real dHvap = 2257000;  /* water enthalpy of vaporization in J/kg */

    C_CENTROID(xc, c, tp);
    rad_c2 = sqrt(xc[0]*xc[0] + xc[1]*xc[1]);

    if (rad_c2 > rf_min && rad_c2 < rf_max) {
        mod_source = (1 + 0.05*vol_check)*total_source;

        fresh_feed = mod_source/volume_source*y_h2o_0;

        Cp_total = Cp_h2o;

        source = fresh_feed*(Cp_total*(T_inject-T_ref) - dHvap);
    }
    else if (rad_c2 > rs_min && rad_c2 < rs_max) {

        Cp_total = C_YI(c,tp,0)*Cp_h2o + (1-C_YI(c,tp,0))*Cp_biomass;*/

        source = 0;
    }
    else {
        source = 0.0;
    }

    /* dS[eqn] = 0.0; */

    return source;
}
```

```
DEFINE_SOURCE(heat_rad_biomass,c,tp,dS,eqn)
{

    Thread *t_m;    /* get mixture thread, */
    Thread *t_b;   /* get biomass-phase thread, which is index 1, that corresponds to current
zone/thread */
    Thread *t_c;   /* get char-phase thread, which is index 2, that corresponds to current
zone/thread */
    Thread *t_s;   /* get sand-phase thread, which is index 3, that corresponds to current
zone/thread */

    real source;            /* local mass source term J/m3*s */
    real sigma = 5.676e-8;  /* constant, W/m2*T4 */
    real em = 0.75;  /* emissivity */
    real Dp = 0.0005;
    real A_tot;  /* total surface area in cell per volume */
    real flux;  /* heat flux */
    real vf_b, vf_c, vf_s, vf_t; /* biomass, char, sand, and total solid volume fractions */
    real T_b, T_c, T_s; /* biomass, char, and sand temps */

    t_m = THREAD_SUPER_THREAD(tp);  /* get mixture thread pointer that corresponds to the same
zone as secondary phase thread "t"*/
       t_b = THREAD_SUB_THREAD(t_m, 1);  /* get solid-phase thread, which is index 1, that
corresponds to current zone/thread */
    t_c = THREAD_SUB_THREAD(t_m, 2);
    t_s = THREAD_SUB_THREAD(t_m, 3);

    vf_b = C_VOF(c, t_b);
    vf_c = C_VOF(c, t_c);
    vf_s = C_VOF(c, t_s);
    vf_t = vf_b + vf_c + vf_s;

    T_b = C_T(c, t_b);
    T_c = C_T(c, t_c);
    T_s = C_T(c, t_s);

    if (vf_t < 1e-6) {
        source = 0;
    }
    else {

        flux = sigma*em*( (vf_c/vf_t)*(pow(T_c,4) - pow(T_b,4)) + (vf_s/vf_t)*(pow(T_s,4) -
pow(T_b,4)) );

        A_tot = C_VOF(c,tp)*6/Dp;

        source = flux*A_tot;
    }

    /* dS[eqn] = 0.0; */

    return source;
}


DEFINE_SOURCE(heat_rad_char,c,tp,dS,eqn)
{
       Analogous to heat_rad_biomass
}


DEFINE_SOURCE(heat_rad_sand,c,tp,dS,eqn)
{
       Analogous to heat_rad_biomass
}
```

Reaction rates

```
#include "udf.h"

/*
This has been modified to match the kinetic parameters in DXue & Fox CES 55 (2011) 2440
*/

real rate_cutoff = 1e-10;  /* cutoff below which rate is set to zero */
real vf_cutoff = 1e-6;
real Dp = 0.0005;  /* particle diameter in m */

    /* mass fraction [kg/kg-phase] and MW [kmole/kg] are access via
yi[phase][species_ID_number] or mw[][]
    gas phase ID = 0,     biomass phase ID = 1,    char phase ID = 2,
    Gas species:        (0) H2O,   (1) Tar,    (2) pyro_gas,     (3) N2
    Biomass phase:    (0) aLign,  (1) vLign,  (2) aHemi,
                      (3) vHemi,     (4) aCell,  (5) vCell
    Char phase:
    */

/* ========================================================================
/*  Activation
/* ========================================================================*/

DEFINE_HET_RXN_RATE (rr_cell_act,c,t,r,mw,yi,rr,rr_t)
{
    Thread **pt = THREAD_SUB_THREADS(t);
    Thread *t_g = pt[0];    /* get gas-phase thread, which is index 0, that corresponds to
current zone/thread */
    Thread *t_b = pt[1];   /* get biomass-phase thread, which is index 1, that corresponds to
current zone/thread */
    Thread *t_c = pt[2];   /* get char-phase thread, which is index 2, that corresponds to
current zone/thread */
    Thread *t_s = pt[3];   /* get sand-phase thread, which is index 3, that corresponds to
current zone/thread */
    real r_conc;  /* in kg-mole/m3, as necessary */
    real k_eff;       /* effect rate coefficient in m3/[s*mol(site)] */
    real Af = 2.8e19; /* A-factor in 1/sec */
    real Ea = 242400;  /* activation energy in J/mol */
    real Rg = 8.314;  /* gas constant in J/mol*K */

    real xc[ND_ND];
    real rad_c2;
    C_CENTROID(xc, c, t);
    rad_c2 = sqrt(xc[0]*xc[0] + xc[1]*xc[1]);
    /* calculatekinetic rate,  */

    r_conc = C_R(c,t_b)*yi[1][5]/mw[1][5];  /* in kg-mole/m3, virgin cellulose concentration*/

    k_eff = Af*exp(-Ea/(Rg*C_T(c,t_b)));       /* rate coefficient in 1/[s] */

    /*
    if (rad_c2 > 0.26 && rad_c2 < 0.265 && xc[1] > 0.05 && xc[1] < 0.051) {
        Message("yi = %e, mw = %e, r_conc = %e, k_eff: %e, id = %d
\n",yi[1][6],mw[1][6],r_conc,k_eff,myid);
    }
    */
    if (k_eff*C_VOF(c,t_b)*r_conc < rate_cutoff || C_VOF(c,t_b) < vf_cutoff) {
        *rr = 0;
    }
    else {
        *rr = k_eff*C_VOF(c,t_b)*r_conc;  /* in kgmole/m3*s */
    }
    return;
}

DEFINE_HET_RXN_RATE (rr_hemi_act,c,t,r,mw,yi,rr,rr_t)
{
    Analogous to rr_cell_act
}

DEFINE_HET_RXN_RATE (rr_lign_act,c,t,r,mw,yi,rr,rr_t)
{
    Analogous to rr_cell_act
}
```

```
/* ========================================================================
/*  activated Biomass --> Tar
/* ========================================================================*/

DEFINE_HET_RXN_RATE (rr_cell_tar,c,t,r,mw,yi,rr,rr_t)
{
    Thread **pt = THREAD_SUB_THREADS(t);
    Thread *t_g = pt[0];    /* get gas-phase thread, which is index 1, that corresponds to
current zone/thread */
    Thread *t_b = pt[1];   /* get biomass-phase thread, which is index 1, that corresponds to
current zone/thread */
    Thread *t_c = pt[2];   /* get char-phase thread, which is index 2, that corresponds to
current zone/thread */
    Thread *t_s = pt[3];   /* get sand-phase thread, which is index 3, that corresponds to
current zone/thread */
    real r_conc;  /* in kg-mole/m3, as necessary */
    real k_eff;       /* effect rate coefficient in m3/[s*mol(site)] */
    real Af = 3.28e14; /* A-factor in 1/sec */
    real Ea = 196500;  /* activation energy in J/mol */
    real Rg = 8.314;  /* gas constant in J/mol*K */

    real xc[ND_ND];
    real rad_c2;
    C_CENTROID(xc, c, t);
    rad_c2 = sqrt(xc[0]*xc[0] + xc[1]*xc[1]);


    /* calculatekinetic rate,  */

    r_conc = C_R(c,t_b)*yi[1][4]/mw[1][4];  /* in kg-mole/m3, virgin cellulose concentration*/

    k_eff = Af*exp(-Ea/(Rg*C_T(c,t_b)));       /* rate coefficient in 1/[s] */

    /*
    if (rad_c2 > 0.26 && rad_c2 < 0.265 && xc[1] > 0.05 && xc[1] < 0.051) {
        Message("yi = %e, mw = %e, r_conc = %e, k_eff: %e, id = %d
\n",yi[1][5],mw[1][5],r_conc,k_eff,myid);
    }
    */

    if (k_eff*C_VOF(c,t_b)*r_conc < rate_cutoff || C_VOF(c,t_b) < vf_cutoff) {
        *rr = 0;
    }
    else {
        *rr = k_eff*C_VOF(c,t_b)*r_conc;  /* in kgmole/m3*s */
    }
    return;
}


DEFINE_HET_RXN_RATE (rr_hemi_tar,c,t,r,mw,yi,rr,rr_t)
{
       Analogous to rr_cell_tar
}



DEFINE_HET_RXN_RATE (rr_lign_tar,c,t,r,mw,yi,rr,rr_t)
{
       Analogous to rr_cel_tar
}
```

```
/* ==========================================================================
/*  activated Biomass --> Char + Gas
/* ==========================================================================*/

DEFINE_HET_RXN_RATE (rr_cell_char,c,t,r,mw,yi,rr,rr_t)
{
    Thread **pt = THREAD_SUB_THREADS(t);
    Thread *t_g = pt[0];    /* get gas-phase thread, which is index 1, that corresponds to
current zone/thread */
    Thread *t_b = pt[1];   /* get biomass-phase thread, which is index 1, that corresponds to
current zone/thread */
    Thread *t_c = pt[2];   /* get char-phase thread, which is index 2, that corresponds to
current zone/thread */
    Thread *t_s = pt[3];   /* get sand-phase thread, which is index 3, that corresponds to
current zone/thread */
    real r_conc;  /* in kg-mole/m3, as necessary */
    real k_eff;       /* effect rate coefficient in m3/[s*mol(site)] */
    real Af = 1.3e10; /* A-factor in 1/sec */
    real Ea = 150500;  /* activation energy in J/mol */
    real Rg = 8.314;  /* gas constant in J/mol*K */

    /*real xc[ND_ND];
    real rad_c2;
    C_CENTROID(xc, c, t);
    rad_c2 = sqrt(xc[0]*xc[0] + xc[1]*xc[1]);
    if (rad_c2 > 0.20 && rad_c2 < 0.21) {
        Message("surf_site_frac = %f, node: %d \n",surf_site_frac_recyc,myid);
    }*/

    /* calculatekinetic rate,  */

    r_conc = C_R(c,t_b)*yi[1][4]/mw[1][4];  /* in kg-mole/m3, virgin cellulose concentration*/

    k_eff = Af*exp(-Ea/(Rg*C_T(c,t_b)));       /* rate coefficient in 1/[s] */

    if (k_eff*C_VOF(c,t_b)*r_conc < rate_cutoff || C_VOF(c,t_b) < vf_cutoff) {
        *rr = 0;
    }
    else {
        *rr = k_eff*C_VOF(c,t_b)*r_conc;  /* in kgmole/m3*s */
    }

    return;
}



DEFINE_HET_RXN_RATE (rr_hemi_char,c,t,r,mw,yi,rr,rr_t)
{
       Analogous to rr_cell_char
}



DEFINE_HET_RXN_RATE (rr_lign_char,c,t,r,mw,yi,rr,rr_t)
{
       Analogous to rr_cell_char
}
```

```
/* ============================================================================
/*  Tar --> Gas
/* ============================================================================*/

DEFINE_HET_RXN_RATE (rr_tar_gas,c,t,r,mw,yi,rr,rr_t)
{
    Thread **pt = THREAD_SUB_THREADS(t);
    Thread *t_g = pt[0];    /* get gas-phase thread, which is index 1, that corresponds to
current zone/thread */
    Thread *t_b = pt[1];   /* get biomass-phase thread, which is index 1, that corresponds to
current zone/thread */
    Thread *t_c = pt[2];   /* get char-phase thread, which is index 2, that corresponds to
current zone/thread */
    Thread *t_s = pt[3];   /* get sand-phase thread, which is index 3, that corresponds to
current zone/thread */
    real r_conc;  /* in kg-mole/m3, as necessary */
    real k_eff;       /* effect rate coefficient in m3/[s*mol(site)] */
    real Af = 4.25e6; /* A-factor in 1/sec */
    real Ea = 108000;  /* activation energy in J/mol */
    real Rg = 8.314;  /* gas constant in J/mol*K */

    /* calculatekinetic rate,  */

    r_conc = C_R(c,t_g)*yi[0][1]/mw[0][1];  /* in kg-mole/m3, virgin cellulose concentration*/

    k_eff = Af*exp(-Ea/(Rg*C_T(c,t_g)));       /* rate coefficient in 1/[s] */

    if (k_eff*C_VOF(c,t_b)*r_conc < rate_cutoff || C_VOF(c,t_b) < vf_cutoff) {
        *rr = 0;
    }
    else {
        *rr = k_eff*C_VOF(c,t_g)*r_conc;  /* in kgmole/m3*s */
    }
    return;
}
```

Appendix G: Energy balance fast biomass pyrolysis

Initial conditions

Gas feeding:

	wt% feed	$\dot{m}_{feed}$(kg/s)	$C_{p,l}$(kJ/kg.K)	$C_{p,g}$(kJ/kg.K)	ΔH_{vap}(kJ/kg)	ΔT(K)	ΔH(kJ/s)
Nitrogen	100.0	0.113	(-)	1.14	(-)	185	-23.83

Biomass feeding:

	wt% feed	$\dot{m}_{feed}$(kg/s)	$C_{p,l}$(kJ/kg.K)	$C_{p,g}$(kJ/kg.K)	ΔH_{vap}(kJ/kg)	ΔT(K)	ΔH(kJ/s)
Biomass	90.91	0.031646	1.4	(-)	(-)	438	19.41
Water	9.09	0.003164	4.184	2.1	2442	438	11.12

Heat of reaction:

Assuming a 50 % pathway split this results in a net reaction contribution of 3.05 kJ/s

	mass fraction	activation (kJ/s)	tar generation (kJ/s)	char generation (kJ/s)	secondary cracking (kJ/s)
cell	0.36	0	1.45	-0.11	-0.24
hemi	0.47	0	1.89	-0.15	-0.31
lignin	0.17	0	0.69	-0.05	-0.11

Because the enthalpy of reaction for the various steps is given by:

	$\Delta H_{reaction}$(kJ/kg)
activation	0
tar generation	255.0
char generation	-20.0
secondary cracking	-42.0

Resulting in an energy balance of ΔH = 9.846 kJ/kg

Adjusted conditions

Gas feeding:

	wt% feed	$\dot{m}_{feed}$(kg/s)	$C_{p,l}$(kJ/kg.K)	$C_{p,g}$(kJ/kg.K)	ΔH_{vap}(kJ/kg)	ΔT(K)	ΔH(kJ/s)
Nitrogen	100.0	0.2219	(-)	1.14	(-)	141	-35.79

Biomass feeding:

	wt% feed	$\dot{m}_{feed}$(kg/s)	$C_{p,l}$(kJ/kg.K)	$C_{p,g}$(kJ/kg.K)	ΔH_{vap}(kJ/kg)	ΔT(K)	ΔH(kJ/s)
Biomass	90.91	0.031646	1.4	(-)	(-)	481	21.33
Water	9.09	0.003164	4.184	2.1	2442	181	11.41

The heat of reaction remains the same as in the previous case, resulting in an even energy balance.